

Assessment of an aircraft propeller noise model by verification & experimental validation

N.S.L. Elbers



Assessment of an aircraft propeller noise model by verification & experimental validation

by

N.S.L. Elbers

to obtain the degree of Master of Science in Aerospace Engineering
In assignment of the Control and Operations department
at the Aircraft Noise and Climate Effects (ANCE) section

at the Delft University of Technology
To be publicly defended on December 22th, 2021

Chair holder

Prof. dr. D.G. Simons, ANCE, Delft University of Technology

Supervisors

Prof. dr. ir. M. Snellen ANCE, Delft University of Technology
Msc. B. von den Hoff ANCE, Delft University of Technology

Other

AP. dr. ir. R. Vos FPP, Delft University of Technology

An electronic version of this thesis is available at <http://repository.tudelft.nl/>.



Preface

This thesis is performed as part of the final phase of the Master Aerospace Engineering of the Delft University of Technology at the Aircraft Noise and Climate Effect section of the faculty of Aerospace Engineering. After a short search, I found this subject and it immediately drew my attention due to its practical application and use. I am thankful I can perform this study and hopefully contribute to research into new propeller designs.

I want to thank my supervisor Bieke von den Hoff for her time during these 30 weeks and for helping me where needed. I really appreciated the feedback from her and the critical questions she asked to help me understand the underlying principles better. Despite the Corona crisis, I felt and feel that I can always contact her whenever needed. I also want to thank prof. dr. ir. M. Snellen and prof. dr. D.G Simons for offering this thesis research and their constructive feedback during the process meetings. I am grateful for the help of Menno van Luijn and Menno Klaassen during the experiment that has been conducted at Teuge Airport. I was not able to do my noise experiment without the Pipistrel Velis Electro, owned by E-Flight, thank you for the amazing cooperation.

Zoetermeer, December 8, 2021

Abstract

The need to contribute to a sustainable future of the aviation industry has spiked an interest in turboprop engines. This is due to three reasons being the higher propulsive efficiency, the better take-off and landing performance on short runways, and the new developments in hybrid and electric aircraft which are propeller-driven. The most significant drawback is the noise they generate, which is undesirable for the surroundings and passengers on the aircraft. The turboprop noise consists of the jet, core, and propeller noise, of which the propeller noise is the most dominant. To reduce the propeller noise, new advanced propeller designs are needed. To see what the effect of the new designs is on the noise emissions, propeller noise models can be used as a valuable tool during the design phase. The models can only be confidently used when they have been properly validated. The more data is used to validate, the higher the confidence will be.

A master student that graduated from the Aircraft Noise and Climate Effects (ANCE) section at the TU Delft created a propeller noise model called HeliX-tool. This model is validated by another model and wind tunnel measurements from NASA but not yet by full-scale outdoor experimental data. To increase the confidence of the HeliX-tool, this model is compared to full-scale outdoor experimental data, consisting of three take-offs and one fly-over, and the quality is assessed in this thesis. The purpose of this thesis is to assess the quality of the HeliX-tool by verification and experimental validation.

Propeller noise consists of periodic noise and broadband noise. Periodic noise is divided into loading and thickness noise. The HeliX-tool only models the steady loading and thickness noise, omitting the broadband noise, and is based upon the helicoidal surface theory. This theory derives the radiation equations by representing the blades as a helicoidal surface and includes the effect of the blade loading, blade thickness, blade sweep, and forward flight. The helicoidal surface theory needs the aerodynamic and performance characteristics of the propeller blade which are obtained by implementing the two external analysis tools, XFOIL and XRotor.

A sensitivity analysis is performed on several input variables that are found to be difficult to obtain. These parameters are changed in value and the difference in SPL level is compared to the baseline case. From this, it is concluded that the HeliX-tool is most sensitive to a change in axial flight speed and the least sensitive to the radial thickness over chord distribution.

The full-scale outdoor experiment is performed with the Pipistrel Velix Electro at Teuge airport to obtain the full-scale outdoor data to compare the output of the model. The Pipistrel Velix Electro is a fully electric-powered two-seater owned by E-flight academy. This aircraft is suitable for the validation of the HeliX-tool as the propeller noise will be the dominant noise source now the engine is electric. The microphone array that is used to obtain the full-scale outdoor data has 64 microphones placed in an Underbrink configuration.

The propeller geometry is an important input for the HeliX-tool and is obtained by 3D scanning the propeller blade of the Pipistrel Velix Electro with the FaroBlu HD laser. The geometry is further processed to obtain the radial blade pitch angle distribution, chord over diameter distribution, thickness over chord distribution, and airfoil coordinates.

The validation metrics are the SPL and OSPL values. The frequency spectra are generated for both the full-scale outdoor data and the HeliX-tool when the aircraft is overhead the microphone array and are compared to each other. In general, the HeliX-tool gives higher SPL values compared to the full-scale outdoor data, which also results in higher OSPL values from the HeliX-tool. For higher tonal harmonics, the SPL value of the peaks decreases. This is true for all the measurements, except for the 5th and 6th harmonic of the fly-over. These result in higher SPL values and do not coincide with the frequency of the 5th and 6th tonal harmonic. The first and third take-off showed high side lobes besides the 4th and 5th tonal harmonic and beamforming are performed at the frequencies of these side lobes and the 5th peak of the fly-over. The 4th tonal harmonic for take-off 1 and 3 and the 2nd tonal harmonic for the fly-over is chosen to beamform as well as check.

With beamforming, the location of the most dominant noise source can be found, although the resolution is limited by the Rayleigh limit. Functional beamforming is used to reduce the side lobes and from the plot can be seen that the dominant noise source shifts in location. It can be concluded that there might be a noise source present within the Rayleigh limit and is thus not seen in the beamforming plot, but this cannot be confirmed.

The values of the validation metrics are within 4 dB and from this can be concluded that the confidence in the HeliX-tool is increased. It can be used as a tool in the design phase of new advanced propellers but is limited to Mach numbers below 0.7 due to the Prandtl-Glauert compressibility correction used in XRotor.

Contents

Preface	i
Abstract	ii
List of Figures	iv
List of Tables	vi
Nomenclature	vii
1 Introduction	1
1.1 Research objective	1
1.2 Research framework	2
2 HeliX-tool Analysis	3
2.1 Propeller noise	3
2.2 Helicoidal surface theory	5
2.3 HeliX-tool assumptions and limitations	8
2.4 External analysis tools	8
2.4.1 XFOIL	8
2.4.2 XRotor	9
2.5 HeliX-tool methodology	9
2.6 HeliX-tool input	10
2.7 HeliX-tool output	13
3 Verification of the HeliX-tool	15
3.1 Sensitivity analysis	15
3.2 Sensitivity method	16
3.3 Results	16
3.3.1 Blade pitch angle	16
3.3.2 Axial flight speed	18
3.3.3 Radial chord over diameter distribution	20
3.3.4 Radial thickness over chord distribution	21
3.4 Robustness of the HeliX-tool	22
4 Measurements set-up	23
4.1 Aircraft	23
4.2 Microphone array	24
4.3 Experiment location	25
4.4 Weather conditions	26
4.5 Additional tools	26
5 Propeller geometry	28
5.1 3D scanner and arm	28
5.2 Geometry processing	29
6 Data Analysis of Measurements	32
6.1 Data from GoPro and GPS sensor	32
6.2 Calibrated noise data	33
6.2.1 Spectrogram	33
6.2.2 OSPL & OASPL	35
6.2.3 Frequency spectra	37
6.3 Main lobe width	38
7 Validation of the HeliX-tool	40
7.1 Validation method	40
7.2 Result	40
7.2.1 Frequency spectra	40
7.2.2 Beamforming	42
7.2.3 Directionality plot	49
8 Conclusion & recommendations	51
8.1 Conclusion	51
8.2 Recommendations	51
Bibliography	53
A Read me file for HeliX-tool	55
B Photogrammetry	57
C Conventional beamforming plots	58

List of Figures

2.1	Monopole sound source	3
2.2	Alternate forms of dipole sound source	4
2.3	Alternate forms of quadrupole sound source	4
2.4	Definition of MCA and FA	6
2.5	Definition of θ	6
2.6	Normalized thickness distribution used in the HeliX-tool	7
2.7	Assumed lift and drag distribution used in the HeliX-tool	8
2.8	Flowchart of HeliX-tool	10
2.9	Helical tip Mach number as a function of the advance ratio J	12
2.10	Noise metrics plots with $M_x = 0.35$, $J = 1.7$, $\beta_{0.75} = 45.8^\circ$	14
3.1	Typical propeller performance plot showing C_p as a function of J for several $\beta_{0.75}$	17
3.2	Relation between the performance coefficients, C_p and C_t	17
3.3	Frequency spectra of different $\beta_{0.75}$ values	18
3.4	Maximum SPL value with respect to M_h	19
3.5	Frequency spectra of different V_x values	19
3.6	Frequency spectra of different Δc values	21
3.7	Frequency spectra of different $\Delta \delta$ values	22
4.1	Pipistrel Velis Electro	23
4.2	The P-812-164-F3A Certified fixed-pitch composite three-blade	24
4.3	The microphone array configuration	25
4.4	Teuge airport	26
4.5	Flight route processed in Matlab	27
5.1	3D scanning of the propeller blade of the Pipistrel Velis Electro	28
5.2	3D scanned propeller blade of the Pipistrel Velis Electro in CATIA	29
5.3	The 3D scanned propeller blade with the 18 airfoil coordinates sections	30
5.4	Definition of β	30
5.5	Pipistrel propeller design parameters	31
5.6	Sketch of section 1 generated in CATIA	31
6.1	Cockpit image from the GoPro video	32
6.2	The Hanning window and its discrete time Fourier transform	34
6.3	Spectrograms of the four measurements	35
6.4	A-weighting function	36
6.5	OSPL and OASPL plots of the four measurements	37
6.6	Frequency spectra of the four measurements	38
6.7	Simulation of the main lobe width	39
7.1	Frequency spectra of the modelled operations from the HeliX-tool	40
7.2	Frequency spectra of the HeliX-tool and outdoor data	41
7.3	Scatter plot	42
7.4	Indication of side lobes and 5th peak of fly-over	43
7.5	Beamformed plots of take-off 1	45
7.6	Location of dominant noise source for the 4th tonal harmonic, 4th and 5th side lobe	45
7.7	Beamformed plots of take-off 3	46
7.8	Location of dominant noise source for the 4th tonal harmonic and 4th side lobe	46
7.9	Functional beamformed plots of the fly-over measurement	47
7.10	Location of dominant noise source for the 2nd BPF and 5th peak for different time stamps	48
7.11	Indication of location of noise sources	48
7.12	Directionality plot	49
7.13	Polar plot of OSPL levels when aircraft is overhead the microphone array	50
A.1	HeliX-tool flowchart	56

B.1	Capturing the object with photogrammetry	57
C.1	Conventional beamformed plots of take-off 1	58
C.2	Conventional beamformed plots of take-off 3	59
C.3	Conventional Beamformed plots of the fly-over measurement	60

List of Tables

2.1	Output parameters of the fitting	9
2.2	Variables with fixed values	11
2.3	M_{crit} for all 18 blade sections	13
2.4	File names of normalized airfoil coordinates of each section	13
3.1	Sensitivity variables	16
3.2	Values and differences of C_p , C_t for different $\beta_{0.75}$ with $M_x = 0.35$ and $J = 1.4$	17
3.3	SPL values of the four harmonics for different $\beta_{0.75}$ with $M_x = 0.35$ and $J = 1.4$	18
3.4	Values and differences of C_p , C_t for different V_x with $J = 1.4$ and $\beta_{0.75} = 35^\circ$	19
3.5	SPL values of the four harmonics for different V_x with $J = 1.4$ and $\beta_{0.75} = 35^\circ$	20
3.6	Values and differences of C_p , C_t for different Δc with $M_x = 0.35$, $J = 1.4$ and $\beta_{0.75} = 35^\circ$	20
3.7	SPL values of the four harmonics for different Δc with $M_x = 0.35$ and $J = 1.4$ and $\beta_{0.75} = 35^\circ$	21
3.8	SPL values of the four harmonics for different $\Delta\delta$ with $M_x = 0.35$, $J=1.4$ and $\beta_{0.75} = 35^\circ$	22
4.1	Weather conditions at Teuge Airport	26
5.1	Geometry data file sections	30
6.1	GoPro data	32
6.2	GPS coordinates with corresponding velocity	33
6.3	BPF and J	33
6.4	Parameters needed for the generation of the spectrograms	34
6.5	The SPL levels and BPF of the outdoor data	38
7.1	The SPL levels and BPF from the HeliX-tool	41
7.2	Outdoor data OSPL parameters	50

Nomenclature

List of Abbreviations

2D	Two-dimensional
3D	Three-dimensional
ADS-B	Automatic Dependent Surveillance-Broadcast
BPF	Blade Passage Frequency
CAD	Computer Aided Design
CFDBF	Conventional Frequency Domain Beamforming
CSM	Cross-Spectral Matrix
DAQ	Data Acquisition System
DFT	Discrete Fourier Transform
FA	Face Alignment
FB	Functional Beamforming
GPS	Global Positioning System
ILS	Instrument Landing System
KNMI	Royal Dutch Meteorological Institute
LAT	Latitude
LON	Longitude
MCA	Mid Chord Alignment
MTOP	Maximum Take-Off Power
MTOW	Maximum Take-Off Weight
OASPL	Overall A-weighted Sound Pressure Level
OSPL	Overall Sound Pressure Level
PSD	Power Spectral Density
SPL	Sound Pressure Level

List of Symbols

$(C_p)_{min}$	Minimum pressure coefficient	[–]
$(C_{p,0})_{min}$	Minimum pressure coefficient at $\alpha = 0^\circ$	[–]
α	Angle of attack	[°]
α_{0L}	Zero lift angle of attack	[°]
β	Blade pitch angle	[°]
$\beta_{0.75}$	Blade angle at 75%R	[°]
$\Delta\beta$	Radial blade pitch angle distribution	[°]
$\Delta\delta$	Radial thickness over chord distribution	[–]
Δc	Radial chord over diameter distribution	[–]
ΔC_l	Increment in lift to stall	[–]
$\frac{dC_d}{dC_L^2}$	Quadratic coefficient	[–]
$\frac{dC_l}{d\alpha}$	Lift gradient	[–]
$\frac{r}{R}$	Radial position to radius ratio	[–]
γ	Ratio between specific heats, C_p and C_v	[–]
$\left(\frac{dC_l}{d\alpha}\right)_{stall}$	Lift gradient at stall	[–]
Ω	Angular speed	[rad/s]
Ω_D	Doppler shifted angular speed	[rad/s]
ϕ_0	Phase lag due to offset	[°]
ϕ_s	Phase lag due to sweep	[°]
ϕ_s	Phase lag	[°]
ψ_D	Drag distribution function	[–]
ψ_L	Lift distribution function	[–]
ψ_V	Thickness distribution function	[–]
ρ	Density of air	[kg/m ³]
θ	Radiation angle from propeller axis to observer point	[°]
adv	Advance coefficient	[–]
B	Number of blades	[–]
B_D	Chord to diameter ratio	[–]
c	Speed of sound	[m/s]
C_d	Drag coefficient	[–]

C_l	Lift coefficient	[—]
C_m	Moment coefficient	[—]
C_p	Specific heat of a gas at constant pressure	[—]
C_p	Power coefficient	[—]
C_t	Thrust coefficient	[—]
C_v	Specific heat of a gas at constant volume	[—]
$C_{d_{min}}$	Minimum drag coefficient	[—]
C_{L0}	Zero lift coefficient at minimum C_d	[—]
$C_{l_{cdmin}}$	Lift coefficient at minimum C_d	[—]
$C_{L_{max}}$	Maximum lift coefficient	[—]
$C_{L_{min}}$	Minimum lift coefficient	[—]
$C_{p,crit}$	Critical pressure coefficient	[—]
D	Propeller diameter	[m]
D_{array}	Array aperture	[m]
dt	Sampling time	[s]
F	Thrust	[N]
f	Frequency	[Hz]
f_s	Sampling frequency	[Hz]
f_k	Higher harmonics frequency	[Hz]
f_{Re}	Reynolds number scaling component	[—]
h	Vertical distance between source and observer	[m]
J	Advance ratio	[—]
k_x, k_y	Non-dimensional wave numbers	[—]
M	Mach number	[—]
m	Number of harmonics	[—]
M_{crit}	Critical Mach number	[—]
M_h	Helical tip Mach number	[—]
M_r	Effective Mach number	[—]
M_t	Rotational tip Mach number	[—]
M_x, M_∞	Flight speed Mach number	[—]
P	Power	[W]
P	Pressure	[hPa]
P_{Dm}	Drag dipole component	[—]
p_{e0}	Reference effective pressure	[Pa]
p_e	Effective pressure	[Pa]
P_{Lm}	Lift dipole component	[—]
P_{Vm}	Volume displacement component	[—]
R	Propeller blade radius	[m]
r	Distance between observer and source	[m]
R_d	Rayleigh limit	[m]
Re	Reynolds number	[—]
Re_{ref}	Reference Reynolds number	[—]
RH	Relative humidity	[%]
RPM	Rotational speed	[RPM]
rps	Revolutions per second	[rev/s]
T	Temperature	[°C]
t_b	Maximum thickness to chord ratio	[—]
V_x	Axial flight speed	[m/s]
V_{wind}	Wind speed	[m/s]
y	Altitude	[m]
z	Radial position of a blade element as fraction of the radius	[—]

1

Introduction

Turboprops are making a comeback now the aviation industry needs to contribute to a sustainable future and decrease its emissions. There are three reasons why these turboprops have increased interest. The first one is their higher fuel efficiency for short-haul flights with respect to turbojet engines. It has been found that short-haul flights emit more carbon dioxide per person per km than long-haul flights [1]. Therefore, reintroducing the turboprop for these flights will increase the engine's efficiency compared to the turbojet and decrease the emissions [2]. Secondly, aircraft with turboprop engines have better take-off and landing performance, which allows for transporting passengers to and from small airports [2]. The third reason for the comeback of the turboprops is the new developments in hybrid and electric aircraft with its most significant drawback, the low energy density of the current batteries. The best way to mitigate that disadvantage is to make better use of the amount of energy that can be stored, which brings attention to the turboprop for its efficiency and high bypass ratios [2].

There is, however, a disadvantage to using turboprops. While the turboprop will emit less carbon dioxide due to its efficiency, it will emit more noise during take-off and landing, which is undesirable.

New advanced designs of propellers are created to reduce noise emissions. To check what the noise emission is of the new designs and to see what the effects of the improvements are on the noise emission, so-called propeller noise models are valuable tools in the design phase. These models predict the propeller noise by modeling the sound sources. Although the not-electric turboprop noise consists of the core, jet, and propeller noise [3], the propeller noise is most dominant [4]. This is the reason why the propeller noise is of most interest when reducing the turboprop noise. Various propeller noise models are created for research.

As experiments at airports and in wind tunnels are expensive in time and money, a high-quality propeller noise model is of value in the design phase of a new propeller. Apart from being a valued tool in the design of a new propeller, propeller noise models can be used to compare noise metrics of existing propellers and the models can be used to verify and validate other models. To confidently use these models, the models need to be verified and validated.

1.1. Research objective

The propeller noise model called HeliX-tool is designed by Haddaoui [5]. This model is available to the Faculty of Aerospace Engineering but is only validated by using other models and windtunnel data of NASA. To increase the confidence in this model, the output of the model is compared to full-scale experimental data in operational conditions and the quality of the model will be assessed.

The research objective is therefore: "To assess the quality of the propeller noise model HeliX-tool by verification and experimental validation".

This objective is accompanied by the following research question: *"What is the quality of the HeliX-tool and should this be used as a tool for future propeller designs?"* This research question is supported by the sub-questions below which are answered in detail in this thesis report.

1. How is the HeliX-tool constructed?
 - (a) What is the structure of the HeliX-tool?
 - (b) What are the assumptions and generalizations taken into account within the model?
 - (c) What is the influence of these assumptions and generalizations on the results of the model?
 - (d) What are the inputs and outputs of the model?
 - (e) How are the inputs of the model obtained?
2. How is the quality of the HeliX-tool assessed?
 - (a) What is the definition of "quality" for the purpose of this project?

- (b) What method is used for the quality assessment of the model?
- (c) What metrics should be assessed during this method?
- (d) What data is going to be used for the quality assessment?
- (e) How is the data going to be obtained?

1.2. Research framework

The thesis begins with analyzing the HeliX-tool to fully understand the model. This analysis is described in [Chapter 2](#) after which a sensitivity analysis is performed to know how sensitive the model is to certain input parameters in [Chapter 3](#). A description of the experimental set-up and equipment of the outdoor noise measurements are given in [Chapter 4](#) which is followed by a detailed description of acquiring the propeller geometry in [Chapter 5](#) as the propeller geometry is an important input. The outdoor data of the noise measurements are processed and analyzed in [Chapter 6](#). The comparison and thus the validation of the outdoor data and HeliX-tool output is given in [Chapter 7](#) and the thesis ends with the conclusion and recommendations in [Chapter 8](#).

2

HeliX-tool Analysis

This chapter describes the analysis of the aircraft propeller noise model made by M. Haddaoui called HeliX-tool [5]. It begins with explaining propeller noise in Section 2.1. This is followed by the description of the helicoidal surface theory in Section 2.2. Several assumptions and boundary conditions are used and these are given in Section 2.3. In addition to these assumptions, two external analysis tools are used in this model which are described in Section 2.4. The HeliX-tool methodology is given in Section 2.5 from which the input parameters of the model can be determined. These inputs are described in Section 2.6. The chapter ends with the outputs of the model in Section 2.7.

2.1. Propeller noise

Propeller noise is divided into two components namely the rotational and broadband noise sources [6]. Rotational noise is also known as periodic noise and it consists of the sound that is associated with discrete frequencies appearing at harmonics of the blade passage frequency, BPF. This is due to the fact that every time the blade passes a certain point, a pulse is created. The frequency of that pulse is related to the time between two passing blades and thus the peaks of the the pulses. The BPF is also known as the fundamental tonal frequency, f_1 [7] and is calculated by Equation 2.1.

$$BPF = B \frac{RPM}{60} \quad (2.1)$$

where B stands for the number of propeller blades. The higher harmonics are present as well and their frequencies (f_k) are multiples of the BPF (f_1) which are given by Equation 2.2 [7]. The higher harmonics are a result of the non-uniform inflow that the propeller encounters. The higher the non-uniform flow, the more velocity fluctuations are produced which give rise to a multitude of harmonics [6].

$$f_k = kf_1, k = 1, 2, 3.. \quad (2.2)$$

The periodic noise is divided into two sub-components namely the thickness and loading noise and the broadband noise is divided into the vortex noise and the turbulence induced noise. These sub-components are explained below.

Thickness noise

Thickness noise propagates along with the disc and can be described as the noise that is created due to the displacement of air in the disc by the thickness of the blade [6]. When the frame of reference is fixed, this movement of air is equal to a periodic addition and removal of mass at every element of air close to the disc. This can be represented as the strength of an array of monopole sources along the blade. A monopole source can be considered as pulsating sphere, radiating the sound equally in every direction. Any sound source with smaller dimensions than the wavelength of the sound will be seen as a monopole source [8]. These monopole sources will be pulsating every time the blade passes, just as with the dipole array of the loading noise. The monopole as pulsating sphere is shown in Figure 2.1 [6].

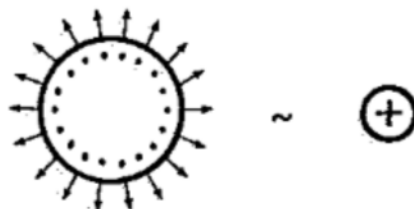


Figure 2.1: Monopole sound source [6]

Thickness noise is usually found to be small compared to the loading noise when the Mach number is lower than 0.7, however, when the speed increases at the tip, the significance of thickness noise increases and may even be similar to that of the loading noise [6].

Loading noise

Loading noise is determined by the blade pressure distribution that is generated when the blades move relative to the medium that surrounds them [6]. This distribution can be resolved into a thrust and torque component normal to the plane and in the plane of rotation respectively. This means that the air that is in contact with the propeller has a force working on it which is resolved in thrust and torque vectors.

Loading noise can either be steady or unsteady. Steady loading noise is created when operating at uniform inflow conditions, then this pressure field on the air is steady relative to the blade and rotates with the blade [6].

Unsteady loading noise is associated with non-uniform flow, which results in a variance in blade loading and incidence angle.

The loading noise is generated by moment injection and has a magnitude and direction. Therefore it can be described by an array of dipoles in the plane of rotation. The loading noise is assumed to be strongest at a θ of 0° and 180° , because the noise is related to the thrust and torque vector, also interpreted as the lift and drag vector. The definition of θ is given in Figure 2.5. An acoustic dipole can be considered as a force located at a point with a different magnitude and direction. Every time the blade passes, the array of dipoles is activated which results in pulses that create the peak at the BPF and higher harmonics. The dipole with its alternate forms can be seen in Figure 2.2 [6].

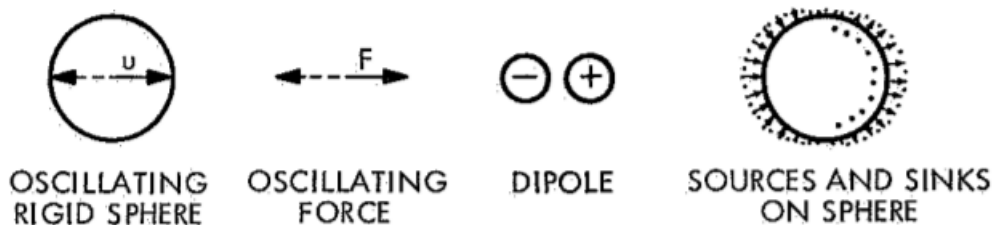


Figure 2.2: Alternate forms of dipole sound source [6]

Vortex noise

The biggest contribution to broadband noise is vortex noise [6]. It is described as the sound that is caused by the shedding and formation of vortices from the tips and trailing edge of the propeller blades in the airflow. It is also associated with some of the noise sources associated with turbulence appearances in the airflow.

Turbulence induced noise

Another contribution to the broadband noise is the turbulence induced noise which is generated by the small-scale motion of the turbulence airflow [6]. Turbulence induced noise is represented as quadrupole sources, which is shown in Figure 2.3.

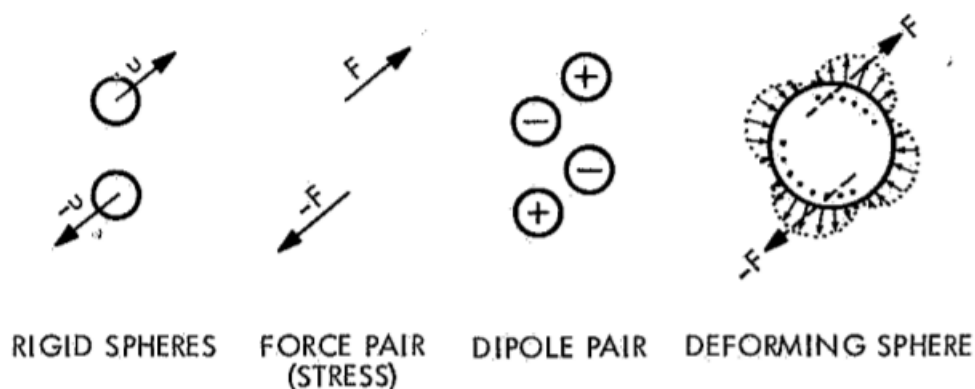


Figure 2.3: Alternate forms of quadrupole sound source [6]

It has a low contribution in the presence of other noise sources because it is inefficiently radiated. This is because

there is no net force on the fluid or net flux of fluid. The fluctuating stress on the fluid generates the sound waves, but fluids do not support stresses well which is the reason why quadrupoles are radiating sound poorly [8]. However, when interacting with the pressure field of the moving blade, the radiation of noise can become a dipole source and should be taken into account.

2.2. Helicoidal surface theory

The HeliX-tool only models the thickness and steady loading noise, meaning it omits the broadband noise. The propeller noise theory used in the HeliX-tool is called the Helicoidal Surface Theory, which is developed by Hanson [9]. Many other theories and methods are developed to model the noise sources, examples are the asymptotic theory by Crighton and Parry [10], the lifting line method and method of matched asymptotic expansion by Brouwer [11, 12] and the lifting surface theory also by Hanson [13]. All of these theories and methods are reducing the computational cost of the numerical integration of the integrals of the governing sound equation. This numerical integration is needed for an accurate and detailed evaluation. The governing sound equation, given by Equation 2.3, is found by Ffowcs and Hawkings [14] which is based on the research in aerodynamic sound conducted by Lighthill in 1952 & 1954 [14]. Each integral in the equation represents a noise source, namely from left to right, the Lighthill quadrupole, loading (dipole), and thickness (monopole) noise [10].

$$4\pi c^2(\rho(X, t) - \rho_0) = \frac{\partial^2}{\partial x_i \partial x_j} \int \left[\frac{T_{ij} J}{r|1 - M_r|} \right] d\eta - \frac{\partial}{\partial x_i} \int \left[\frac{p_{ij} n_j A}{r|1 - M_r|} \right] dS(\eta) + \frac{\partial}{\partial t} \int \left[\frac{\rho_0 v_n}{r|1 - M_r|} \right] dS(\eta) \quad (2.3)$$

The Helicoidal Surface Theory derives the far-field radiation equations by representing the blades as a helicoidal surface, hence the name [9]. The far-field is defined as the distance where the near field ends and continues to infinity [15]. The near-field is the area close to the source. Here, the acoustic particle speed and sound pressure are not in phase and the sound field does not reduce by 6 dB every time the distance from the source is expanded. The near field ends either at a distance from the source equivalent to approximately a wavelength of sound or equal to three times the biggest dimension of the sound source. The larger distance of the two, determines the distance of the near-field.

The effect of the blade loading, blade thickness, blade sweep and forward flight is included in this theory. The forward flight is included by the addition of a Doppler shift term. This alters the frequency that is heard by the observer which depends on the location of the observer with respect to the source and the relative velocity between the two.

Blade sweep is taken into account as a phase lag effect. This phase lag is given by Equation 2.4 and a detailed explanation is found in Haddaoui [5]. As the propeller in Haddaoui [5] has no blade sweep, this phase lag effect is neglected.

$$\phi_s = \frac{2mBM_T}{M_r(1 - M_x \cos(\theta))} \frac{MCA}{D} \quad (2.4)$$

where m is the number of harmonics, M_T is the rotational tip Mach number, M_r is the effective Mach number, M_x is the flight speed Mach number, D is the diameter of the propeller, θ is the radiation angle from propeller axis to observer point, and MCA is the Mid Chord Alignment. M_r is calculated by Equation 2.5 where the z equals the radial position of a blade element as a fraction of the radius.

$$M_r = \sqrt{M_x^2 + z^2 M_T^2} \quad (2.5)$$

The θ is shown in Figure 2.5, where the distances y and r are given as well. The y is the altitude and the r is the distance between the observer and source at time of emission.

It is also possible to include a phase lag due to offset. This is given by Equation 2.6, where FA is the Face Alignment which is the distance at the tip normal to the blade surface. The MCA and FA are shown in Figure 2.4.

$$\phi_0 = \frac{2mB}{zM_r} \left(\frac{M_r^2 \cos\theta - M_x}{(1 - M_x \cos(\theta))} \right) \frac{FA}{D} \quad (2.6)$$

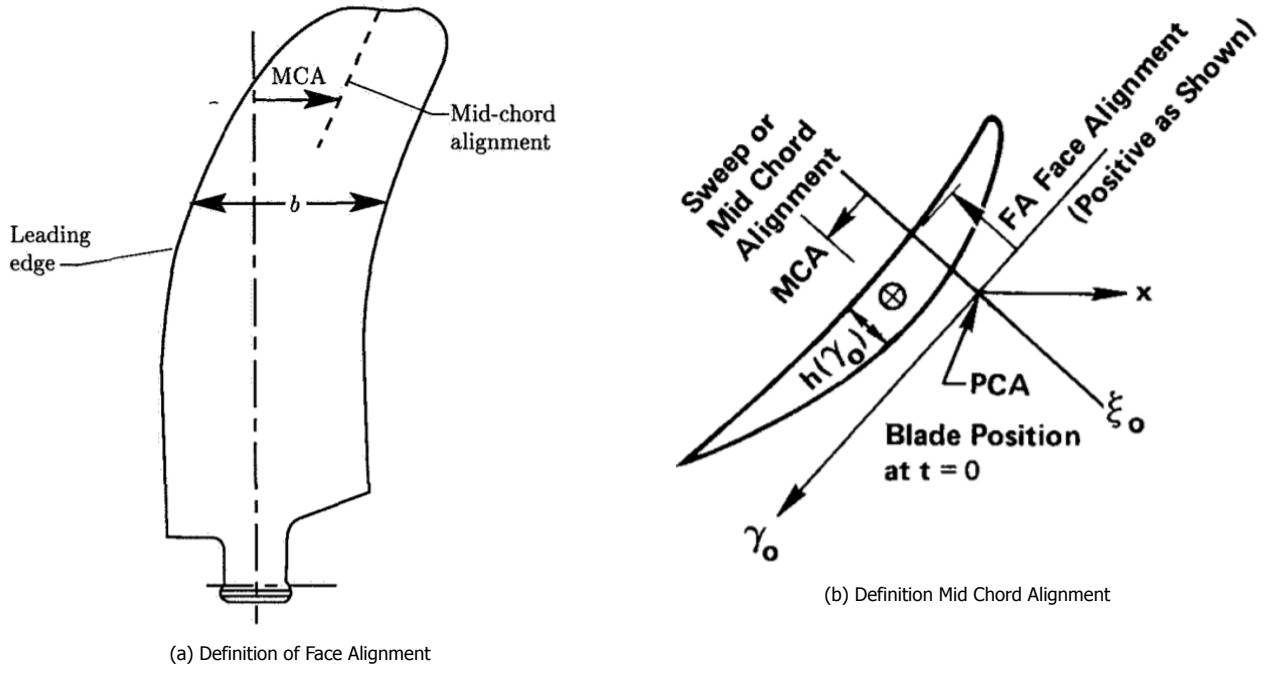


Figure 2.4: Definition of MCA and FA [16]

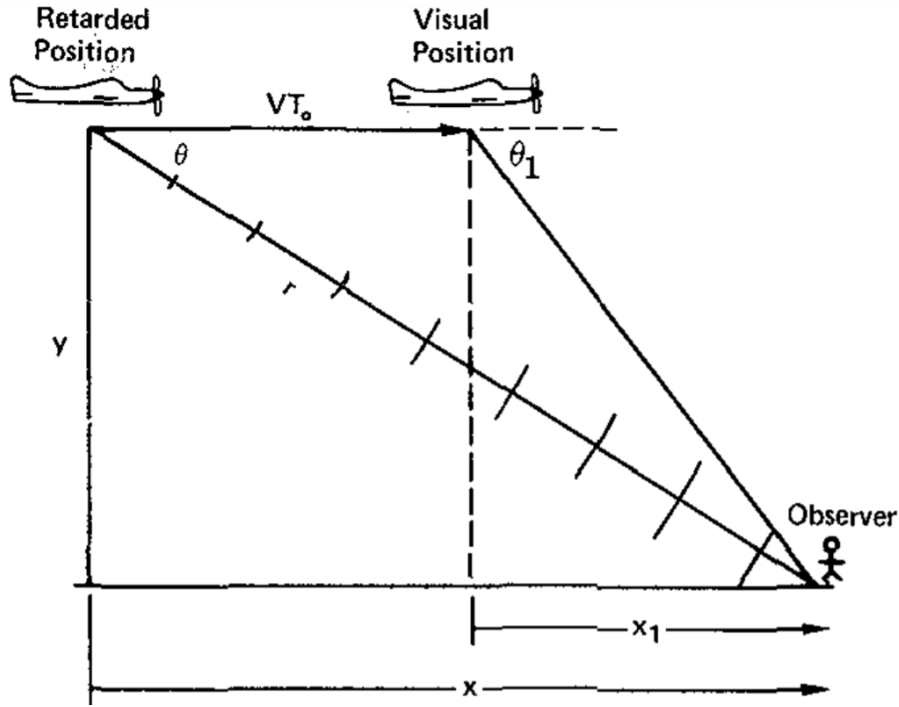


Figure 2.5: Definition of θ [9]

The thickness and loading sources are assumed to act on the advance helix. This helix is the surface swept by a radial line and rotates at a certain angular velocity and moves forward with the flight velocity. The propeller blade loading can be established when the angle of attack is determined with respect to the helical surface. From this, the harmonic sources in the frequency domain can be obtained using the helicoidal surface theory by Hanson [9]. Simplified mathematical expressions are obtained to model the steady thickness noise and loading noise starting with the expression for the acoustic pressure given by Equation 2.7.

$$p(t) = \sum_{m=-\infty}^{\infty} P_{mB} \exp(-imB\Omega_D t) \quad (2.7)$$

where where P_{mB} equals the Fourier transform of the pressure at the m th harmonic of the BPF [5]. The P_{mB} consists of the P_{Vm} , P_{Dm} and P_{Lm} , which are the volume displacement component, drag dipole and lift dipole respectively and given by Equation 2.8, Equation 2.9 and Equation 2.10. These are the components that model the thickness and loading noise.

$$P_{Vm} = -\frac{\rho_0 c_0^2 B \sin \theta \exp \left[imB \left(\frac{\Omega_D r}{c_0} - \frac{\pi}{2} \right) \right]}{8\pi \left(\frac{\gamma}{D} \right) (1 - M_x \cos \theta)} x \frac{1}{2} \int_{root}^{tip} M_r^2 e^{i(\phi_0 + \phi_s)} J_{mB} \left(\frac{mBz M_t \sin \theta}{1 - M_x \cos \theta} \right) x 2k_x^2 t_b \psi_V(k_x) dz \quad (2.8)$$

$$P_{Dm} = -\frac{\rho_0 c_0^2 B \sin \theta \exp \left[imB \left(\frac{\Omega_D r}{c_0} - \frac{\pi}{2} \right) \right]}{8\pi \left(\frac{\gamma}{D} \right) (1 - M_x \cos \theta)} x \frac{1}{2} \int_{root}^{tip} M_r^2 e^{i(\phi_0 + \phi_s)} J_{mB} \left(\frac{mBz M_t \sin \theta}{1 - M_x \cos \theta} \right) x i k_x C_D \psi_D(k_x) dz \quad (2.9)$$

$$P_{Lm} = -\frac{\rho_0 c_0^2 B \sin \theta \exp \left[imB \left(\frac{\Omega_D r}{c_0} - \frac{\pi}{2} \right) \right]}{8\pi \left(\frac{\gamma}{D} \right) (1 - M_x \cos \theta)} x \frac{1}{2} \int_{root}^{tip} M_r^2 e^{i(\phi_0 + \phi_s)} J_{mB} \left(\frac{mBz M_t \sin \theta}{1 - M_x \cos \theta} \right) x - i k_y C_L \psi_L(k_x) dz \quad (2.10)$$

Here, i is the imaginary number defined as $i^2 = -1$, m is the number of harmonics and t_b is the maximum thickness to chord ratio which is determined in the HeliX-tool. The k_x and k_y are the non-dimensional wave numbers defined as given by Equation 2.11 and Equation 2.12.

$$k_x = \frac{2mBB_D M_t}{M_r (1 - M_x \cos \theta)} \quad (2.11)$$

$$k_y = \frac{2mBB_D}{zM_r} \left(\frac{M_r^2 \cos \theta - M_x}{1 - M_x \cos \theta} \right) \quad (2.12)$$

Here, B_D is the chord to diameter ratio. The ψ_V , ψ_D and ψ_L are distribution functions and represent the distribution of the thickness, lift and drag components respectively. These are given by Equation 2.13, Equation 2.14 and Equation 2.15.

$$\psi_V(k_x) = \int_{-0.5}^{0.5} H(x) e^{ik_x x} dx \quad (2.13) \quad \psi_D(k_x) = \int_{-0.5}^{0.5} f_D(x) e^{ik_x x} dx \quad (2.14) \quad \psi_L(k_x) = \int_{-0.5}^{0.5} f_L(x) e^{ik_x x} dx \quad (2.15)$$

The $H(x)$ is a normalized thickness distribution of the airfoil coordinates and is dependent on the radial position of the blade section. The maximum of $H(x)$ is 1, and the integration is performed from -0.5 to 0.5 which represents the leading edge and the trailing edge of the airfoil. The f_L and f_D represent the assumed chordwise lift and drag distribution used in the HeliX-tool. The distributions are graphically depicted in Figure 2.6 and Figure 2.7 [5].

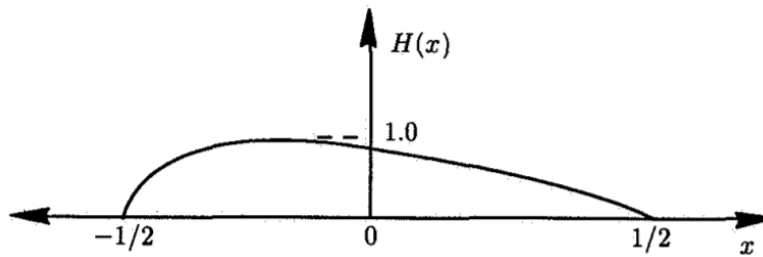


Figure 2.6: Normalized thickness distribution used in the HeliX-tool [5]

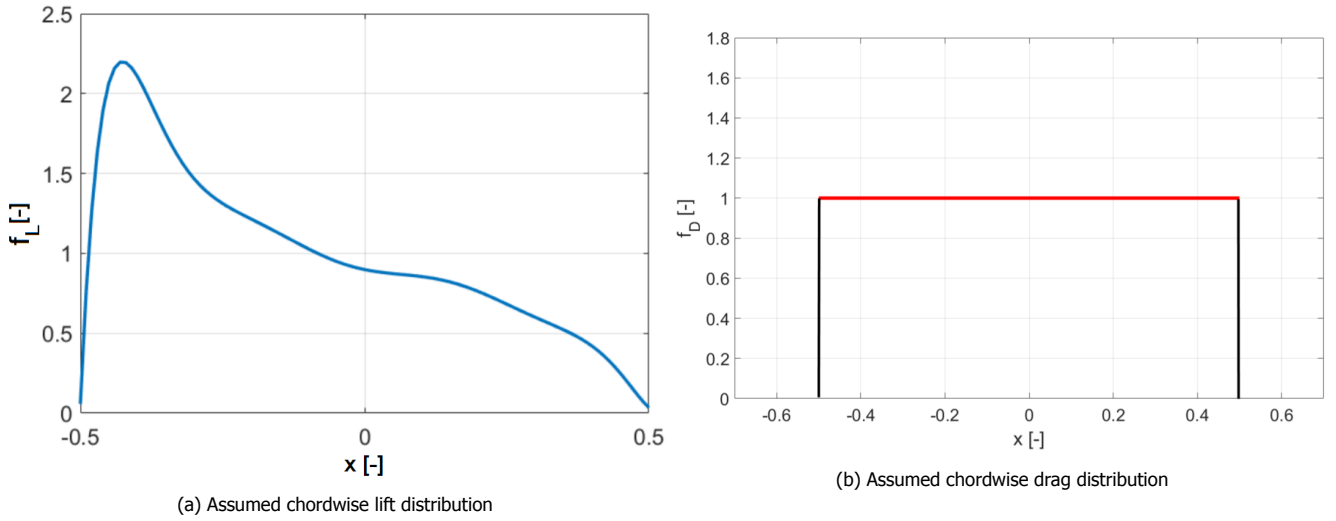


Figure 2.7: Assumed lift and drag distribution used in the HeliX-tool [5]

In addition to using this theory, several assumptions and boundary conditions are used which are described in the following section.

2.3. HeliX-tool assumptions and limitations

The assumptions and their implications are given below:

- Blade of propeller has no sweep, meaning the phase lag effects can be omitted. It is expected that the model will give higher noise levels than when the blade is swept, this is because swept blades reduce the noise emission [17].
- Propeller operates in an isolated configuration and has only an axial inflow, meaning there is no additional inflow velocity that is added to the velocity term that the blade encounters and thus no periodical variation in angle of attack and no asymmetric loading. Only symmetric and steady loading is obtained by only axial flow. It is expected that the model will give lower noise levels, as the operating conditions are idealized, while in reality this is not the case.
- XRotor uses a Prandtl-Glauert compressibility correction which should not be applied for Mach numbers higher than 0.7.
- The propeller noise sources that are taken into account are the harmonic noise sources: steady loading noise and the thickness noise. Mach numbers above 1 are avoided and the quadrupole sources being present in the broadband noise are omitted. It is expected that the model will give lower noise levels, as the model leaves the broadband noise out of the calculation, while this will be present when conducting an experiment.

The HeliX-tool also makes use of the two external analysis tools for the computation of the noise emission. These two external tools are described in the following section.

2.4. External analysis tools

The Helicoidal Surface Theory needs several aerodynamic parameters for the calculation of the noise emission. These parameters are obtained by using XFOIL and XRotor. Their function within the HeliX-tool is briefly described in Subsection 2.4.1 and Subsection 2.4.2 respectively.

2.4.1. XFOIL

XFOIL is a tool designed by M. Drela [18] and used for the development and analysis of subsonic airfoils. The purpose of XFOIL is to obtain the 2D aerodynamic properties of the propeller blade that are needed as input for XRotor. The input for XFOIL are the NACA airfoil coordinates of every radial propeller blade section, the range in angle of attack, α , and the Reynold's number, Re , that corresponds to the radial blade section. For every radial blade section the lift coefficient, C_l , drag coefficient, C_d , moment coefficient, C_m and corresponding α 's will be calculated.

In XFOIL the setting that affects the boundary layer around the airfoil is changed by using the so-called e^n method. This method simulates the effect of disturbances at the transition point of laminar to turbulence flow. Changing the n -value, the transition point shifts and the turbulence level changes. The default value for n is 9 in XFOIL, which equals the condition of an average windtunnel. However, the value for n is changed to 0.01, because according to a sensitivity study performed by Klein [19], the smallest deviations between the performance coefficients computed by XRotor and experimentally found are obtained using that value. This n value is also used in Haddaoui [5].

2.4.2. XRotor

XRotor is a program that is used for the design and analysis of free-tip and ducted propellers and windmills [20]. It has various functions, but for the HeliX-tool it is needed to acquire the performance coefficients, C_p and C_t , of the propeller blade. Before XRotor is run to obtain the performance parameters, XRotor is used to perform a fitting of the 2D aerodynamic properties given by XFOIL and obtain other aerodynamic characteristics. The output of XFOIL is the input of this fitting and the output of this fitting is given in Table 2.1.

Symbol	Description	Unit	Symbol	Description	Unit
α_{0L}	Zero lift angle of attack	°	C_{l0}	Zero lift coefficient at minimum Cd	—
$\frac{dC_l}{d\alpha}$	Lift gradient	—	$C_{LC_{dmin}}$	Lift coefficient at minimum Cd	—
$\left(\frac{dC_l}{d\alpha}\right)_{stall}$	Lift gradient at stall	—	C_{dmin}	Minimum drag coefficient	—
C_{Lmax}	Maximum lift coefficient	—	C_m	Pitching moment coefficient	—
C_{Lmin}	Minimum lift coefficient	—	$\frac{dC_d}{dC_l^2}$	Quadratic coefficient	—
ΔC_l	Increment in lift to stall	—			

Table 2.1: Output parameters of the fitting

The output parameters of the fitting and the critical Mach number, M_{crit} , Reference Reynolds number, Re_{ref} and Reynolds number scaling component, f_{Re} , are the input variables of the performance analysis performed by XRotor. The f_{Re} is a parameter that is used in XRotor to scale the drag coefficient. This is set to zero because XFOIL and XRotor are run for one operational condition, meaning that the local Re_{ref} and Re are equal to each other.

The output of the performance analysis of XRotor gives the performance parameters C_p and C_t which are the power and thrust coefficient respectively.

Within XRotor there are three methods implemented to calculate the induced velocities and induced losses [20] which are the *graded momentum formulation*, the *potential formulation* and the *vortex formulation*. The first method is the least computational expensive and the last the most. For the HeliX-tool the potential formulation is chosen as the propeller blade has no sweep. The graded momentum formulation is not suitable as this method is only used for advance ratios below 0.5 and the vortex formulation will unnecessarily increase the computational time. The advance ratio will be explained in Section 2.6.

2.5. HeliX-tool methodology

The HeliX-tool is built from three major processes which are the aerodynamic calculation, the performance calculation, and the noise calculation, thereby solving for Equation 2.3. The flow of these processes is given in the flowchart in Figure 2.8. The yellow blocks represent the outputs of XFOIL, XRotor and the HeliX-tool.

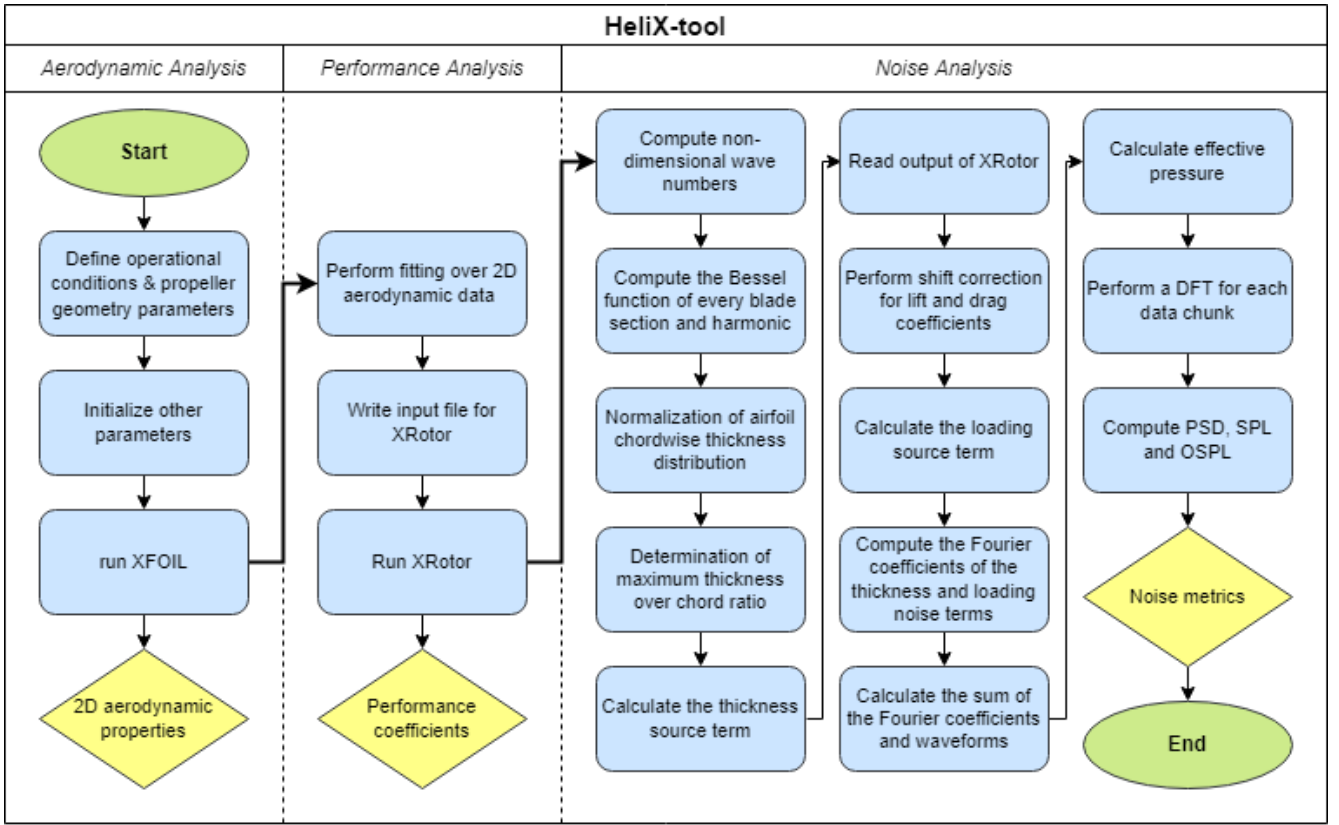


Figure 2.8: Flowchart of HeliX-tool

Within the noise calculation, there is a distinction between the thickness and steady loading noise. This is because the thickness noise calculation is independent of the output of XRotor as it is only dependent on the airfoil thickness distribution and effective Mach number and not the loading of the blade.

Before XFOIL can be run, the operational conditions and propeller geometry files need to be defined. Other variables such as the number of blades and harmonics are also determined. The variables such as the helical tip Mach number, M_h , rotational tip Mach number, M_t , flight speed Mach number, M_x , advance ratio, J , and BPF are calculated before XFOIL is run. After XFOIL is run, and the aerodynamic properties are obtained, the fitting is performed and XRotor is run.

Now, all the parameters needed to start the noise level computation implementing the Helicoidal Surface Theory have been obtained. The noise computation starts with the calculation of the non-dimensional wave numbers and local effective Mach number, M_r , after which the Bessel function for every blade section and the harmonic number is defined. The exact formulas for these parameters can be found in Haddaoui [5]. Then the airfoil chordwise thickness distribution is normalized, the maximum thickness over chord ratio is determined for every blade section and the thickness source distribution is computed after which the Fourier coefficients of the thickness noise are calculated.

The data from XRotor is written and saved in a data file, which is read to obtain the parameters needed for the shift correction for lift and drag coefficients. This shift correction is needed due to the generation of the induced velocities. The loading source distribution is calculated after which the Fourier coefficients of the loading noise are computed.

The final phase of the noise calculation starts with summing the Fourier coefficients. Then the waveforms are calculated. From this the effective pressure and overall sound pressure level, OSPL, are determined while a discrete fourier transform, DFT, for each chunk of data is performed. The power spectral density, PSD, and the sound pressure level, SPL, are computed corresponding to the frequency bands and the results are plotted.

Several input parameters have already been touched upon but the following section will go into detail about the input parameters, which is followed by the description of the output parameters in Section 2.7.

2.6. HeliX-tool input

There are several parameters that need to be known before the HeliX-tool can be run. These are initialized in the main file and are listed in Table 2.2.

Symbol in code	Meaning	Unit	Symbol in code	Meaning	Unit
<i>rho</i>	Density	$\frac{kg}{m^3}$	<i>M_{cr}</i>	Critical Mach number	—
<i>dvo</i>	Dynamic viscosity	$\frac{kg}{s \cdot m}$	<i>V_x</i>	Axial flight speed	$\frac{m}{s}$
<i>diameter</i>	Diameter	<i>m</i>	<i>rpm</i>	Revolutions per minute	$\frac{rev}{min}$
<i>radius</i>	Radius	<i>m</i>	<i>*rps</i>	Revolutions per second	$\frac{rev}{s}$
<i>c</i>	Speed of sound	$\frac{m}{s}$	<i>*Omega</i>	Angular speed	$\frac{rad}{s}$
<i>n_i</i>	Number of points radially	—	<i>*Omega_D</i>	Doppler shifted angular speed	$\frac{rad}{s}$
<i>m</i>	Number of harmonics	—	<i>*M_t</i>	Rotational tip Mach number	—
<i>*M_x</i>	Flight axial Mach number	—	<i>altitude</i>	Altitude	<i>m</i>
<i>*advance_ratio</i>	Advance ratio	—	<i>*adv</i>	Advance coefficient	—
<i>beta0</i>	Blade angle at 0.75%R	°	<i>rake</i>	Rake angle	°
<i>Re_{exp}</i>	Reynolds scaling factor	—	<i>hub_location</i>	Hub location r/R	—
<i>nblades</i>	Number of blades	—	<i>phase_0</i>	Phase shift due to offset	°
<i>t_{end}</i>	Duration of propeller signal	<i>s</i>	<i>phase_s</i>	Phase shift due to sweep	°
<i>f_s</i>	Sampling frequency	<i>Hz</i>	<i>*BPF</i>	Blade passage frequency	<i>Hz</i>
<i>dt</i>	Sampling time	<i>s</i>	<i>*M_h</i>	Helical tip Mach number	—
<i>t</i>	Time	<i>s</i>			

Table 2.2: Variables with fixed values

Not all of the variables in Table 2.2 need to be given a user input in the code, the parameters with an (*) are computed by the model itself. These are calculated by Equation 2.16 to Equation 2.24. Here, R is the radius of the propeller blade and the BPF is calculated by Equation 2.1 given in Section 2.1.

$$M_x = \frac{V_x}{c} \quad (2.16)$$

$$J = \frac{V_x \cdot 60}{RPM \cdot D} \quad (2.17)$$

$$dt = \frac{1}{f_s} \quad (2.18)$$

$$rps = \frac{RPM}{60} \quad (2.19)$$

$$\Omega = \frac{2\pi RPM}{60} \quad (2.20)$$

$$\Omega_D = \frac{\Omega}{1 - (M_x \cos(\theta))} \quad (2.21)$$

$$M_t = \frac{\Omega R}{c} \quad (2.22)$$

$$adv = \frac{V_x}{\Omega \cdot R} \quad (2.23)$$

$$M_h = \sqrt{M_x^2 + M_t^2} \quad (2.24)$$

The helical tip Mach number, M_h , is the highest Mach number present and calculated by Equation 2.24. The helical tip Mach number should not be higher than 0.7, as the Prandtl-Glauert compressibility correction used in XRotor cannot be used when the value of 0.7 is surpassed.

The advance ratio, J , provides an indication of the loading of the propeller. The advance ratio allows the determination of the performance coefficients of the propeller, which are needed to calculate the noise parameters [5]. In Figure 2.9 one can see the relationship between the helical tip Mach number and the advance ratio for different M_x .

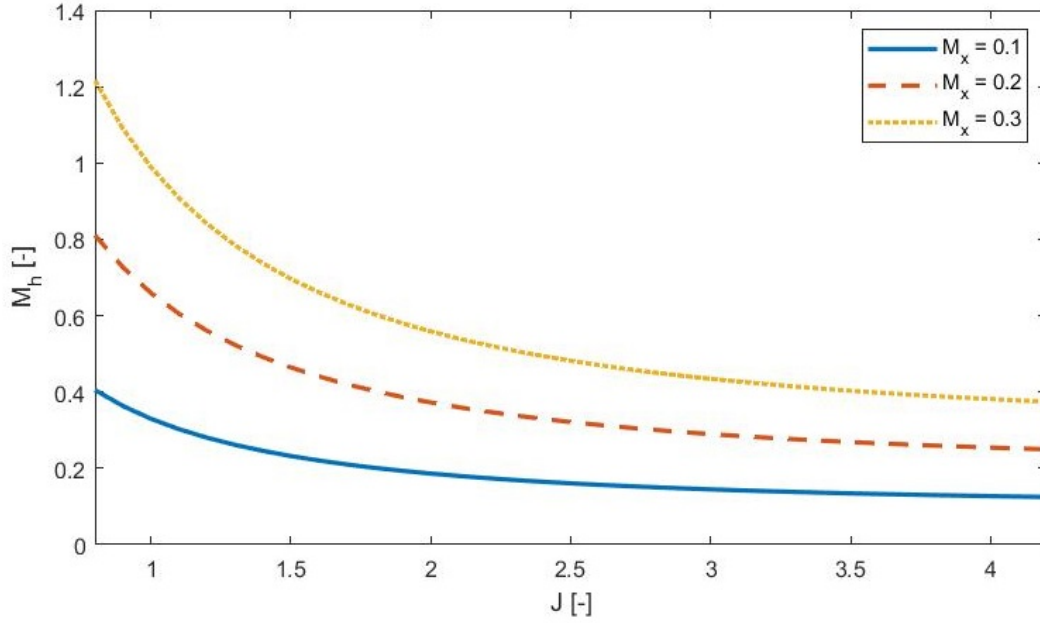


Figure 2.9: Helical tip Mach number as a function of the advance ratio J

From this figure it can be concluded that the helical tip Mach number decreases with increasing advance ratio for a fixed value of M_x . This is logical as a high advance ratio equals a low propeller loading because a high J means a high V_x and/or low RPM. If the M_x is fixed, the V_x is fixed, which means that the RPM should be low for a high J, thus the M_t is low and the M_h decreases.

The M_{cr} is the critical Mach number which is the freestream Mach number of the airflow in front of the blade section for which the airflow over the blade section achieves sonic flow on the airfoil ($M = 1$) [21]. Knowing the M_{cr} is important as the airfoil experiences a drastic increase in drag coefficient when this M_{cr} is even slightly surpassed. The M_{cr} is found by using Equation 2.25 and Equation 2.26, which present the minimum and critical pressure coefficient respectively.

$$(C_p)_{min} = \frac{(C_{p,0})_{min}}{\sqrt{1 - M_\infty^2}} \quad (2.25)$$

Here, $(C_{p,0})_{min}$ is the minimum pressure coefficient for the airfoil at an angle of attack of 0° and M_∞ is the flight speed Mach number.

$$C_{p,cr} = \frac{2}{\gamma M_{cr}^2} \left[\frac{(1 + (\frac{\gamma-1}{2})M_{cr}^2)}{(1 + \frac{\gamma-1}{2})} \right]^{\frac{\gamma}{\gamma-1}} - 1 \quad (2.26)$$

Here, γ is equivalent to the ratio between the specific heats of a gas at constant pressure, C_p and volume, C_v as given in Equation 2.27.

$$\gamma \equiv \frac{C_p}{C_v} \quad (2.27)$$

The M_{cr} is found by setting Equation 2.25 and Equation 2.26 equal to each other, so $C_{p,cr} = (C_p)_{min}$. As γ and M_∞ are known, the only parameter left to be determined is the $(C_{p,0})_{min}$. This parameter is obtained by using another tool called JavaFoil which is a similar tool as XFOIL. The airfoil coordinates of every propeller blade section is imported into JavaFoil, from which the $(C_{p,0})_{min}$ is obtained. Now, every parameter is known to find the M_{crit} for which $C_{p,cr} = (C_p)_{min}$. Their values are given in Table 2.3.

Sections	M_{crit} [-]	Section	M_{crit} [-]	Section	M_{crit} [-]
1	0.557	7	0.605	13	0.644
2	0.532	8	0.619	14	0.638
3	0.538	9	0.624	15	0.634
4	0.556	10	0.605	16	0.642
5	0.577	11	0.629	17	0.652
6	0.602	12	0.624	18	0.598

Table 2.3: M_{crit} for all 18 blade sections

Detailed information about how the values of β_{a_0} ($\beta_{0.75}$), V_x , RPM, and altitude, (h) are found is given in [Section 6.1](#).

Besides the initial parameters, there are several input files needed as well. These are the following:

- Geometry of the propeller in the files: *betadata_Sr2.mat*, *chord_Sr2.mat* and *thicknessdata_Sr2.mat*. These are the blade pitch distribution, blade chord over diameter distribution and the thickness over chord distribution data of the SR-2 propeller defined per radial section respectively. The *betadata_Sr2.mat* file consists of the variables *delta_beta* and *radial*, the *chord_Sr2.mat* file consists of the variables *chord* and *radial_c* and the *thicknessdata_Sr2.mat* file consists of the variables *r_R_Sr2* and *thick_Sr2*.
- Normalized airfoil coordinates for every section in the files: rR024 - rR100.txt. There are 18 sections, thus 18 files in total. The names of each of the data files of the sections is given in [Table 2.4](#).

Sections	Name of file	Section	Name of file	Section	Name of file
1	rR024.txt	7	rR045.txt	13	rR075.txt
2	rR027.txt	8	rR050.txt	14	rR080.txt
3	rR030.txt	9	rR055.txt	15	rR085.txt
4	rR032.txt	10	rR060.txt	16	rR090.txt
5	rR034.txt	11	rR065.txt	17	rR095.txt
6	rR037.txt	12	rR070.txt	18	rR100.txt

Table 2.4: File names of normalized airfoil coordinates of each section

- NACA airfoil coordinates in the files: NACA00xx, NACAxx.txt, 16series1.txt and 65series. These are needed for the thickness normalization of the airfoil of the propeller blade. More information about the thickness normalization is found in Haddaoui [5].

Intermediate outputs of the model which are inputs for the noise calculation are the *Sr2_data* file, *induced_v_axial*, *induced_v_tangential* and *alfadata.dat* generated by the *xrotor* function. The *Sr2_data* file gives the free tip potential formulation solution of the SR2 propeller, this file contains among others the thrust coefficient, C_t , the power coefficient, C_p , the blade pitch angle, β , the lift coefficient, C_L , and drag coefficient, C_D , per blade section. The *induced_v_axial* and *induced_v_tangential* files give the axial and tangential velocity components for every blade section. The *alfadata.dat* file contains the angle of attack, α , and lift coefficient, C_l , per blade section.

Knowing the inputs of the HeliX-tool, the output parameters are described in the following section.

2.7. HeliX-tool output

The intermediate output parameters of the HeliX-tool are the performance coefficients C_p and C_t which are obtained from XRotor. This intermediate result can be checked with data to see whether XFOIL and XRotor are working accordingly. However, when performing noise measurements, the instruments will only measure the noise levels and not the performance of the aircraft.

The final output of the model are the noise parameters modelled at microphone level. These are shown in frequency spectra and directivity plots. In the frequency spectra plot, the total SPL values are plotted against the frequency, while in the directivity plot, the OSPL values are plotted against the θ . SPL is the sound pressure level and the OSPL is the overall sound pressure level. These noise metrics are further explained in [Section 6.2](#). The plots are shown in [Figure 2.10](#).

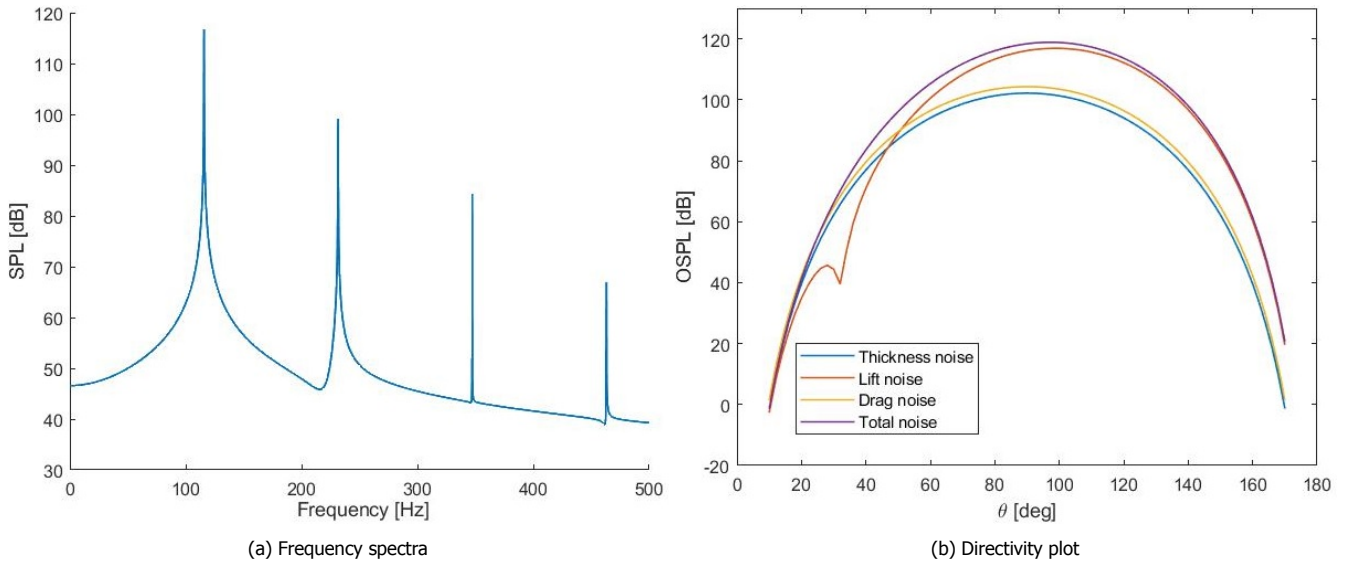


Figure 2.10: Noise metrics plots with $M_x = 0.35$, $J = 1.7$, $\beta_{0.75} = 45.8^\circ$

From [Figure 2.10a](#) it can be seen that the SPL values decrease with higher harmonics as expected. From [Figure 2.10b](#) it can be seen that the drag has the lowest contribution, after which the thickness and lift noise follow. These plots will be explained in more detail when the output of the HeliX-tool is compared to the data of the outdoor noise measurements. Before the HeliX-tool is run under the operating conditions and with the propeller geometry of the aircraft used for this thesis, a sensitivity analysis is performed to understand which parameters should be accurately determined. The full sensitivity analysis is given in the following chapter.

3

Verification of the HeliX-tool

During the generation of the HeliX-tool, some choices in the parameters, i.e. configurational and physical, are left to the developer of the model [22]. Sometimes, physical parameters are hard to find, non-existent, uncertain or requiring assumptions that could influence the accuracy of the output parameters of the model. It is therefore important to identify the input parameters that have the most influence on the output parameters of the model. This is being investigated by performing a sensitivity analysis with the operational conditions of Haddaoui and geometry of the SR2 propeller that he used during the modelling of the HeliX-tool. The sensitivity analysis is explained in [Section 3.1](#) which is followed by the method in [Section 3.2](#). The chapter ends with the results of the sensitivity analysis in [Section 3.3](#).

3.1. Sensitivity analysis

There are many sensitivity analysis methods and they are all important when developing a numerical model [23]. These methods allow the study of how the uncertainties of the outputs of the model relate to the uncertainties of the input parameters [24]. The purpose of these methods are many, i.e. model verification, model understanding, model simplifying and input parameter prioritization.

Before performing a sensitivity analysis, it is relevant to clearly specify the objective of the study as accentuated by Saltelli et al [24] and Pappenberger et al [25] as this will determine the type of method used. These objectives may be:

- Identify and prioritize the input parameters with the most influence.
- Identify non-influential inputs in order to fix them to nominal values.
- Outline the output behavior as a function of the inputs by focusing on a particular area of inputs if needed.
- Calibrate several model inputs making use of the information available (real output observations, constraints, etc.).

The objective of the sensitivity analysis method used for the HeliX-tool is to understand how much the inaccuracy in the input measurements influence the output of the model.

Before the execution of the sensitivity analysis it has become clear that some input variables found in [Table 2.2](#) are difficult to obtain or the values will be obtained with a certain margin. These variables are the following:

- $\Delta\beta$, the radial blade pitch angle distribution
- $\Delta\delta$, the radial thickness over chord distribution
- Δc , the radial chord over diameter distribution
- V_x , the axial flight speed
- RPM, the rotational speed
- $\beta_{0.75}$, the blade angle at 75%R

The propeller geometry is hard to find as the propeller is a commercial propeller and not a scientific one as was used when developing the HeliX-tool. The geometry is 3D scanned and processed in a computer aided design, CAD, program in order to obtain the geometry data files needed. The blade angle setting value of the propeller needs to be measured or calculated. The flight and rotational speed measurement instruments have a certain margin.

3.2. Sensitivity method

The V_x and RPM are related to each other with Equation 3.1. Therefore, the RPM is left out of the sensitivity analysis. J is kept constant during the sensitivity analysis. The radial blade pitch angle distribution, $\Delta\beta$, is also left out of this analysis as it represents the $\beta_{0.75}$ only in a different manner.

$$RPM = \frac{V_x \cdot 60}{JD} \quad (3.1)$$

All other variables mentioned before are changed with a logical and reasonable value. This value is determined by looking at the accuracy of the measurements or the measurement tools and are given in Table 3.1. All variables are changed both positively and negatively.

The C_t , C_p and the total sound pressure level, SPL, values are the metrics that will be compared during the sensitivity analysis. The total sound pressure level consists of the thickness and loading noise combined. The SPL values are given in absolute value for the baseline case and is absolute difference in SPL value for the other cases. The baseline case has the operational conditions: $\beta_{0.75} = 35^\circ$, $M_x = 0.35$ and $J = 1.4$. The C_t and C_p coefficients represent the performance of the propeller and the SPL values give a representation of the noise emission. For the performance coefficients, C_p and C_t , the absolute values are given as well as the absolute difference. The absolute SPL values for the four harmonics are given and also presented in a frequency spectra plot. These metrics are compared to the initial values of C_t , C_p and SPL values. The method is summarized in Table 3.1 and the change in value has been determined from the inaccuracy of the input measurements.

Table 3.1: Sensitivity variables

Sensitivity variables	Initial value	Change in value	Comparison metrics
Δc	array	1%, 5%	C_t , C_p , SPL
$\Delta\delta$	array	1%, 5%	C_t , C_p , SPL
β_0	35 °	1°, 5°	C_t , C_p , SPL
V_x	120.05 m/s	1 m/s, 5 m/s	C_t , C_p , SPL

When performing the sensitivity analysis, it has become clear that XFOIL itself is also sensitive to changing operating conditions. Several times it did not find convergence for the range of angle of attacks given, which resulted in changing the step in α or the limit of the α array. If convergence is found, blade sections could be stalled, which is indicated with 's' in the data file that is created by XRotor. This 's' needs to be removed as the function textscan will give an error reading this. It is possible to have multiple sections stalled, so remove this 's' and run the main file after 'xrotor()' again. When the model finds stalled sections, the modelled C_t is lower than if no stalled sections are found, because the thrust is lower when sections are stalled.

Another message that can arise in the data file generated by XRotor, is "Not converged", even though XFOIL did find convergence for one of the α 's in the array. The data file still gives data, thus the code can be run up to the end and give the performance coefficients and noise metrics. However, these results need to be carefully interpreted as the results are doubtful and the results should not be considered in the sensitivity analysis. In the results below, a (C) represents a converged data file, while a (NC) represents a not converged data file.

3.3. Results

The results of the sensitivity analysis are shown in this section. It starts with the analysis of the blade pitch angle in Subsection 3.3.1, after which the axial flight speed is discussed in Subsection 3.3.2. The chord over diameter distribution and thickness over diameter distribution are found in Subsection 3.3.3 and Subsection 3.3.4 respectively.

3.3.1. Blade pitch angle

In Table 3.2 the absolute values and differences in C_p and C_t are given for $\beta_{0.75}$. It can be seen that for lower $\beta_{0.75}$, lower performance coefficients are obtained and vice versa for higher values of $\beta_{0.75}$. This corresponds to literature as in general, the C_p coefficient reduces with reducing $\beta_{0.75}$ as can be seen in Figure 3.1 [26]. And with decreasing C_p , the C_t decreases as well, for which relation is shown in Figure 3.2 [26].

Interesting are the negative values of the performance coefficients for a $\beta_{0.75}$ of 30° . A negative thrust coefficient

can be present when the drag force increases and becomes more than the thrust but in reality such a propeller would never be designed as a propeller should propel the aircraft forward and thus have a positive thrust coefficient.

Table 3.2: Values and differences of C_p , C_t for different $\beta_{0.75}$ with $M_x = 0.35$ and $J = 1.4$

β_0 [°]	Change in $\beta_{0.75}$ [°]	C_p [-]	C_t [-]	Difference in C_p [-]	Difference in C_t [-]
30	-5	-0.0249	-0.04112	-0.2962	-0.1873
34	-1	0.20545	0.10962	-0.0659	-0.0366
35	0	0.27135	0.14619	0	0
36	+1	0.33974	0.18189	0.0684	0.0357
40	+5	0.8689	0.3447	0.5976	0.1628

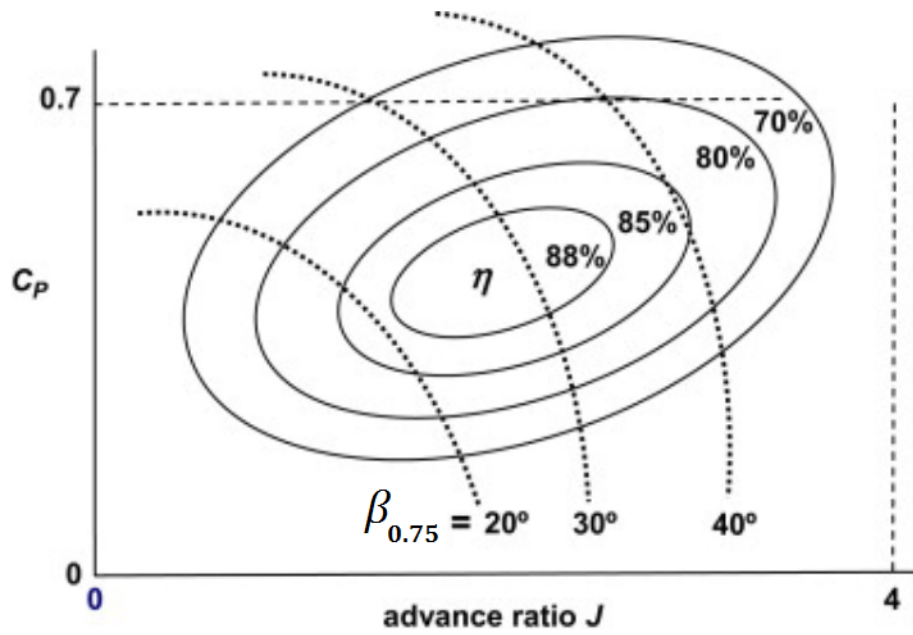


Figure 3.1: Typical propeller performance plot showing C_p as a function of J for several $\beta_{0.75}$ [26]

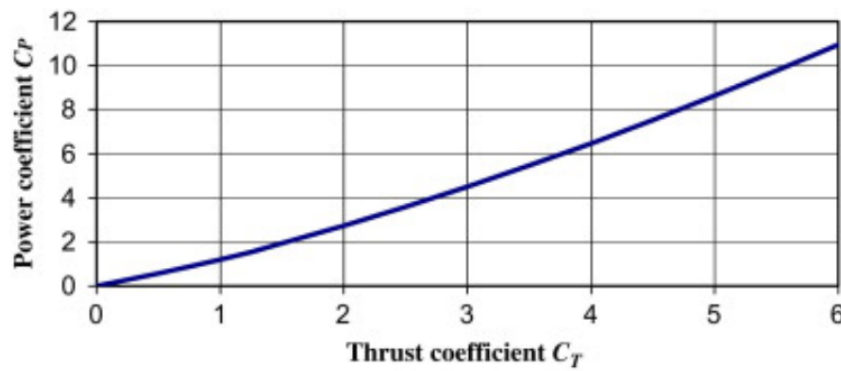


Figure 3.2: Relation between the performance coefficients, C_p and C_t [26]

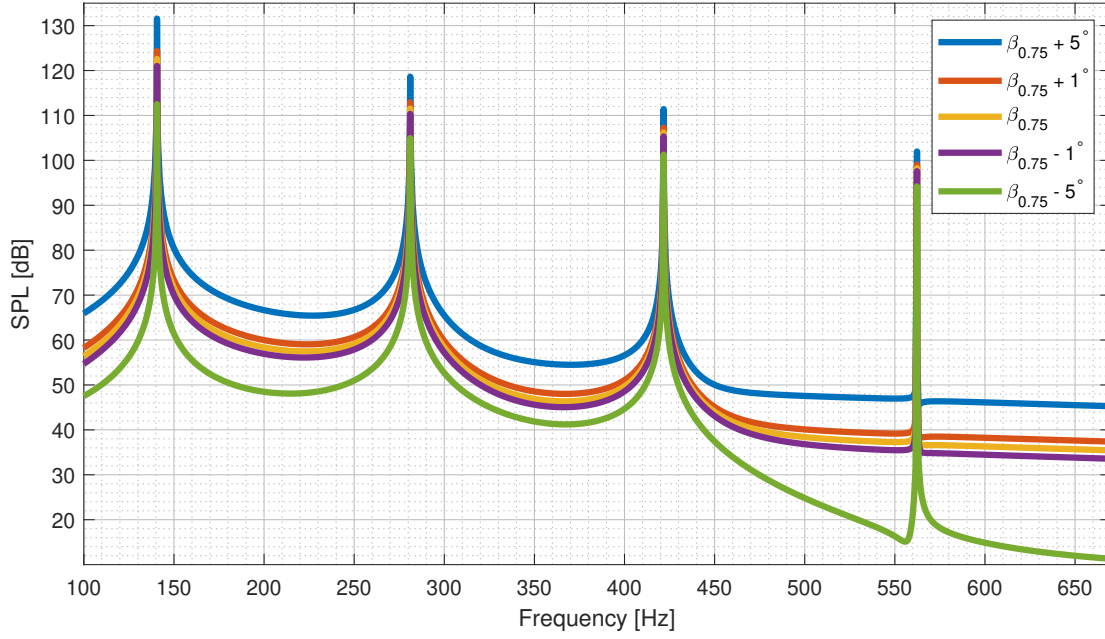


Figure 3.3: Frequency spectra of different $\beta_{0.75}$ values

The frequency spectra of different $\beta_{0.75}$ values are shown in Figure 3.3 and the four harmonics are clearly visible. The SPL values in dB of these peaks at the four harmonics are given in Table 3.3. The last column of the table presents the stalled blade sections if any are present.

As expected from Figure 3.1 and Figure 3.2, the highest $\beta_{0.75}$ resulted in the highest performance coefficients and thus also in the highest SPL value.

Table 3.3: SPL values of the four harmonics for different $\beta_{0.75}$ with $M_x = 0.35$ and $J = 1.4$

Change in $\beta_{0.75}$ [°]	1st harmonic Δ SPL	2nd harmonic Δ SPL	3rd harmonic Δ SPL	4th harmonic Δ SPL	stalled sections
-5 (C)	-10.072	-6.569	-4.916	-4.0392	-
-1 (C)	-1.572	-1.161	-0.866	-0.6622	-
0 (C)	122.593	111.519	106.198	98.2581	-
+1 (C)	1.746	1.425	1.096	0.8235	-
+5 (C)	8.953	7.117	5.206	3.723	12,13,14 15,17

3.3.2. Axial flight speed

In Table 3.4, the absolute value and difference in C_p and C_t is given for V_x . As the performance coefficients are a function of the flight speed as given by Equation 3.2 and Equation 3.3 [26], where P equals the power and F equals the thrust and rps is related to V_x by Equation 3.4, it is expected that with increasing flight speed, the performance coefficients would increase as well.

$$C_p = \frac{P}{\rho \cdot rps^3 D^5} \quad (3.2)$$

$$C_t = \frac{F}{\rho \cdot rps^2 D^4} \quad (3.3)$$

$$rps = \frac{V_x}{JD} \quad (3.4)$$

This is true for all, but the $V_x = 119.05m/s$ case. $V_x = 119.05m/s$ gives higher performance coefficients values. This can be the result of a poorly performed fitting of the lift curves in XRotor and this result is ignored for the conclusion of the sensitivity analysis.

Table 3.4: Values and differences of C_p , C_t for different V_x with $J = 1.4$ and $\beta_{0.75} = 35^\circ$

V_x [m/s]	Change in V_x [m/s]	C_p [-]	C_t [-]	Difference in C_p [-]	Difference in C_t [-]
115.05	-5	0.2625	0.14681	-0.0088	0.00062
119.05	-1	0.39423	0.15306	0.1229	0.0069
120.05	0	0.27135	0.14619	0	0
121.05	+1	0.2875	0.1526	0.0161	0.0064
125.05	+5	0.4142	0.1778	0.1429	0.0316

The frequency spectra of the different V_x values is plotted in Figure 3.5 from which can be seen that the BPF changes with V_x value. A higher flight speed results in a higher BPF. This makes sense as the axial flight speed changes the rotational speed, RPM, which is related to the BPF by Equation 2.1.

As expected, the highest performance coefficients result in the highest SPL values. This is also supported by the graph plotted in Figure 3.4 obtained from Dittmar [27]. Here it is shown that the SPL values increase with increasing helical tip Mach number, M_h , until a certain maximum is reached. And M_h is related to M_x and V_x with Equation 2.24 and Equation 2.16.

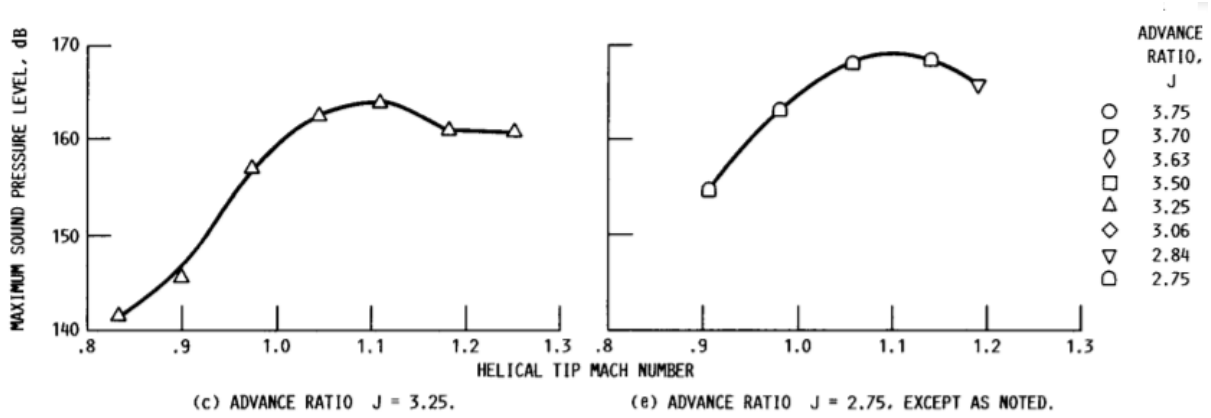


Figure 3.4: Maximum SPL value with respect to M_h [27]

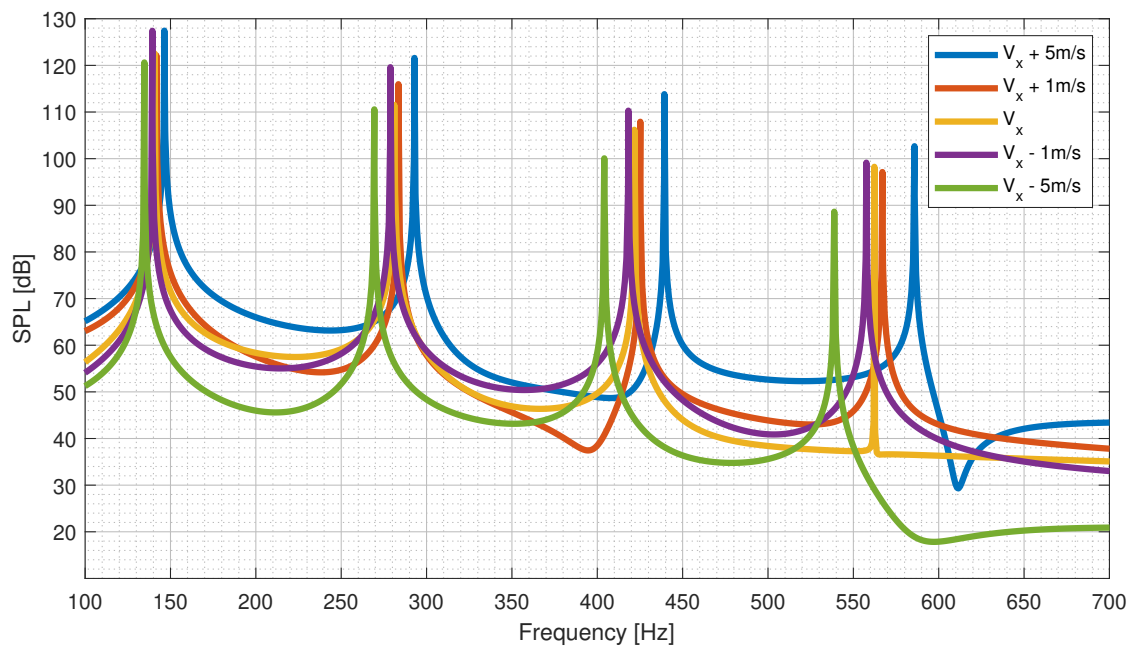


Figure 3.5: Frequency spectra of different V_x values

The absolute SPL values of the peaks are given in Table 3.5 from which can be seen that for three operating conditions blade sections are stalling. Thus these SPL values are higher then when the blade section would not be stalling.

Table 3.5: SPL values of the four harmonics for different V_x with $J = 1.4$ and $\beta_{0.75} = 35^\circ$

Change in V_x [m/s]	1st harmonic Δ SPL	2nd harmonic Δ SPL	3rd harmonic Δ SPL	4th harmonic Δ SPL	stalled sections
-5 (C)	-1.964	-0.949	-6.124	-9.6257	17,18
-1 (C)	4.826	8.093	4.095	0.8882	15,16
0 (C)	122.593	111.519	106.198	98.2581	-
+1 (C)	-0.433	4.450	1.718	-1.120	-
+5 (C)	4.859	10.078	7.634	4.4139	12

3.3.3. Radial chord over diameter distribution

The Δc is the chord of the blade section divided over the diameter. In Table 3.6, the absolute values and differences in C_p and C_t are given for Δc . There is no trend found in the value of the performance coefficient with increasing or decreasing Δc value. As the diameter of the propeller is constant, the chord length will increase or decrease. With an increase in chord length, the surface of the propeller blade increases and it is expected that the performance coefficients would increase because the surface area is higher, however, with a higher surface area, the drag and torque forces become higher as well reducing the performance coefficients.

Table 3.6: Values and differences of C_p , C_t for different Δc with $M_x = 0.35$, $J = 1.4$ and $\beta_{0.75} = 35^\circ$

Change in Δc [%]	C_p [-]	C_t [-]	Difference in C_p [-]	Difference in C_t [-]
-5	0.39646	0.16425	0.1251	0.0181
-1	0.24293	0.13329	-0.0284	-0.0129
0	0.27135	0.14619	0	0
+1	0.71772	0.19134	0.4464	0.0452
+5	0.28456	0.15310	0.0132	0.0069

The frequency spectra of the different Δc cases are shown in Figure 3.6.

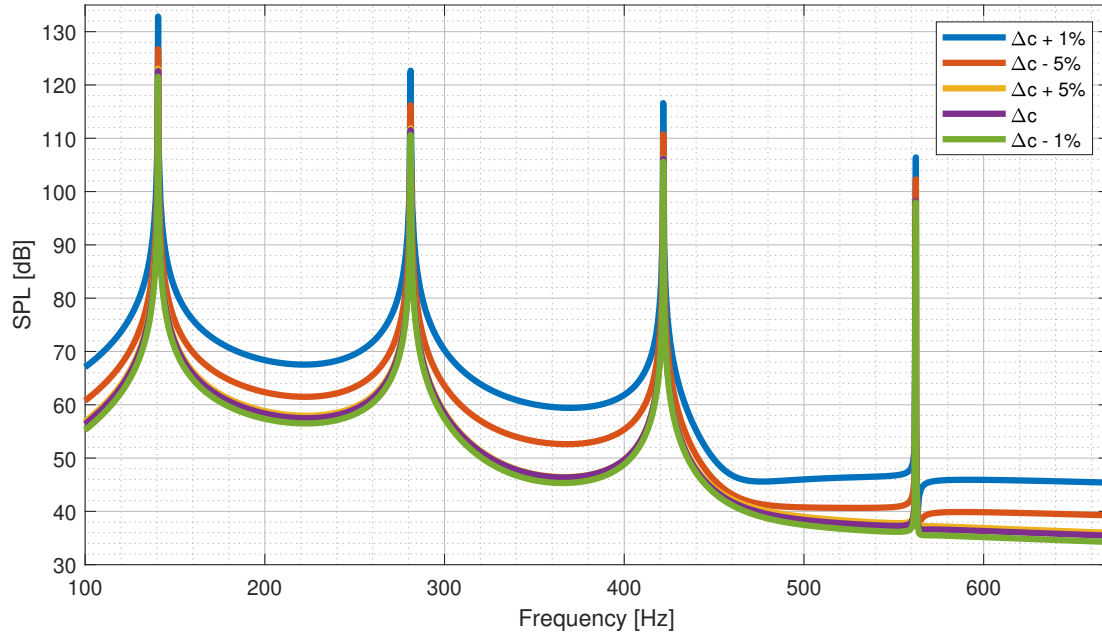


Figure 3.6: Frequency spectra of different Δc values

The absolute SPL values for the peaks of the harmonics are given in Table 3.7 from which can be seen that the -5% change in Δc gives a not converged solution. The result that this case gives is doubtful and will not be taken into consideration when drawing a conclusion of this sensitivity analysis. Increasing the Δc with 5% could be increasing the drag forces in a way that it results in lower performance coefficients and thus lower SPL values than the $+1\%$ case. However, more drag will result in the addition of unsteady loading noise and thus an addition to the noise level. There is a possibility that these two phenomena are cancelling each other out, resulting in a higher difference in SPL value for the $+1\%$ case than for the $+5\%$ case.

Table 3.7: SPL values of the four harmonics for different Δc with $M_x = 0.35$ and $J = 1.4$ and $\beta_{0.75} = 35^\circ$

Change in Δc [%]	1st harmonic Δ SPL	2nd harmonic Δ SPL	3rd harmonic Δ SPL	4th harmonic Δ SPL	stalled sections
-5 (NC)	4.129	4.682	4.532	4.0259	13,16 17,18
-1 (C)	-1.057	-0.922	-0.613	-0.296	-
0 (C)	122.593	111.519	106.198	98.2581	-
+1 (C)	10.236	11.151	10.395	8.1539	13,14,15 16,17
+5 (C)	0.461	0.363	0.120	-0.2509	-

3.3.4. Radial thickness over chord distribution

A change in the thickness distribution does not change the values of the thrust and power coefficient as the thickness distribution is imported after the calculation of the performance coefficients and only has effect on the thickness noise. The SPL values are shown in Figure 3.7. As expected, the lines are overlapping and do not differ much. A higher $\Delta\delta$ value results in a higher SPL value, as the contribution of the thickness noise is increased and the total SPL value is increased as well.

The absolute SPL values are given in Table 3.8 and shows a maximum difference of only 0.2601 dB for the fourth harmonic between the extreme cases.

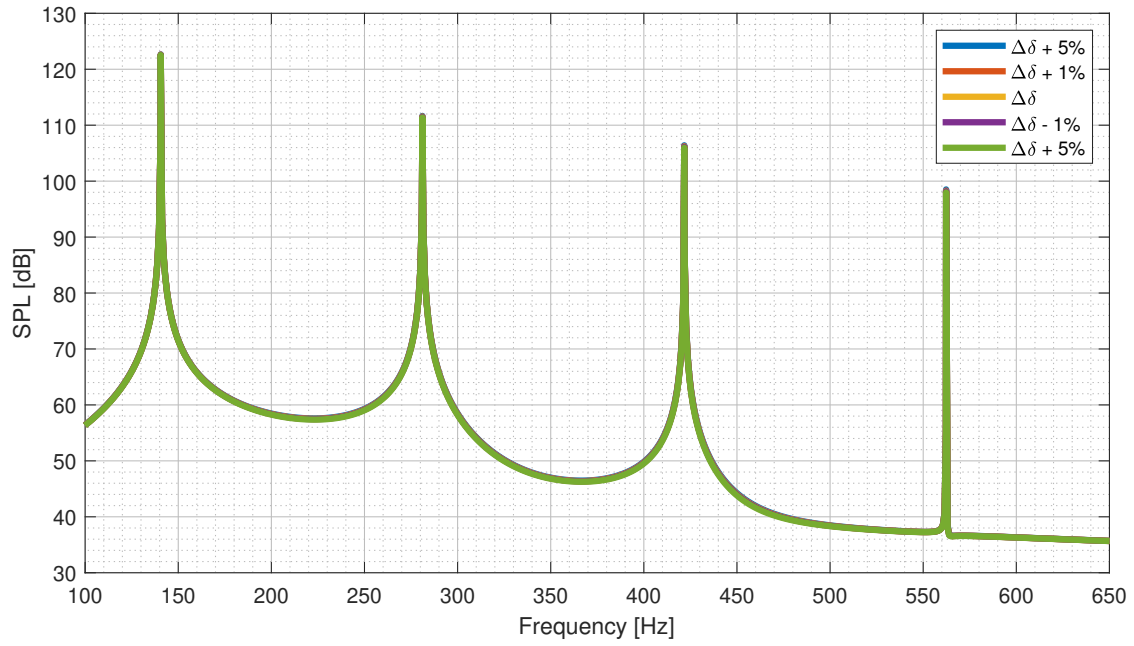


Figure 3.7: Frequency spectra of different $\Delta\delta$ values

Table 3.8: SPL values of the four harmonics for different $\Delta\delta$ with $M_x = 0.35$, $J=1.4$ and $\beta_{0.75} = 35^\circ$

Change in $\Delta\delta$ [%]	1st harmonic Δ SPL	2nd harmonic Δ SPL	3rd harmonic Δ SPL	4th harmonic Δ SPL	stalled sections
-5 (C)	-0.063	-0.142	-0.213	-0.2667	-
-1 (C)	-0.013	-0.029	-0.043	-0.0528	-
0 (C)	122.593	111.519	106.198	98.2581	-
+1 (C)	0.012	0.028	0.042	0.0526	-
+5 (C)	0.064	0.143	0.209	0.2601	-

3.4. Robustness of the HeliX-tool

From the sensitivity analysis, it can be concluded that higher performance coefficients, result in higher SPL values.

Deviating 1° from $\beta_{0.75}$ does not result in very different SPL values. The maximum difference in SPL value is 1.7460 dB for the BPF and the minimum is 0.6622 dB for the fourth harmonic. When deviating 5° from $\beta_{0.75}$, the difference in SPL is significant. The maximum and minimum difference being 10.0720 dB and 3.7229 dB for the BPF and fourth harmonic respectively.

Having a difference in flight speed will result in a different BPF and higher harmonics, as well as different SPL values. Higher values of V_x result in higher performance coefficients and SPL values.

A change in Δc of +1% or +5% results in diverse performance coefficients and SPL values. This is due to the rise of the drag and friction forces, when increasing the chord length.

Changing the $\Delta\delta$ value has almost no influence on the performance coefficients and SPL values. This is due to the fact that the $\Delta\delta$ is introduced after the calculation of the coefficient and only effects the thickness noise. The thickness noise has a small contribution compared to the loading noise for operational conditions below $M_x = 0.7$ [6]. This is also shown in Figure 2.10b.

The input parameters ranging from having the most influence on the output to the least influence is as follows and this is also the order in which the chance of obtaining a wrong value is highest to lowest:

V_x , β_0 , Δc and $\Delta\delta$.

The V_x should be obtained with a high accuracy in order to have a reliable output from the HeliX-tool.

4

Measurements set-up

After the sensitivity analysis is performed and the parameters needed to be obtained with the highest accuracy are known, it is time for the full-scale outdoor experiment. This chapter describes the experiment conducted to obtain the data for the validation of the HeliX-tool. The experiment consisted of four measurements which were performed on the 20th of July, 2021 from 18:42 until 19:08 hours. The chapter starts with the description of the aircraft that is flown in [Section 4.1](#). The microphone array is explained in [Section 4.2](#) and the experiment location and weather conditions are given in [Section 4.3](#) and [Section 4.4](#). The chapter ends with [Section 4.5](#), in which the additional tools and devices used during the four measurements are specified.

4.1. Aircraft

The aircraft that is measured during the noise measurements is the Pipistrel Velis Electro [\[28\]](#), which is shown in [Figure 4.1](#). The Pipistrel Velis Electro is owned by E-flight academy [\[29\]](#), the first and only full-electric flight school in the Netherlands. The Velis is the first certified fully electric-powered two-seater aircraft mainly used for pilot training [\[28\]](#). This aircraft is chosen for the noise measurements because the HeliX-tool models only propeller noise. It is assumed that this aircraft gives only propeller noise as the engine is electric.

The Pipistrel E-811-268 MVIC EASA Type-Certified is the engine of the Velis and has a maximum take-off power, MTOP, of 57.6 kW [\[28\]](#).



Figure 4.1: Pipistrel Velis Electro

Propeller

The Pipistrel has the P-812-164-F3A Certified fixed-pitch composite three-blade as propeller which has a diameter of 1.64 m and can be seen in [Figure 4.2](#). The blade angle at 75% of the blade radius, $\beta_{0.75}$, is measured by Hangar One, an aircraft maintenance company located at Teuge Airport, and found to be 18°. [Chapter 5](#) will go into more detail about the obtaining of the propeller geometry data.



Figure 4.2: Close up of the P-812-164-F3A Certified fixed-pitch composite three-blade

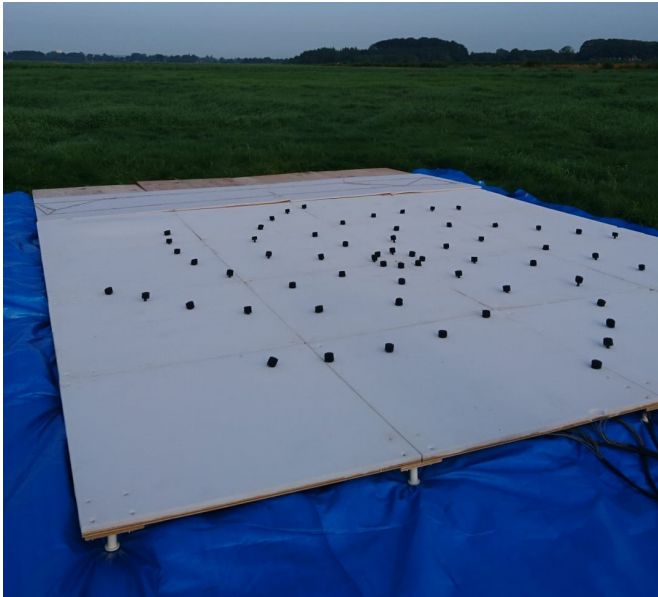
4.2. Microphone array

The microphone array that is used for the outdoor noise measurements is designed by an aerospace engineering alumna of the Delft University of Technology. The array has 64 microphones which are connected through 8 spiral arms. The microphones are placed in an Underbrink configuration which is shown in [Figure 4.3b](#). An advantage of this configuration is the ability to analyze both far-field and near-field with a high resolution [\[30, 31\]](#). This configuration creates a higher density of microphones in the middle of the array and has a high performance over a broad range of frequencies in terms of array resolution and side lobe levels. However, this resolution is limited by the Rayleigh limit or distance, which is also known as the spatial resolution [\[32\]](#) and is the limit at which the two sources are still separately visible. The Rayleigh limit is given by [Equation 4.1](#) [\[33\]](#).

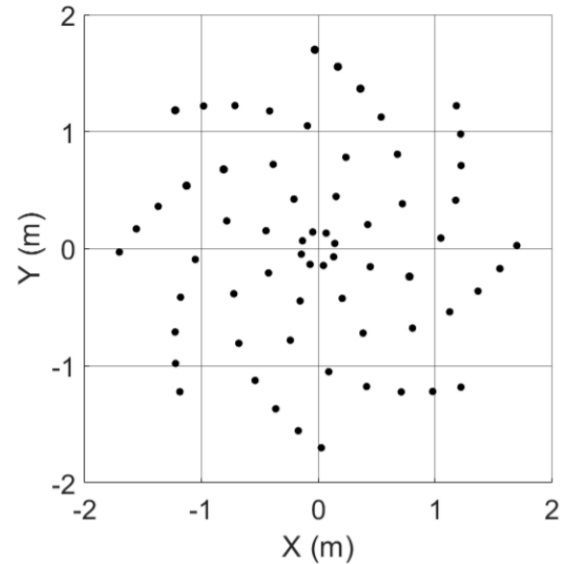
$$R_d = 1.22 \frac{ch}{D_{array}f} \quad (4.1)$$

Here R_d equals the Rayleigh distance, c the speed of sound in air, h the distance between source and receiver, D_{array} the array aperture, and f the frequency. When the distance between the source and receiver increases, the Rayleigh distance increases, and thus the spatial resolution decreases [\[32\]](#).

The microphones are mounted on 16 1 by 1-meter wooden plates, which together make an array of 4 by 4-meter. To prevent any reflections by these wooden plates, the plates are covered with a layer of melamine foam to absorb the sound. The microphones closest to the edges of the array are located 30 cm inward from the edges to reduce the ground reflection. This results in an array aperture of 3.4 m. Windshields are placed on top of the microphones to diminish the effect of wind. The microphones are calibrated with a pistonphone of 1 kHz at an OSPL of 93.8 dB. The microphone array located in the field at Teuge airport is shown in [Figure 4.3a](#).



(a) The 4 by 4-meter microphone array located in the field at Teuge airport



(b) The Underbrink microphone array configuration as used in the outdoor measurements. This view is from below, looking upward towards the sky

Figure 4.3: The microphone array used for the noise measurements at Teuge Airport

Besides the microphone array, a system is needed that records the analog signals and converts these to a digital signal. This is the data acquisition system, DAQ, which has a sampling rate of 50 kHz. Four DAQs are available for outdoor measurements and for this experiment, the DAQ camera 2 was used for all measurements. A laptop is connected to the DAQ which has the application Labview installed to control the DAQ. With the Labview application, the measurements can be stopped and started, data can be saved and real-time microphone data, spectrogram, and beamforming can be shown. These features allow the user to check the microphone outputs during the measurements [32].

An optical camera is placed in the center of the microphone array facing upwards to the sky. It is also connected directly to the laptop and Labview. In Labview, the exposure time can be altered, which allows for a clear video in every weather condition. The optical camera supports the acoustic measurements in two ways. The first is being able to determine the overhead location of the aircraft by generating a video. The second is being able to lay a still of the video over the acoustic source map in order to check if the location of noise sources is correct. This can be checked when the noise data has been obtained and beamforming is performed. The method of beamforming will be explained in Subsection 7.2.2.

During the measurements at Teuge Airport, the researchers were not allowed to stand at the location of the microphone array for safety reasons and therefore could not make use of the real-time features of Labview. The optical camera was not working due to an update issue and therefore no video was recorded during the measurements.

4.3. Experiment location

The outdoor measurements were taken at Teuge Airport. A data set of four noise measurements of the Pipistrel Velis Electro were gathered. The four measurements consisted of three take-offs and one fly-over. These measurements were agreed upon by E-flight academy and the researchers. The take-offs were of importance for E-flight and the fly-over for the validation of the HeliX-tool. Due to the electric engine and thus battery capacity, these four measurements could be performed before the battery capacity was too low. To obtain the most accurate measurements, the Velis should be as close as possible to the microphone array, and background noise should be minimal.

From these requirements, the microphone array location was determined to be in the extension of the runway with a small road nearby. This location would result in the highest chance to have the aircraft fly straight over the array. The location of the array and the researchers during the measurements is shown in Figure 4.4 in which the direction of flight is also indicated.

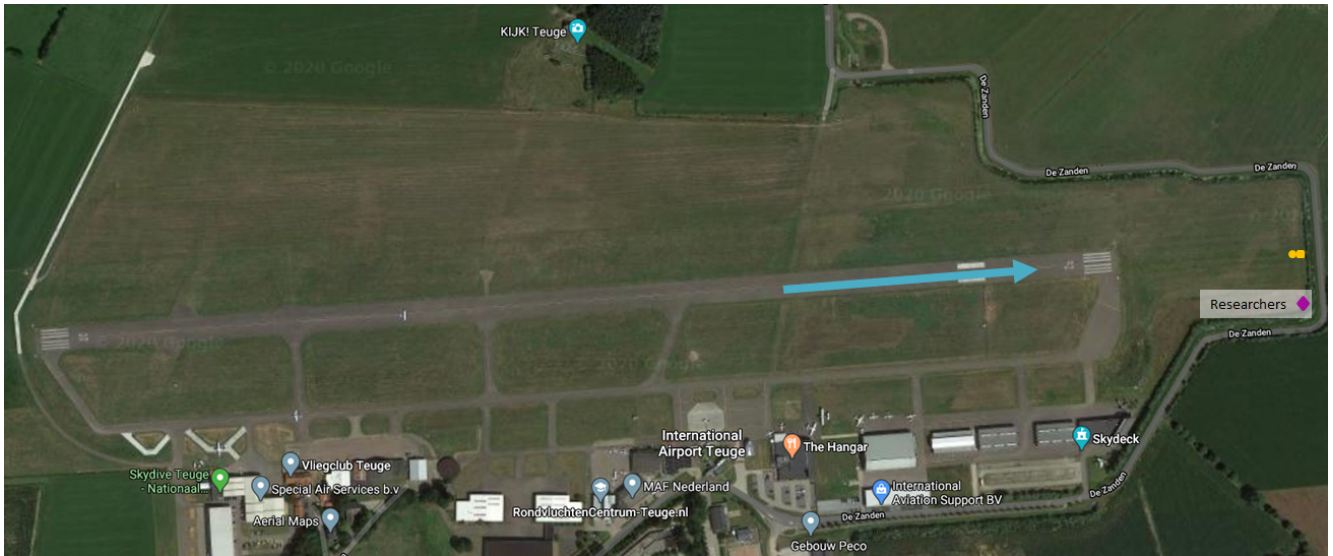


Figure 4.4: Location of the microphone array (yellow blocks) at Teuge Airport, direction of flight is indicated with the blue arrow and the researchers location is indicated with the purple diamond.

4.4. Weather conditions

The weather conditions are necessary for the validation of the HeliX-tool as these can alter the noise levels by changing the propagation of the sound. For example, if there is a strong wind present during the measurements, this will affect the noise levels recorded. They are obtained through the Royal Dutch Meteorological Institute, KNMI, and are summarized in Table 4.1. Teuge Airport does not have a KNMI station therefore the weather conditions from the closest airport Deelen are used which is located at 5.873 LON and 52.056 LAT.

Table 4.1: Weather conditions at Teuge Airport

Parameter	Meaning	Value	Unit
T	Temperature	19.5	$^{\circ}C$
P	Pressure	1021.7	hPa
RH	Relative humidity	67	%
DD	Wind direction	East	-
V_{wind}	Wind speed	1	m/s

4.5. Additional tools

Two other tools are used during the noise measurements. These are a GoPro and Garmin GLO global positioning system (GPS) sensor. The GoPro is used in the cockpit to film the cockpit instruments from which the flight speed, V_x , rotational speed, RPM, and altitude, h can be seen.

The Garmin GLO GPS sensor was connected to a smartphone via bluetooth. With a GPS app called myTracks, data was stored in a .gpx and .kml file. With an online KML-to-CSV converter [34], the data are read in an excel file from which the GPS coordinates of the flight path are found. From the GPS data, the velocity is calculated with Matlab. This is explained in more detail in Section 6.1. The flight path flown during the measurements and processed in Matlab can be seen in Figure 4.5 where the location of the microphone array is indicated by the red marker. The flight path obtained by the Garmin GLO GPS sensor is also processed by the online KML-to-CSV converter and the two flight paths are the same.

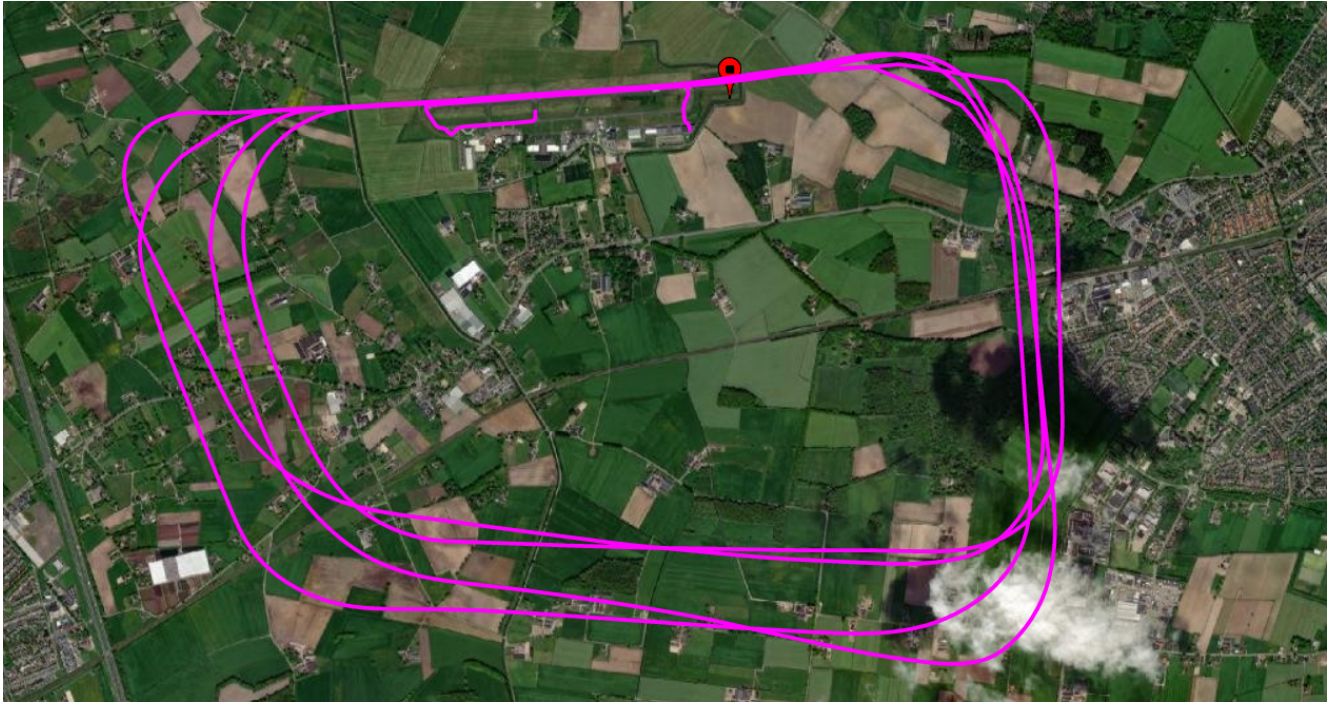


Figure 4.5: Flight route captured by the Garmin GPS sensor and processed in Matlab

5

Propeller geometry

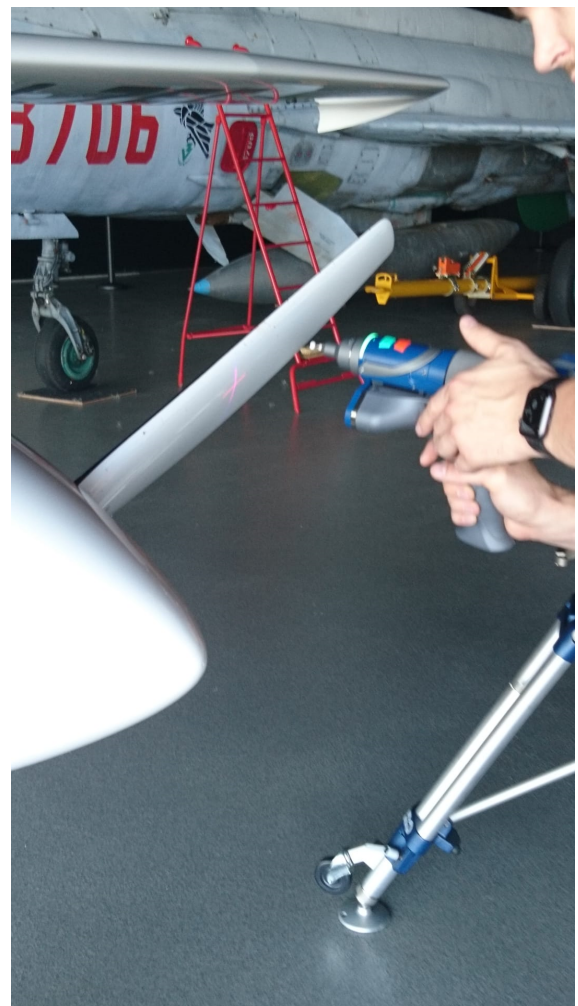
The geometry of the propeller has been mentioned in [Chapter 3](#) and is an important input for the HeliX-tool. It is defined by four data sets which are the radial chord over diameter distribution, Δc , the radial thickness over chord distribution, $\Delta \delta$, the radial blade pitch angle distribution, $\Delta \beta$, and the airfoil coordinates per radial blade section. These are obtained by 3D scanning one propeller blade because there was no data available from the manufacturer. The 3D scanner and arm are shown in [Section 5.1](#). [Section 5.2](#) discusses the geometry processing of the propeller blade. When no 3D scanner is available, a different method of obtaining the propeller geometry is explained in [Appendix B](#).

5.1. 3D scanner and arm

The FaroBlu HD laser with a FARO Quantum E 3.5m 7-axis arm is the 3D scanner that is used [35]. The scanner with arm is shown in [Figure 5.1](#). It has an accuracy of $\pm 25 \mu m$, gives 2000 points per line, has a scan rate of 300 frames per second which results in scanning 600000 points per second. It is preferred to have a smooth but not reflecting surface. There is no specific pattern or training that needs to be followed in order to capture the object, as long as the laser covers the entire surface.



(a) The FaroBlu HD laser with a FARO Quantum E 3.5m 7-axis arm

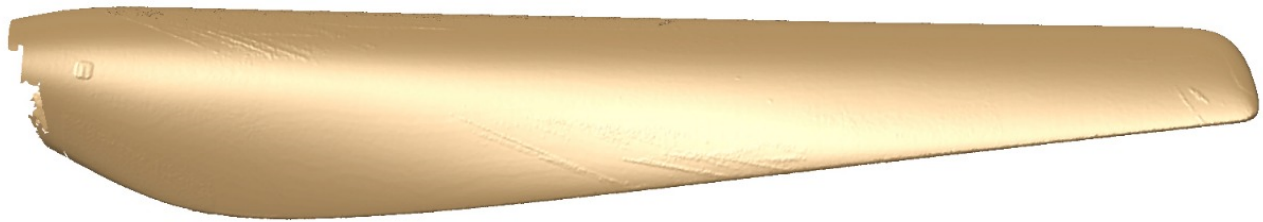


(b) Scanning the propeller blade

Figure 5.1: Pictures taken during the 3D scanning of the propeller blade of the Pipistrel Velis Electro

5.2. Geometry processing

Several steps are taken before the geometry files are obtained. The 3D scanned geometry consists of points covering the surface area of the propeller blade. The minimum point spacing is $40\mu m$. The scanned geometry is optimized in the software of the 3D scanner. This optimization consists of manually removing the points outside of the surface of the blade and checking whether the surface of the blade has been captured by the 3D scanner. Through the points displaying the surface of the blade, a mesh is generated and exported as a .stl file. From this 3D model of the propeller blade the chord, thickness, blade pitch, and airfoil coordinates need to be determined. This is done by importing the file into CATIA, a CAD software program. The top, bottom, and side views of the 3D scanned propeller blade are shown in [Figure 5.2](#).



(a) Top view



(b) Bottom view



(c) Side view

Figure 5.2: 3D scanned propeller blade of the Pipistrel Velis Electro in CATIA

There is missing surface at the root of the propeller blade, this is because the hub of the propeller is located at the root. The top view is the side faced away from the pilots and the color was white. This side of the propeller had a little sticker near the root which can be seen in [Figure 5.2a](#).

The bottom view, [Figure 5.2b](#), which is the side of the propeller facing the pilots was black and the 3D scanner had a little more trouble scanning this side. The 3D scan of this side shows more roughness than the top view, however, this roughness is because the scanner had to go over this side more frequently which resulted in more points. This is not preferred as too many points creates a thick layer of points which is computational expensive and can result in a thicker geometry.

When the .stl file is imported in CATIA, the model is cut into sections. The numbers of sections and spacing for the several geometry files is given in [Table 5.1](#). The number of sections is the same as for the SR2 propeller that Haddaoui [5] used to design the HeliX-tool. The first section for the thickness, chord, and blade pitch angle distribution is at 162.437 mm and for the airfoil coordinates sections at 175 mm measured from the root.

Table 5.1: Geometry data file sections

Geometry symbol	Meaning	Number of sections [-]	Spacing [mm]
Δc	Radial chord over diameter distribution	51	13
$\Delta \delta$	Radial thickness over chord distribution	43	15.4
$\Delta \beta$	Radial blade pitch angle distribution	42	16
-	Airfoil coordinates	18	38.3

The propeller blade with its sections for the airfoil coordinates is shown in [Figure 5.3](#). To cut the propeller blade in sections, a line representing the leading edge is created from which the sections are generated.

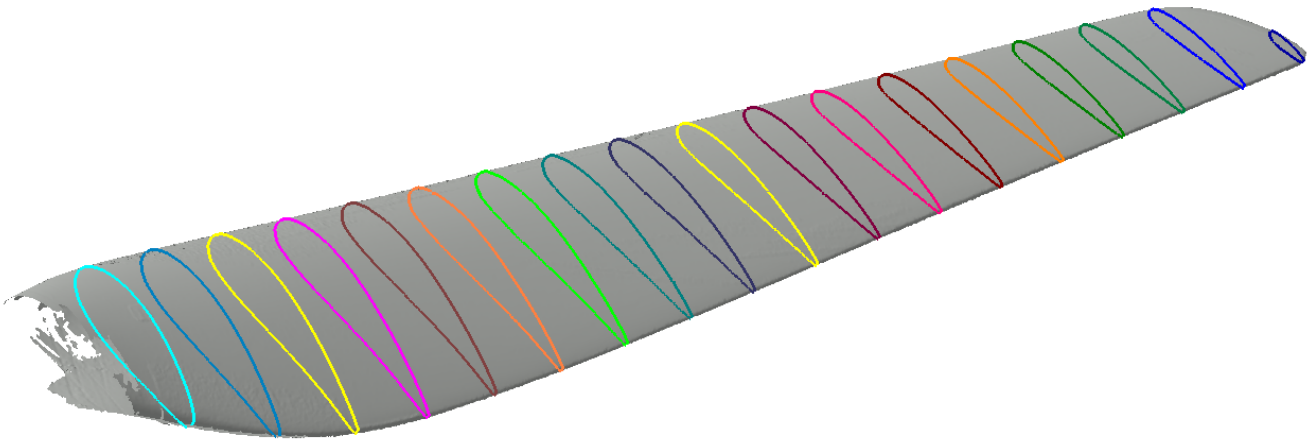


Figure 5.3: The 3D scanned propeller blade with the 18 airfoil coordinates sections

The chord, thickness, and blade pitch angle distribution are measured in CATIA with the measuring tool. The chord and thickness are found as given in [Figure 5.6](#). The blade pitch angles are found as follows:

- The section at 75% of the blade radius is created.
- There the axis system is generated as shown in [Figure 5.4](#) to have the β at a value of 18° . This figure is also used by Hangar One to determine the β at 75% of the blade radius.
- This axis system is used to determine the β at the other sections by using the measuring tool.

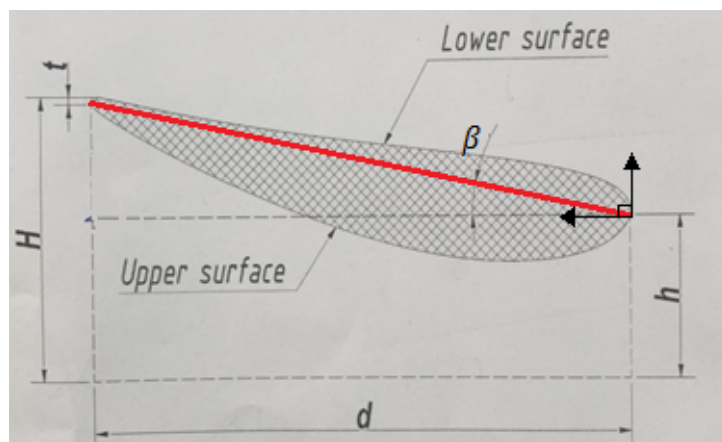


Figure 5.4: Definition of β

The chord is divided over the diameter to get Δc , the thickness is divided over the chord corresponding to the section of the thickness to get $\Delta \delta$ and the measured blade pitch is subtracted from the $\beta_{0.75}$ to obtain the $\Delta \beta$. The obtained Δc , $\Delta \delta$ and $\Delta \beta$ are plotted as a function of the radial position to radius ratio, r/R , and are shown in Figure 5.5.

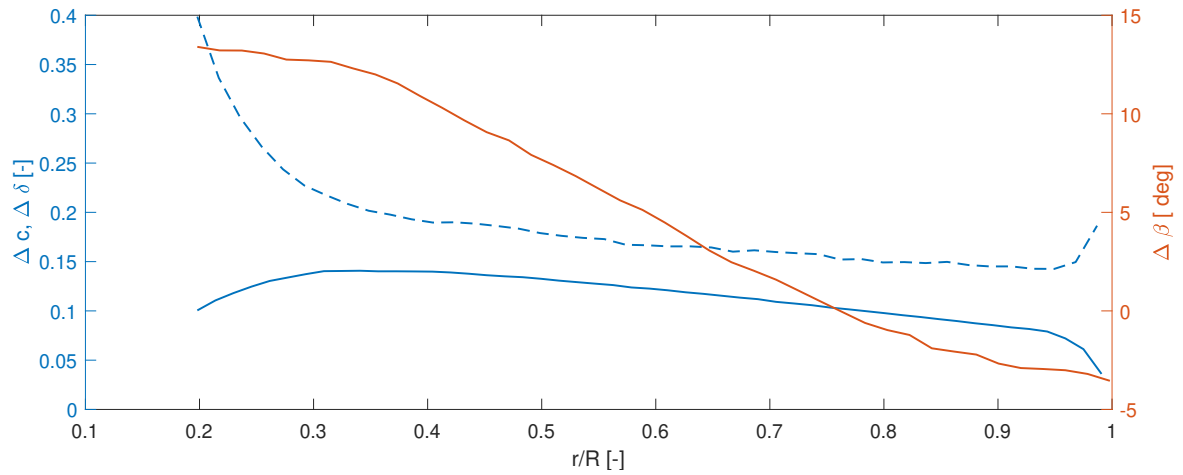


Figure 5.5: Pipistrel propeller design parameters. The Δc , $\Delta \delta$ and $\Delta \beta$ are plotted as a function of r/R

The airfoil coordinates cannot be computed in CATIA. Sketches of all 18 sections are made with the corresponding coordinate system. The sketch of the first section is shown in Figure 5.6.

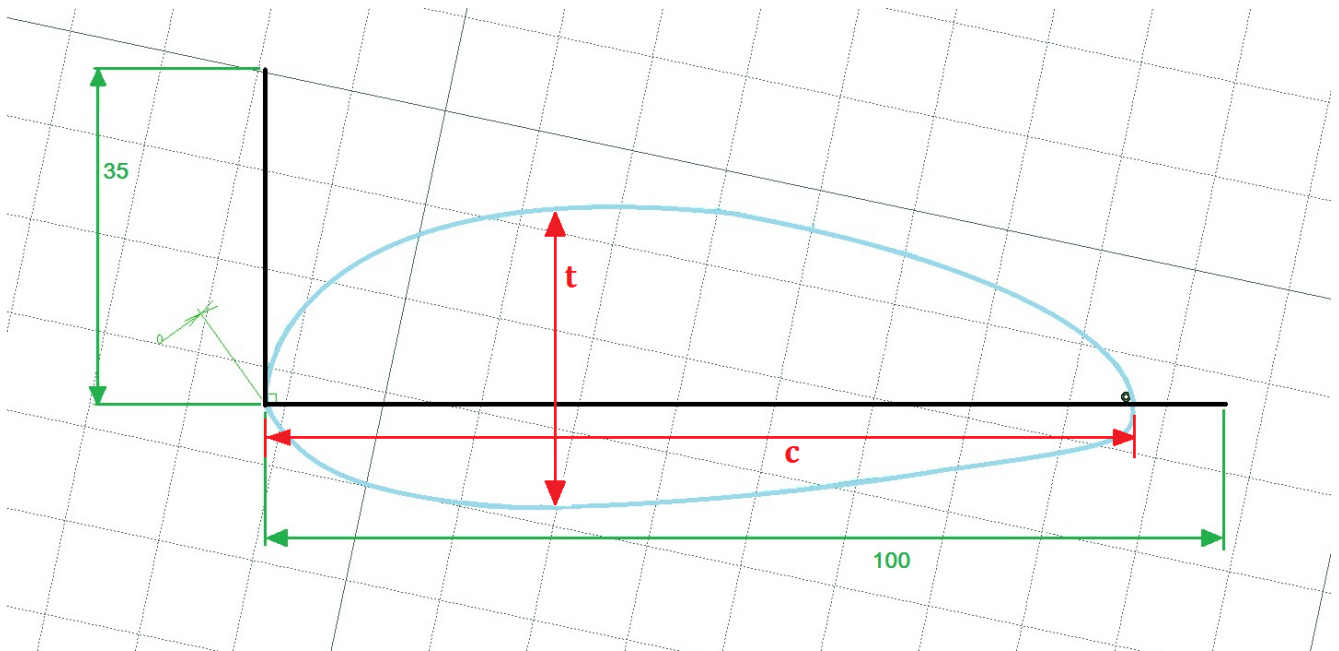


Figure 5.6: Sketch of section 1 generated in CATIA

These sketches are exported as .jpg files and imported into the GetDataGraph digitizer software. This software enables the finding of the coordinates of the airfoil profile. The axis needs to be determined first for scaling after which you can click on the airfoil profile and obtain the coordinates. The number of airfoil coordinates are between 40 and 60. Later, in XFOIL, this number is increased to 160 for every section by interpolating between the points. The airfoil coordinates are exported as a .txt file. XFOIL wants to have the airfoil coordinates from the trailing edge to the leading edge and back to the trailing edge. After the coordinates are found a normalization of the coordinates is performed.

6

Data Analysis of Measurements

After the full-scale outdoor noise experiment has been performed, the obtained data needs to be analyzed and processed. This chapter describes the data analysis of the full-scale outdoor noise measurements taken with the Pipistrel Velis Electro. It starts with the description of the data obtained by the GoPro and GPS sensor in [Section 6.1](#) which is followed by the data processing of the calibrated noise data in [Section 6.2](#). The main lobe width is explained in [Section 6.3](#) and the chapter ends with the beamforming of the fly-over measurement in [Subsection 7.2.2](#).

6.1. Data from GoPro and GPS sensor

The GoPro videos show the rotational speed, RPM, velocity, V_x , in kts and altitude, h , in ft during the measurements. The video is stopped when the aircraft is overhead the microphone array by looking at the maps display in the cockpit and the values of the variables are read from the instrumental displays.



Figure 6.1: Cockpit image from the GoPro video

In [Figure 6.1](#), the yellow block indicates the altimeter from which the altitude is estimated. 50 ft is subtracted from the estimated value as this is the offset seen when the aircraft is on the ground. The red block indicates the rotational speed display, and the blue block represents the map display. The yellow dot in the maps display shows the location of the microphone array during the measurements. The name of the GoPro video, with time stamp and values of the rotational speed, altitude, and velocity are summarized in [Table 6.1](#).

Table 6.1: GoPro data

Measurement	GoPro video name	Time stamp [m:s]	h [m]	ω [RPM]	Velocity [kts]	Velocity [m/s]
Take-off 1	GH010233	09:54	76.20	2430	60 kts	30.8667
Take-off 2	GH020233	02:59	39.62	2460	67 kts	34.4678
Take-off 3	GH020233	07:24	42.76	2440	65 kts	33.4389
Fly-over	GH020233	11:47	12.19	2520	80 kts	41.1556

Four noise measurements are performed in total thus the location of the microphone array should be four times present in the GPS data file. The location of the microphone array is determined by using Google maps and is found to be 6.061948 LON and 52.243294 LAT. The GPS data is matched with these coordinates and the velocity has been calculated by using Haversine's formula [36]. The Haversine formula gives the shortest distance between two GPS coordinates over the Earth's surface ignoring elevation. The GPS data is determined every second which results in a distance every second. The velocity is calculated by dividing the distance over 1 second. The velocities at corresponding number of GPS stamp are given in Table 6.2.

Table 6.2: GPS coordinates with corresponding velocity

Number of GPS stamp [-]	GPS LON coordinate [-]	GPS LAT coordinate [-]	Velocity [m/s]
199	6.0621	52.2436	31.0443
464	6.0620	52.2435	36.8442
703	6.0621	52.2436	36.1095
939	6.0619	52.2434	41.7091

From the velocity and rotational speed, the BPF and J can be calculated with Equation 2.1 and Equation 2.17. The BPF and the J are summarized in Table 6.3, where the velocity, V_x , from the GPS is used for the calculation as this is more accurate than the velocity obtained from the cockpit because the cockpit instrument shows the velocity in steps of 1 kts, which is 0.514 m/s. The BPF can also be obtained from the frequency spectra plot, which is generated in the following section.

Table 6.3: BPF and J

Measurement	BPF [Hz]	J [-]
Take-off 1	121.5	0.4674
Take-off 2	123.0	0.5480
Take-off 3	122.0	0.5414
Fly-over	126.0	0.6055

6.2. Calibrated noise data

During the experiment on Teuge Airport, four measurements were completed. These consist of three take-offs and one fly-over. The data from these measurements were calibrated and processed into several graphs. Information about the calibration can be found in von den Hoff [32]. The first graph that is generated from the data is the spectrogram which is found in Subsection 6.2.1. The spectrogram of the measurements is given to show the reader the harmonics and the absence of background noise. This is an indication that the noise data will probably only exist of propeller noise. The OSPL and OASPL plots are found in Subsection 6.2.2. From these plots, the time stamp of the peak in noise level can be seen which is needed for the generation of the frequency spectra which are plotted and shown in Subsection 6.2.3.

6.2.1. Spectrogram

A spectrogram is a two dimensional image of the spectrum of a sound signal and shows how it varies with time. The vertical axis represents frequency, the horizontal axis represents time and the colors indicate the power often given in dB [37].

The spectrogram is generated by breaking up the in time domain sampled signal into data chunks. These are Fourier transformed and for each chunk, the spectrum level in dB is calculated. Every chunk corresponds to a vertical line in the spectrogram and they are laid side by side to form the image [37].

The most important feature of the spectrogram is the length of the data chunks, T , which is also called window size and is calculated by Equation 6.1. Here, N is the number of samples in each chunk and Δt is determined using $1/f_s$, where f_s equals the sampling frequency which is 50 kHz for every measurement [37].

$$T = N\Delta t \quad (6.1)$$

The frequency resolution can be calculated using Equation 6.2, meaning a shorter window will give more accurate results in timing, but that will be at the expense of the frequency resolution, and vice versa [37].

$$df = \frac{1}{T} \quad (6.2)$$

A window can be applied over the signal to reduce the side lobes in the frequency spectrum. These side lobes are a result of constructive interference. When the magnitude of these side lobes are equal to the main lobe, these are called grating lobes [38].

For the noise data of this experiment, a Hanning window with length N is applied over the time signal. The Hanning window is visually presented in Figure 6.2 [39]. The window reduces the side lobes and increases the main lobe width. More information about the main lobe width is presented in Section 6.3. After applying the fast Fourier transform over the signal, the signal is corrected for the Hanning window again.

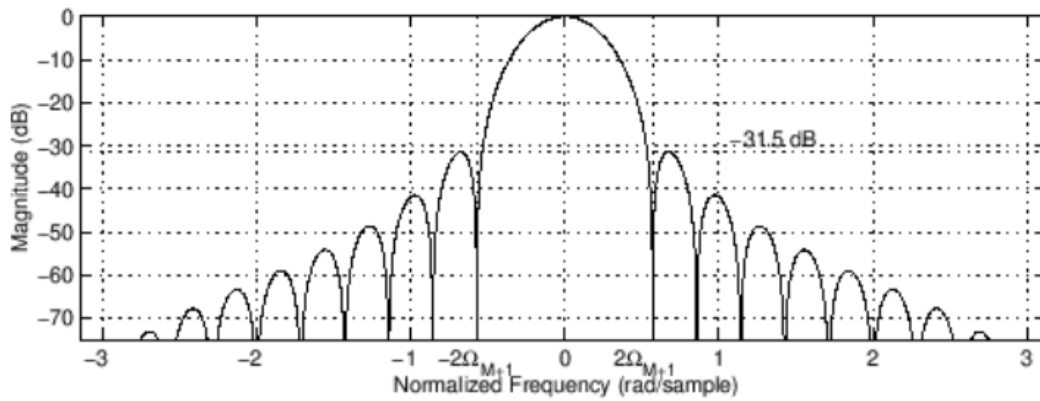


Figure 6.2: The Hanning window and its discrete time Fourier transform [39]

The four spectrograms of the measurements are given in Figure 6.3. The frequency resolution can be improved without altering the time resolution. This results in a clearer spectrogram and is done by zero-padding the signal. Zeros are added to the data chunks to increase the length of the signal without adding information to it. The fast Fourier transform will be computed faster when using a length of 2^X . Therefore, the data chunks for all the four measurements are zero-padded to a length, N, of $2^{14} = 16384$. The resulting window size and frequency resolution is given in Table 6.4. The block size is the initial number of samples in a data chunk, and this is thus prolonged to the size of N. The theoretical df is determined by the blocksize, while the df is determined by N.

Table 6.4: Parameters needed for the generation of the spectrograms

Measurement	Block size [-]	N [-]	T [s]	df [Hz]	df theoretical [Hz]
Take-off 1	3111	16384	0.3277	3.0518	16.072
Take-off 2	4150	16384	0.3277	3.0518	12.048
Take-off 3	3125	16384	0.3277	3.0518	16.000
Fly-over	3838	16384	0.3277	3.0518	13.028

The sound measurements are clean as the different harmonics are accurately shown and the spectrogram also shows the Doppler effect, as expected. This effect is shown in the shape of the harmonics. They are in a 'Z' shape, they start at a higher frequency and later drop to a lower frequency which is sensible as the aircraft is flying first towards the microphone array and then away from it. This is because when the noise source moves to the observer, the distance between the radiated sound waves decreases, and thus the distance between two peaks becomes smaller resulting in a higher frequency. The distance between two peaks increases when the noise source is moving away from the observer resulting in a lower frequency.

The spectrograms of the second and third take-off are similar in shape to each other. The fly-over has a small spreading of the SPL values in the time domain, which is probably due to the higher flight speed.

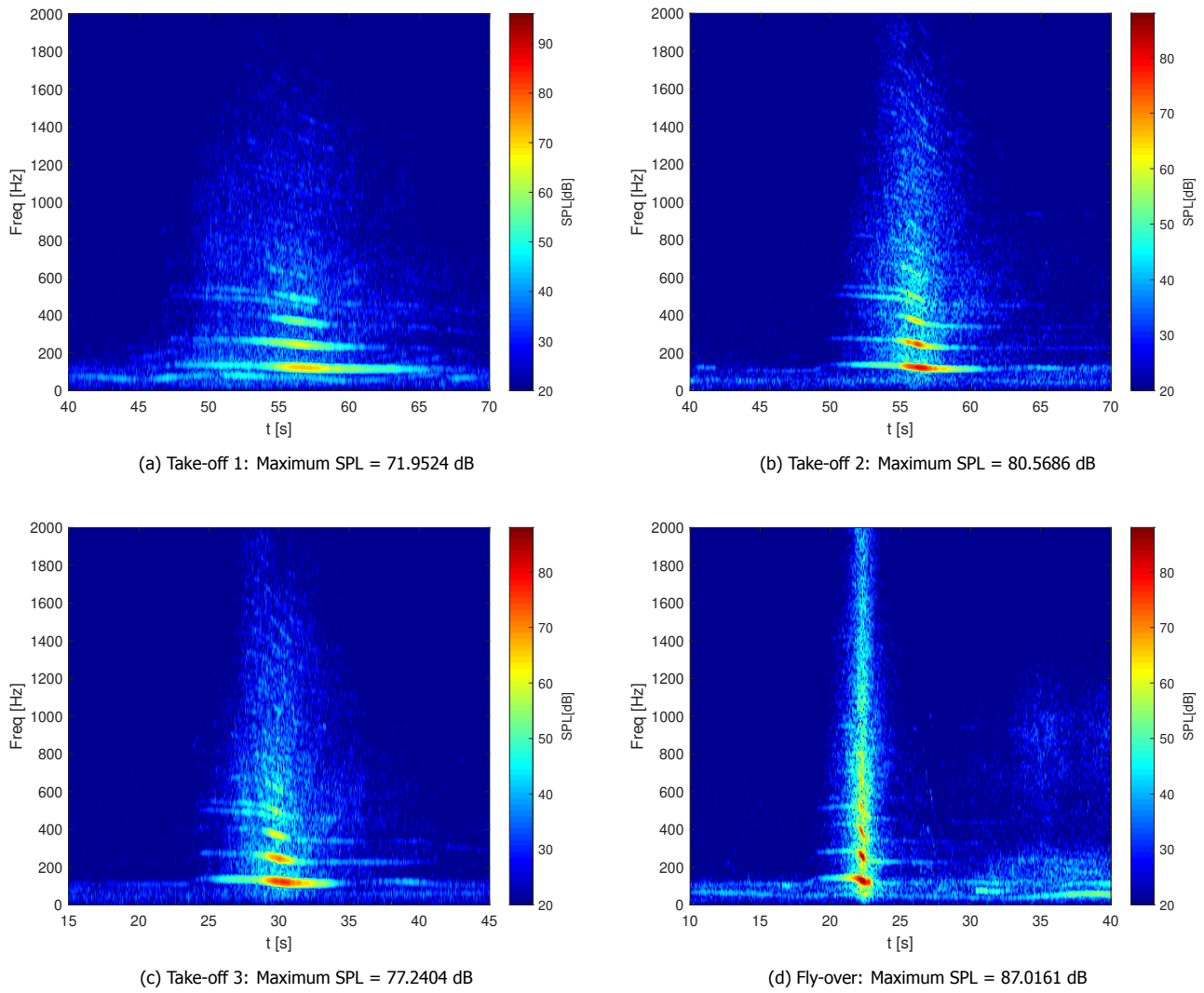


Figure 6.3: Spectrograms of the four measurements with a 30 seconds time window. Maximum SPL level for the dB scale is determined from [Figure 6.3d](#)

6.2.2. OSPL & OASPL

The second graph that is generated is the OSPL and OASPL plots which are shown in [Figure 6.5](#). The OSPL is the overall sound pressure level and the OASPL is the overall A-weighted sound pressure level. These parameters measure the loudness of a noise signal via phones [\[37\]](#).

The OSPL is calculated by [Equation 6.3](#) in the time domain and by [Equation 6.4](#) in the frequency domain [\[37\]](#). These two OSPLs should be the same to verify whether the data processing is correct in the frequency domain.

$$OSPL = 10 \log_{10} \left(\frac{p_e^2}{p_{e0}^2} \right) \quad (6.3)$$

$$OSPL = 10 \log_{10} \sum 10^{SPL/10} \quad (6.4)$$

The p_{e0} is the reference effective pressure which generally has a value of $2 \cdot 10^{-5}$ Pa. The p_e^2 is the effective pressure squared which is given by [Equation 6.5](#) in which $x(t)$ is the time signal. For sinusoidal signals the p_e is given by [Equation 6.6](#).

$$p_e^2 = \frac{1}{T} \int_0^T [x(t)]^2 \quad (6.5)$$

$$p_e = \frac{1}{\sqrt{2}} p_{max} \quad (6.6)$$

The OASPL is also known as the L_A and is calculated by Equation 6.7 [37]. Here, ΔL_A is the A-weighting function which is calculated by Equation 6.8 and is graphically depicted in Figure 6.4.

$$L_A = 10 \log_{10} \sum 10^{\frac{SPL + \Delta L_A}{10}} \quad (6.7)$$

$$\Delta L_A = -145.528 + 98.262(\log f) - 19.509(\log f)^2 + 0.975(\log f)^3 \quad (6.8)$$

This A-weighting is based on the equal loudness contour at 40 phons. Phon is the unit of loudness and is defined as follows: "A tone has a loudness level of X phons if it is equally loud as a tone with an SPL of X dB at 1 kHz" [37].

The A-weighting damps the power level at lower frequencies more than at the higher frequencies as can be seen from Figure 6.4. The first six harmonics of the full-scale outdoor measurements are below 1000 Hz and therefore the OASPL values are lower than the OSPL values which can be seen in Figure 6.5. The maximum OSPL and OASPL values are indicated as well.

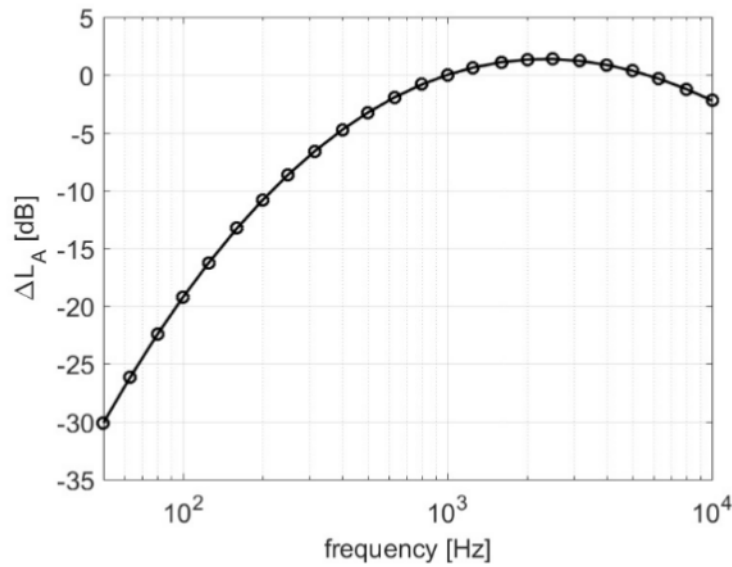
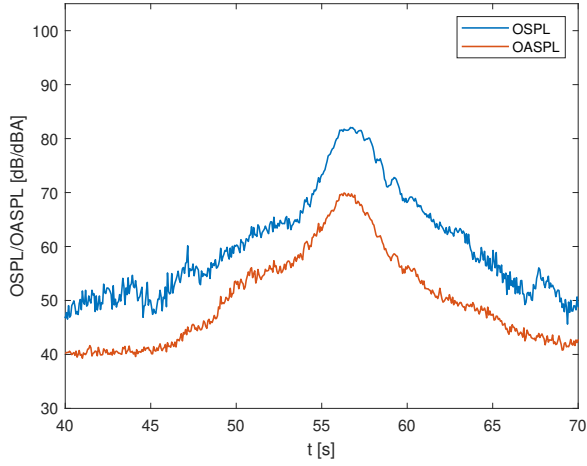
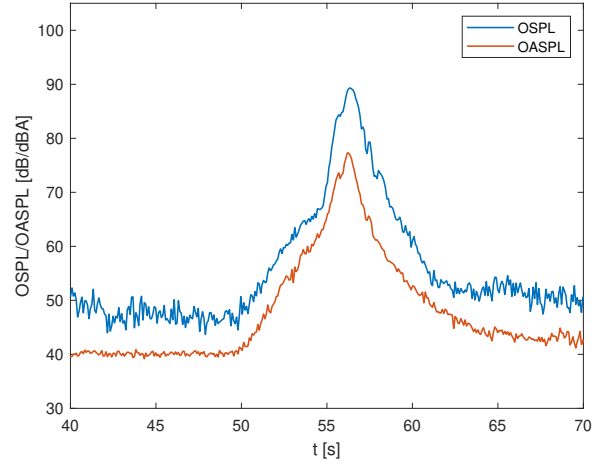


Figure 6.4: A-weighting function as given by Equation 6.8 [37]

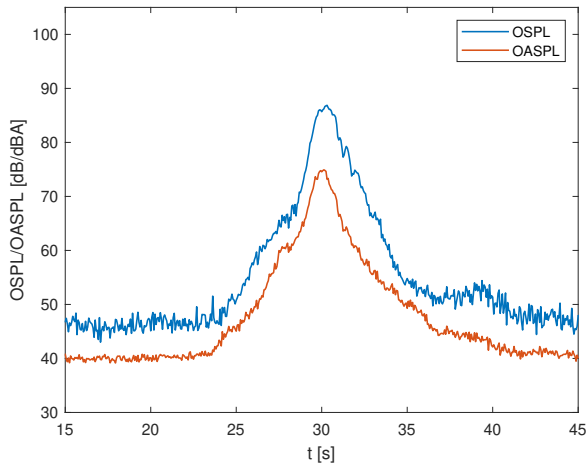
The second and third take-offs are similar in peak shape and the fly-over has the sharpest peak. This is as expected as the spectrogram showed a similar result.



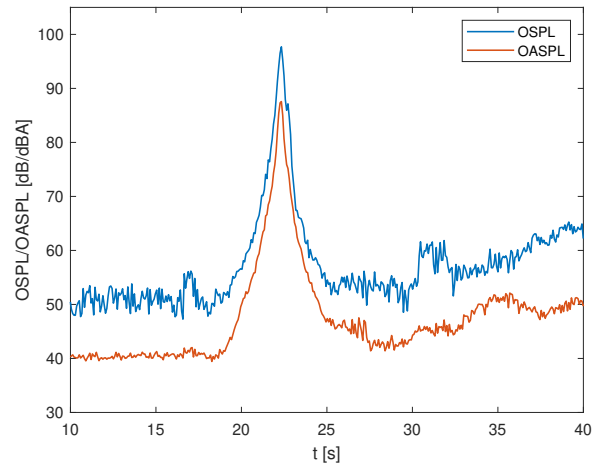
(a) Take-off 1: Maximum OSPL & OASPL = 82.0687 dB & 69.9262 dBA



(b) Take-off 2: Maximum OSPL & OASPL = 89.3403 dB & 77.2936 dBA



(c) Take-off 3: Maximum OSPL & OASPL = 86.87 dB & 74.9338 dBA



(d) Fly-over: Maximum OSPL & OASPL = 97.7014 dB & 87.5632 dBA

Figure 6.5: OSPL and OASPL plots of the four measurements

6.2.3. Frequency spectra

The third graph created is the frequency spectrum, which stems from the generation of the power spectral density, PSD. The PSD represents the amount of energy in a frequency band.

Parseval's theorem gives for a continuous signal the representation given in Equation 6.9 [37].

$$\int_{-\infty}^{\infty} [x(t)]^2 dt = \int_{-\infty}^{\infty} |X(f)|^2 df \quad (6.9)$$

From these two equations, the equation of the PSD, in Pa^2/Hz is expressed as given by Equation 6.10 [37]. In the discrete form, the PSD is given by Equation 6.11.

$$PSD = P(f) = \frac{|X(f)|^2}{T} \quad (6.10)$$

$$PSD = P_m = \frac{|X_m|^2}{T} = \frac{|X_m|^2}{N\Delta t} \quad (6.11)$$

The PSD presents the energy in a 1 Hz band. Multiplying the PSD by df results in the SPL value. Take the \log_{10} of this and the SPL in dB is obtained as shown in Equation 6.12.

$$SPL = 10 \log_{10} \left(\frac{df \cdot PSD}{p_{ref}^2} \right) \quad (6.12)$$

The SPL values of the four measurements are plotted against the frequency which generates the frequency spectra. The frequency spectra need to be generated when the aircraft is overhead the microphone array and in a short time slot. This is to obtain an adequate estimate of the PSD values and thus SPL values. The Doppler effect will be interfering with the data processing when a long time slot is chosen. A snapshot of 0.1 s is selected. During these 0.1 s, the aircraft will move a distance of approximately 4 m which is determined by multiplying the axial velocity with the 0.1 s, which is the size of the microphone array. The four frequency spectra are shown in Figure 6.6. The start time of the snapshot is obtained by looking at the OSPL and OASPL plot Figure 6.5 and is taken 0.1s around the peak of the SPL. The start time is thus 56.76 s, 56.31 s, 30.2 s, and 22.29 s for take-off 1, take-off 2, take-off 3, and fly-over respectively. Meaning the peaks of the SPL of the four measurements are located at 56.81 s, 56.36 s, 30.25 s, and 22.34 s. In order of highest to lowest SPL peaks is the fly-over, take-off 2, take-off 3, and take-off 1. This is logical as this trend was found in the spectrograms and mainly determined by the altitude of the measurement.

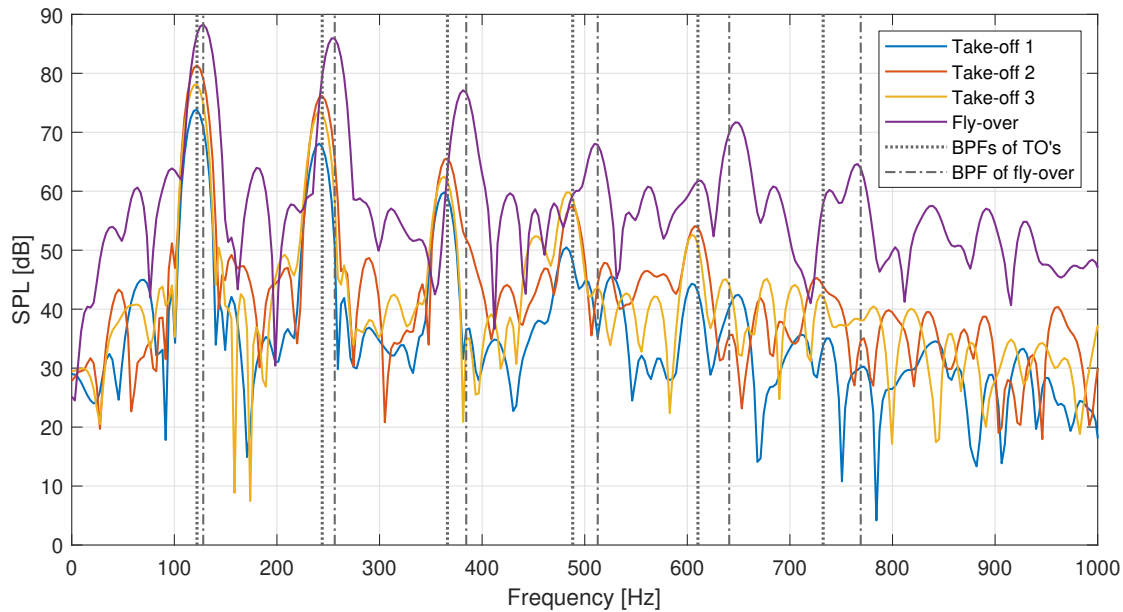


Figure 6.6: Frequency spectra of the four measurements

The BPF is already calculated and given in Table 6.3 but can be obtained from the frequency spectra too as indicated in Figure 6.6. The difference between the calculated BPF and the BPF obtained from the frequency spectra plots is small from which is concluded that the data processing has been properly executed.

The tonal harmonics are present at the BPF and higher multiples of the BPF. The SPL values of the first six tonal harmonics of the full-scale outdoor measurement are given in Table 6.5. These SPL values will be compared to the SPL values obtained by the HeliX-tool which will be given in Chapter 7.

Table 6.5: The SPL levels in dB of the six harmonics of the four measurements and BPF

Measurement	SPL of 1st harmonic	SPL of 2nd harmonic	SPL of 3rd harmonic	SPL of 4th harmonic	SPL of 5th harmonic	SPL of 6th harmonic	BPF [Hz]
Take-off 1	73.7929	68.0703	59.8114	50.4765	44.3097	35.0460	122.07
Take-off 2	81.3463	76.1651	65.5668	57.3430	53.8462	45.2822	122.07
Take-off 3	78.0717	73.5250	62.4890	59.7931	52.6208	42.4150	122.07
Fly-over	88.2779	85.9300	77.1177	68.0413	71.6999	64.6207	128.17

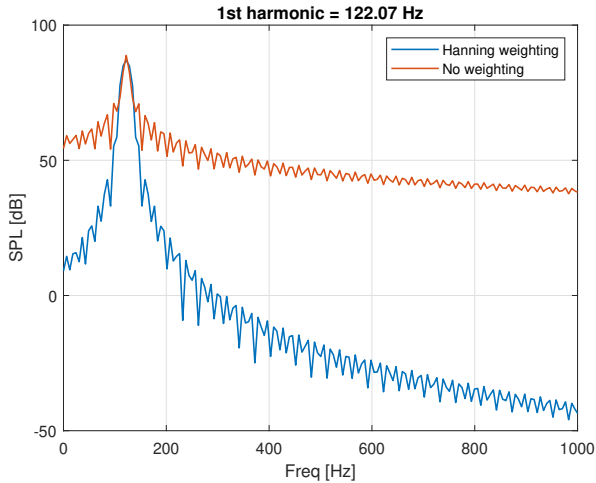
6.3. Main lobe width

When applying the Hanning weighting function, the main lobe width increases. To check whether the increase in the main lobe width of the full-scale outdoor noise data and model output is plausible, a simulation is created for a simple sine function where the same signal processing is applied.

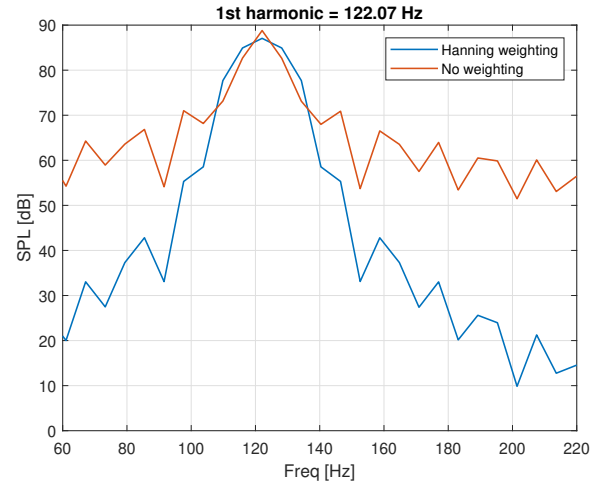
The main lobe represents the magnitude of the sound source. The main lobe width is approximately determined by the df and provides information about the spatial resolution in the frequency domain. The main lobe width is determined at -3 dB from the main lobe's peak [40].

The value of the peak is 85.7844 dB and 84.0529 dB for the not weighted and Hanning weighted signal respectively. The width of the main lobe is thus determined at 82.7844 dB for the not weighted signal and 81.0529 dB for the Hanning weighted signal.

In figure Figure 6.7 the main lobe width is plotted of this simple sine function for the first harmonic with and without Hanning weighting. For the not weighted signal, the main lobe width is approximately 8 Hz. For the Hanning weighted signal, the main lobe width is 14 Hz.



(a) Main lobe width simulation for $X = \sin(2\pi BPft)$



(b) Zoomed in plot

Figure 6.7: Simulation of the main lobe width

7

Validation of the HeliX-tool

After all the input variables are found and the full-scale outdoor data has been processed and analyzed, the HeliX-tool can be validated. This chapter contains information about the validation process of the HeliX-tool. It starts with the explanation of the validation methods from which one can choose in [Section 7.1](#). After the validation method is chosen, the chapter gives the results of the validation in [Section 7.2](#).

7.1. Validation method

The validation method chosen for this research thesis is comparison. The output of the HeliX-tool is compared to data from the full-scale outdoor noise measurements. For the purpose of this project, the quality will be solely determined by the accuracy of the HeliX-tool, as other characteristics of the model such as user-friendliness and efficiency can only be assessed when comparing this model to other models. This is out of the scope of this thesis.

7.2. Result

The results of the validation is given in this section. The metrics that will be compared to each other are the SPL and OSPL values at microphone level. These are shown in the frequency spectra in [Subsection 7.2.1](#) and the OSPL versus θ plot in [Subsection 7.2.3](#).

7.2.1. Frequency spectra

The HeliX-tool is run for six harmonics. The frequency spectra given by the model are shown in [Figure 7.1](#). The six harmonics are clearly visible and they decrease in value with increasing harmonic. The same data processing has been performed over the model output, thus zero-padding and Hanning weighting. The outdoor data and model output for the four measurements are given in one plot for a clear comparison. These graphs are given in [Figure 7.2](#).

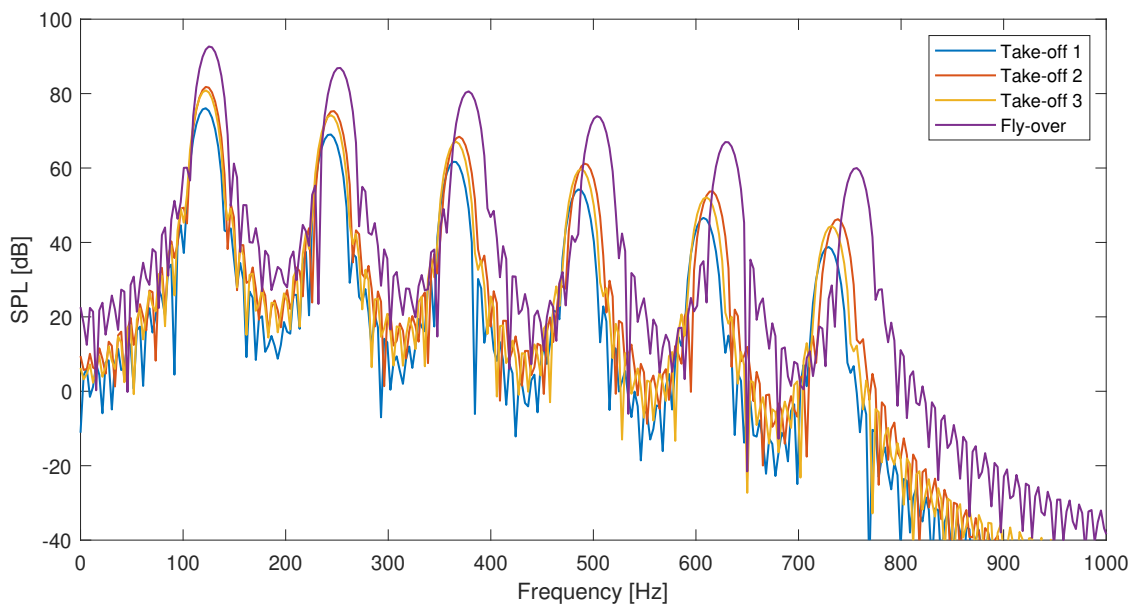


Figure 7.1: Frequency spectra of the modelled operations from the HeliX-tool

From these graphs it can be seen that the frequency location of the peaks are matching and the SPL values are

within 4 dB off. Only for the fly-over, the 5th and 6th harmonics do not match with each other in frequency and SPL value. The model follows the trend of lower SPL values with higher harmonics while the processed full-scale outdoor data gives higher SPL values for the 5th and 6th with respect to the 4th tonal harmonic. This increase in SPL value can be caused by another noise source. This is later discussed in [Subsection 7.2.2](#).

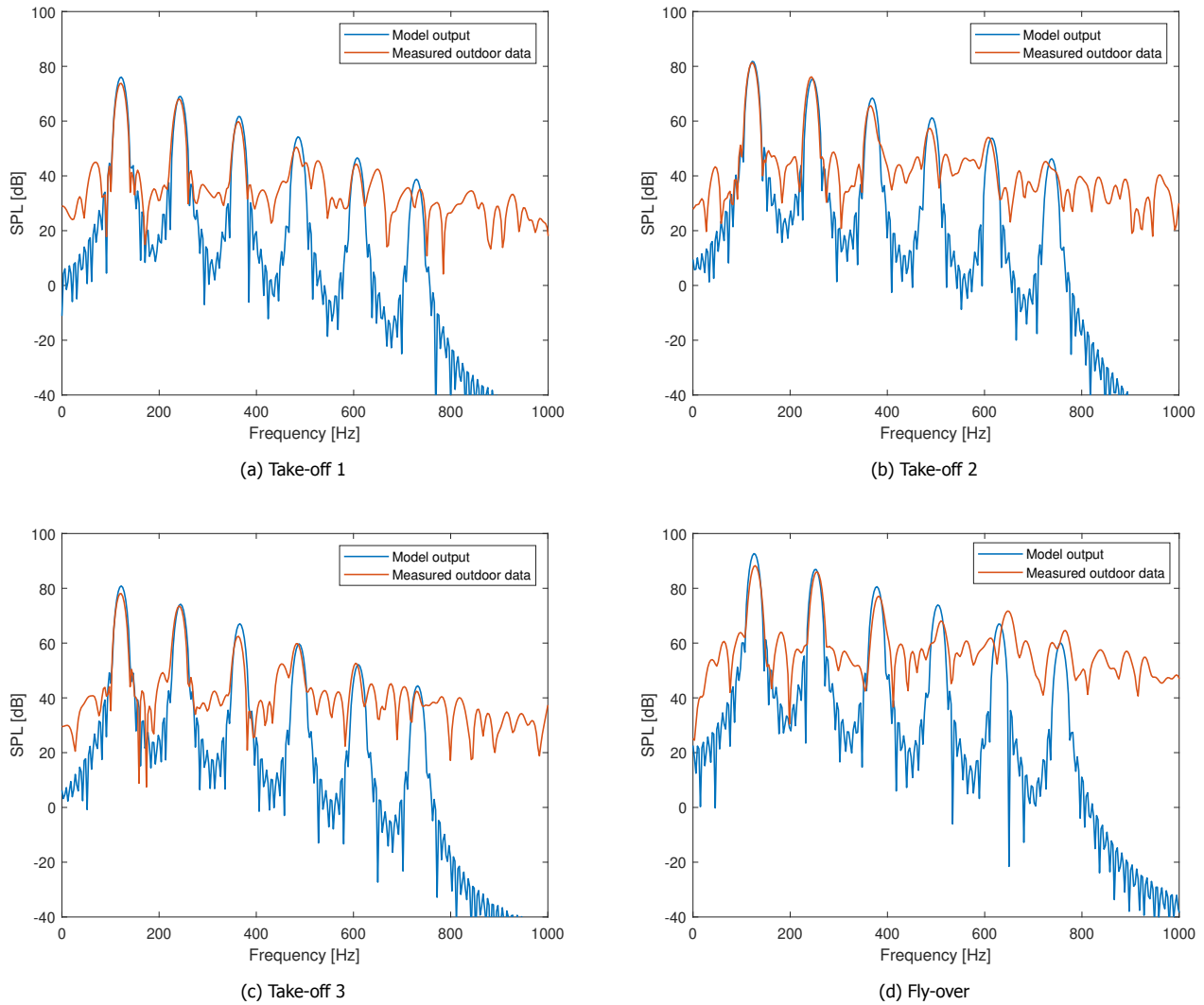


Figure 7.2: Frequency spectra of the Helix-tool and outdoor data

The absolute SPL values of the peaks of the four modelled operations are summarized in [Table 7.1](#) and the BPF obtained from the model is given as well.

Table 7.1: The SPL levels in dB of the six harmonics of the four modelled operations and BPF from the Helix-tool

Measurement	SPL of 1st harmonic	SPL of 2nd harmonic	SPL of 3rd harmonic	SPL of 4th harmonic	SPL of 5th harmonic	SPL of 6th harmonic	BPF [Hz]
Take-off 1	76.0740	69.0128	61.6145	53.9862	46.1486	38.1237	122.07
Take-off 2	81.7977	75.1807	67.9817	61.1938	53.6831	45.9158	122.07
Take-off 3	80.8656	74.2009	67.0691	59.6942	52.1291	44.4063	122.07
Fly-over	92.6618	86.8158	80.6058	73.9388	66.9757	59.9957	125.122

To clearly see how much the absolute SPL values of the outdoor data and model deviate from each other, a scatter plot is created and shown in [Figure 7.3](#). Every harmonic of every measurement is plotted, and the outdoor data SPL values are plotted against the SPL values of the model. If the markers are on the grey diagonal line, the SPL

values match perfectly. In general, the HeliX-tool SPL values are higher than the outdoor data SPL values. This means that the HeliX-tool models the noise levels higher than they are in reality and thus overestimates the noise levels. This is not expected as the model is simplified and has assumptions.

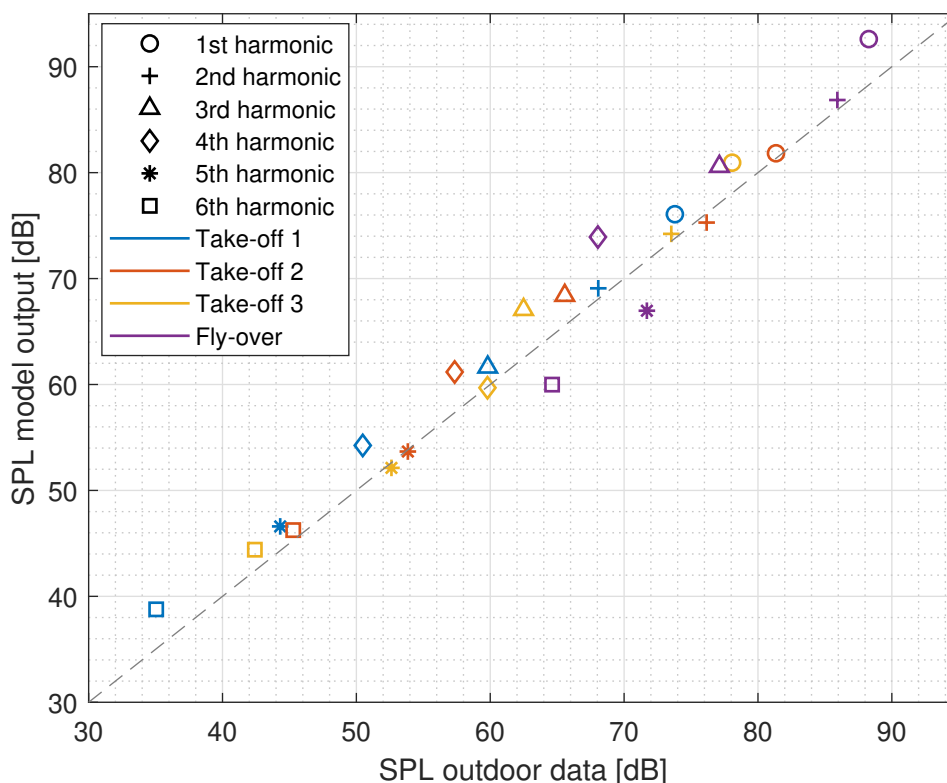


Figure 7.3: Outdoor SPL data and model output SPL values in a scatter plot

7.2.2. Beamforming

Beamforming is a signal processing technique that performs a spatial filtering operation that enables the mapping of the distribution of the noise sources at a definite distance from the microphone array and is, therefore, able to localize the strongest source [41]. For this full-scale outdoor noise measurement it is expected that the propeller is the dominant noise source. Over the years, various beamforming approaches and algorithms have been developed. The increased computation performance of computers and the improvement of data acquisition resulted in well-established beamforming algorithms.

From the take-off 1 measurement in Figure 7.4a it can be seen that behind the 4th and 5th tonal harmonic, a high side lobe is present. This is also the case for the 4th tonal harmonic of the take-off 3 measurement where a high side lobe is present in front of the 4th tonal harmonic as can be seen in Figure 7.5c. The fly-over measurement shown in Figure 7.2d, shows that the 5th peak of the does not coincide with 5th tonal harmonic. Also, the SPL value of the 5th peak is higher than the 4th tonal harmonic, which is not as expected as the higher the harmonic the lower the SPL value should be.

Beamforming is performed at the frequencies of these side lobes and the 5th peak of the fly-over. The 4th and 5th side lobe for the take-off 1 measurement are found at 524.90 Hz and 650.02 Hz respectively. The side lobe of take-off 3 is found at 451.66 Hz and the 5th peak of the fly-over at 647 Hz. The 4th tonal harmonic is at 488.28 Hz and is used as check for the take-off 1 and take-off 3 side lobes as the full-scale outdoor data and model output coincide. For the fly-over the 2nd tonal harmonic is used which is at 256.35 Hz. These peaks and frequencies are indicated for clarification in Figure 7.4.

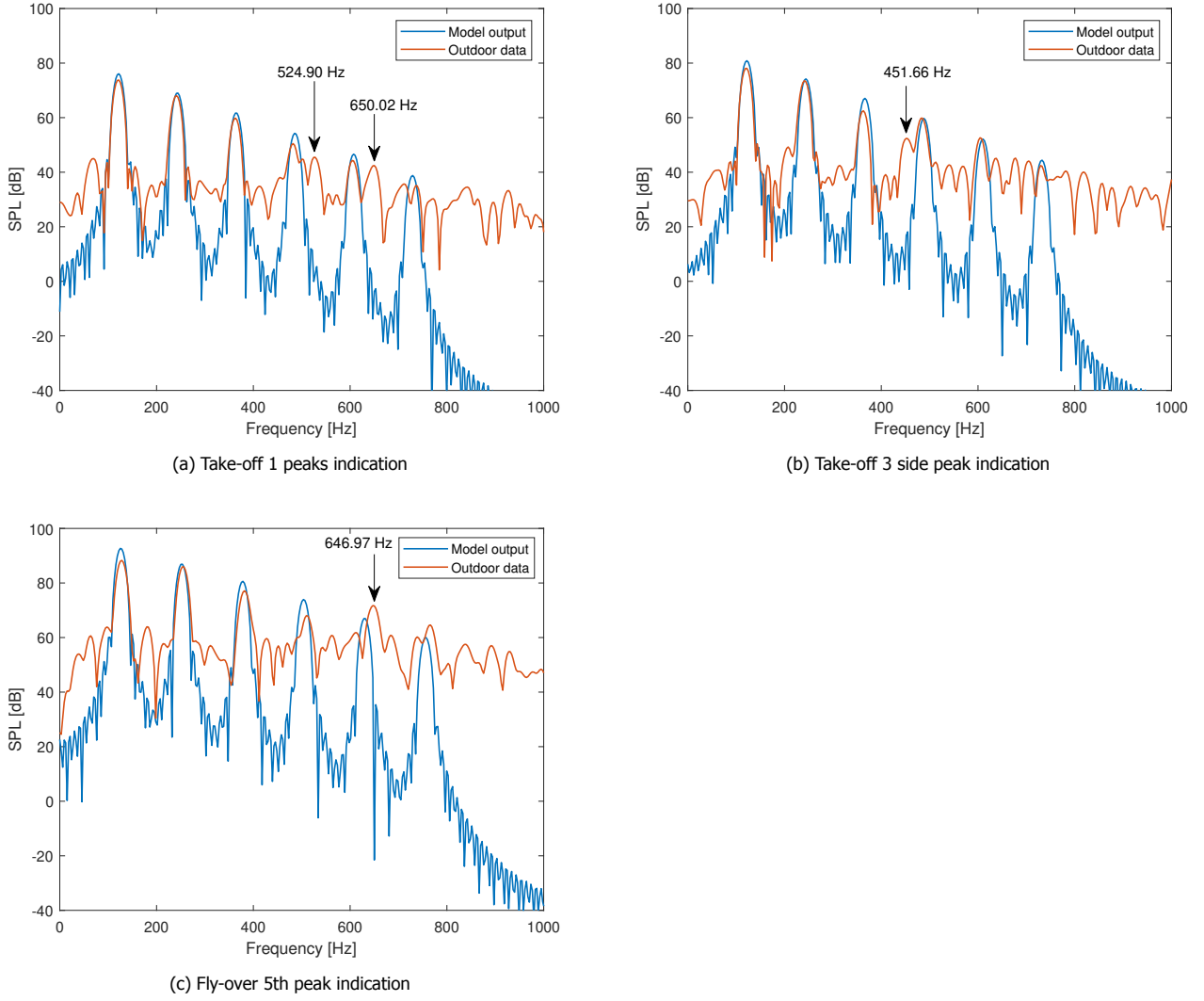


Figure 7.4: Frequency spectra of the HeliX-tool and outdoor data with arrows indicating the side lobes and 5th peak of the fly-over

The 4th and 2nd tonal harmonic will be used as check to see whether the propeller is at the same location in the beamformed plots. If not, another noise source that is more dominant than the propeller could be present.

Two beamforming methods are applied, which are conventional frequency-domain beamforming, CFDBF, and functional beamforming, FB, also in the frequency domain. These are explained below and this section ends with the results of the functional beamforming. The beamforming plots generated with conventional frequency-domain beamforming are found in [Appendix C](#).

Conventional Frequency Domain Beamforming

Conventional frequency domain beamforming is a popular method for aeroacoustic experiments to obtain noise source maps [42]. It is robust, fast, and simple to use. Another advantage is that this method can be used both in the frequency and time domain. However, a disadvantage is the insufficient dynamic range and spatial resolution. Due to the large distance between the aircraft and the observer, the usage of this method is more difficult for aircraft fly-over experiments.

The algorithm regards the Fourier transforms of the measured pressures in the N microphones of the array as an N -dimensional vector $\mathbf{p}(f) \in \mathbb{C}^{N \times 1}$, dependent on frequency (f) given by [Equation 7.1](#):

$$\mathbf{p}(f) = \begin{pmatrix} p_1(f) \\ \vdots \\ p_N(f) \end{pmatrix} \quad (7.1)$$

The measured signal is represented as $s_j \mathbf{g}_j$, where s_j is the strength of the source and $\mathbf{g}_j \in \mathbb{C}^{N \times 1}$ is the so-called

steering vector to a potential source location, ξ_j [42]. The steering vector has N components, $\mathbf{g}_{j,n}, n \in [1...N]$, which are the modeled pressure amplitudes at the microphone locations for a sound source of unit strength. The \mathbf{g}_j used for this research is given by Equation 7.2, where $\tau = r/c$ and r is determined by Equation 7.3.

$$\mathbf{g}_j = \frac{e^{-2i\pi f\tau}}{r} \quad (7.2)$$

$$r = \sqrt{(x_n - x_j)^2 + (y_n - y_j)^2 + h^2} \quad (7.3)$$

Here, x_n and y_n are the x and y-coordinate of the microphones, x_j and y_j are the x and y-coordinate of the scan grid points and h is the altitude.

The autopower of a source, A , given by Equation 7.4, at a certain potential source location at grid point ξ_j , is determined by minimizing the difference between the experimentally obtained pressure vector, \mathbf{p} , and the modeled pressures of a source $s_j \mathbf{g}_j$.

$$A(\xi_j) = \frac{\mathbf{g}_j^* \langle \mathbf{p} \mathbf{p}^* \rangle \mathbf{g}_j}{\|\mathbf{g}_j\|^4} = \frac{\mathbf{g}_j^* \mathbf{C} \mathbf{g}_j}{\|\mathbf{g}_j\|^4} \quad (7.4)$$

In Equation 7.4, an asterisk, (*), represents the complex conjugate transpose and \mathbf{C} is the $N \times N$ cross-spectral matrix, CSM, of the experimentally obtained pressures.

Functional Beamforming

Functional beamforming is an adaptation of the CFDBF algorithm and is developed by Dougherty [43]. The strongest advantage of this method is the improvement in dynamic range [41]. The CSM is Hermitian and positive semidefinite and can be decomposed in its eigenvalues. The CSM is given by Equation 7.5 [42].

$$\mathbf{C} = \mathbf{U} \Sigma \mathbf{U}^* = \sum_{n=1}^N \sigma_n \mathbf{u}_n \mathbf{u}_n^* \quad (7.5)$$

Here, \mathbf{U} , is the unit matrix which has eigenvectors ($\mathbf{u}_1, \dots, \mathbf{u}_N$) of \mathbf{C} as its columns and Σ is the diagonal matrix which has the real-part of the eigenvalues, ($\sigma_1, \dots, \sigma_N$) of \mathbf{C} , on the diagonal entries. The autopower of the source when using functional beamforming is given by Equation 7.6.

$$A_\nu(\xi_j) = \left[\mathbf{g}^* \mathbf{C}^{\frac{1}{\nu}} \mathbf{g} \right]^\nu = \left[\mathbf{g}^* \mathbf{U} \Sigma^{\frac{1}{\nu}} \mathbf{U}^* \mathbf{g} \right]^\nu \quad (7.6)$$

Here, ν is a parameter that needs to be defined by the user and should be higher than 1. If $\nu = 1$, the results equal the CFDBF method. Increasing the parameter ν will result in side lobe attenuation and an improvement in resolution.

The computational time of the functional beamforming method is identical to the CFDBF method, the only difference is the added process of the eigenvalue decomposition of \mathbf{C} [42]. The biggest downside to the use of functional beamforming is the reduction in SPL levels, which is the result of the $\frac{1}{\nu}$ operator.

Beamforming results

At 56.81 s, the aircraft is directly overhead the microphone array during the take-off 1 measurement. A time snap of 0.1 s is chosen for beamforming and starts at 56.76 s. The beamformed plots are given in Figure 7.5. The left column is beamformed at 488.28 Hz and the right column is at the 4th and 5th side lobe at 524.90 Hz and 650.02 Hz. From the plots it can be seen that the aircraft does not fly over the center of the microphone array.

When applying FB, the SPL values decrease which is corrected by simply adding the difference of the SPL values when CFDBF and FB are performed to the functional beamformed SPL values. The white striped lines in the beamformed plots indicate the location of the highest SPL value and thus the center of the noise source which is the propeller in this experiment. The x- and y-coordinate are given in the captions below the figures as well as the value of ν and the maximum SPL levels.

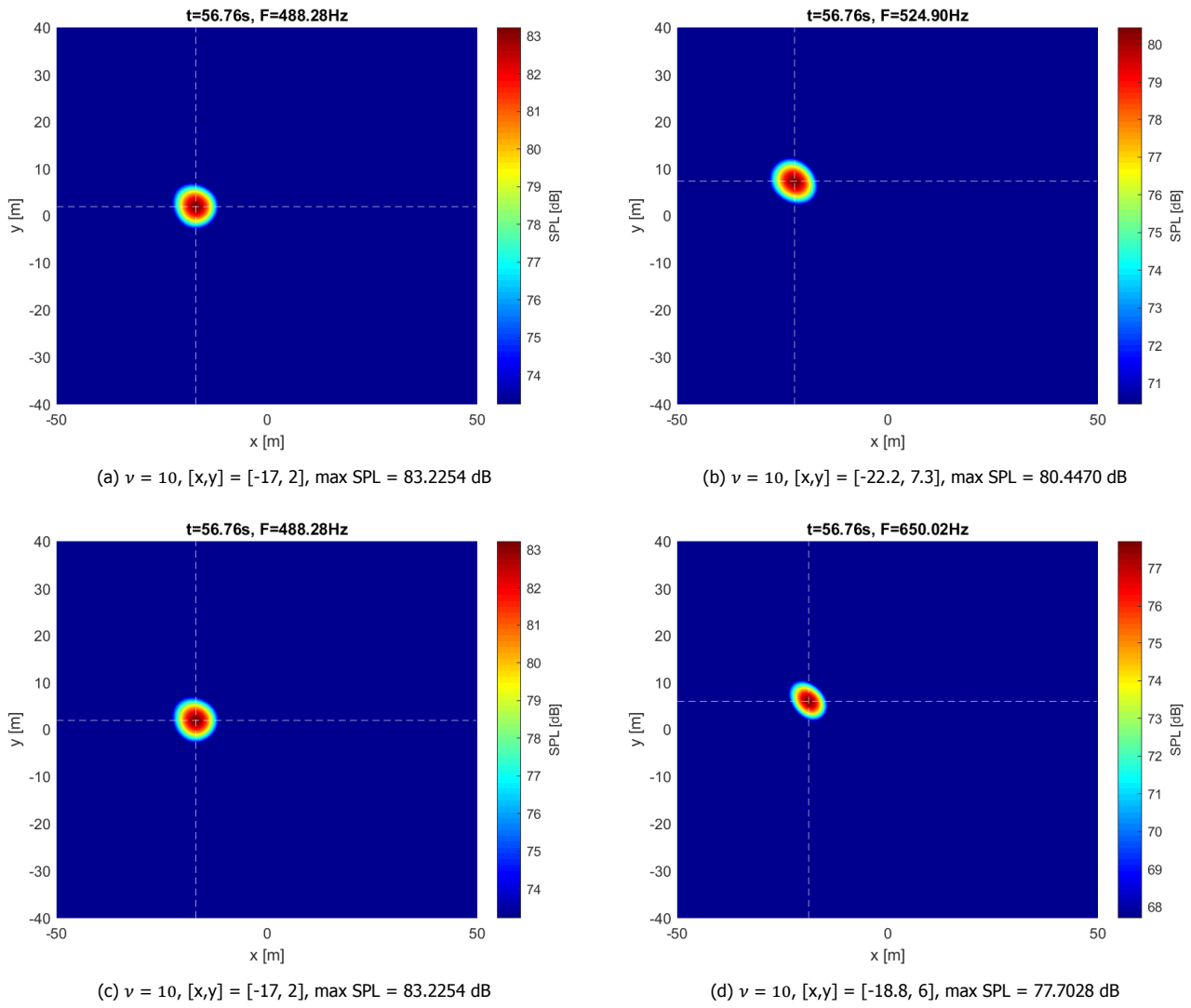


Figure 7.5: Beamformed plots of take-off 1

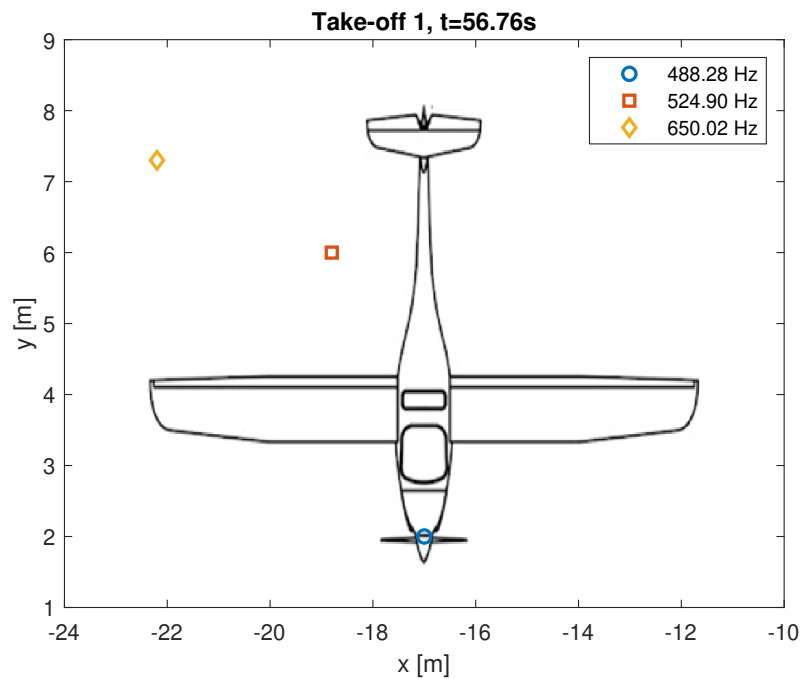


Figure 7.6: Location of dominant noise source for the 4th tonal harmonic, 4th and 5th side lobe

The position of the noise sources at the different frequencies on the Pipistrel are shown in Figure 7.6. The dominant noise course at the different frequencies are not at the same location. For the 4th and 5th side lobe, the location of the noise source is not even on the aircraft.

At 30.25 s, the aircraft is directly overhead the microphone array during the take-off 3 measurement. A time snap of again 0.1 s is chosen for beamforming and starts at 30.2 s. The beamformed plots of the take-off 3 is given in Figure 7.7. The location of the dominant noise source is changing with 0.8 m in x-direction and 0.7 m in y-direction. The position on the aircraft is shown in Figure 7.8.

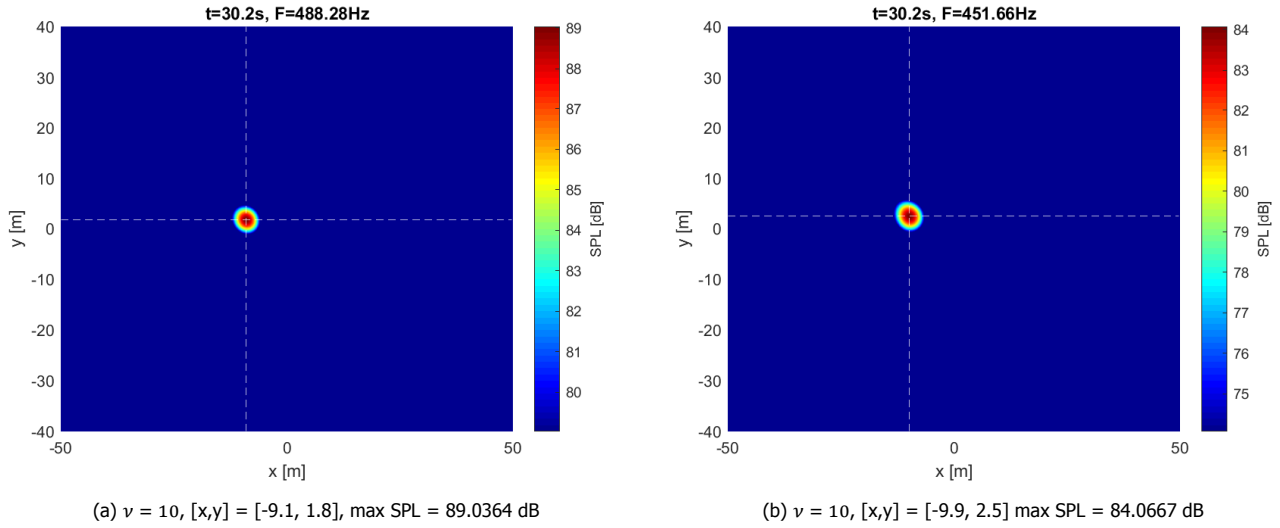


Figure 7.7: Beamformed plots of take-off 3

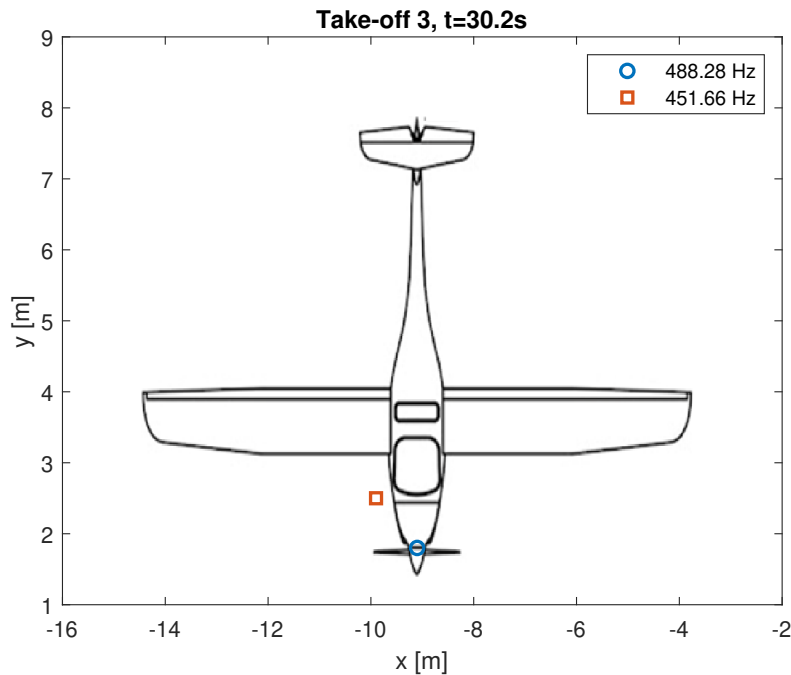


Figure 7.8: Location of dominant noise source for the 4th tonal harmonic and 4th side lobe

At 22.34 s, the aircraft is directly overhead the microphone array during the fly-over measurement. A time snap of again 0.1 s is chosen for beamforming and starts at 22.29 s. The data is also beamformed at 22.39 s and 22.19 s to see the movement of the dominant noise source in the beamformed figures.

The results are shown in Figure 7.9. The left column is the 2nd tonal harmonic and the right column is the 5th peak. The aircraft did not fly over the center of the microphone array and no noise sources other than the aircraft propeller are presented in the beamformed plot. Though, due to the Rayleigh limit which is calculated by Equation 4.1, sources located within 2.93m and 2.32m are not distinguished for the 2nd tonal harmonic and

5th peak respectively and could be present. The x and y-position for the different time stamps are plotted in [Figure 7.10](#).

The location of the center at the 5th peak does not coincide with the center of the 4th tonal harmonic. This can be an indication that there is another noise source present during the measurement located within the Rayleigh limit.

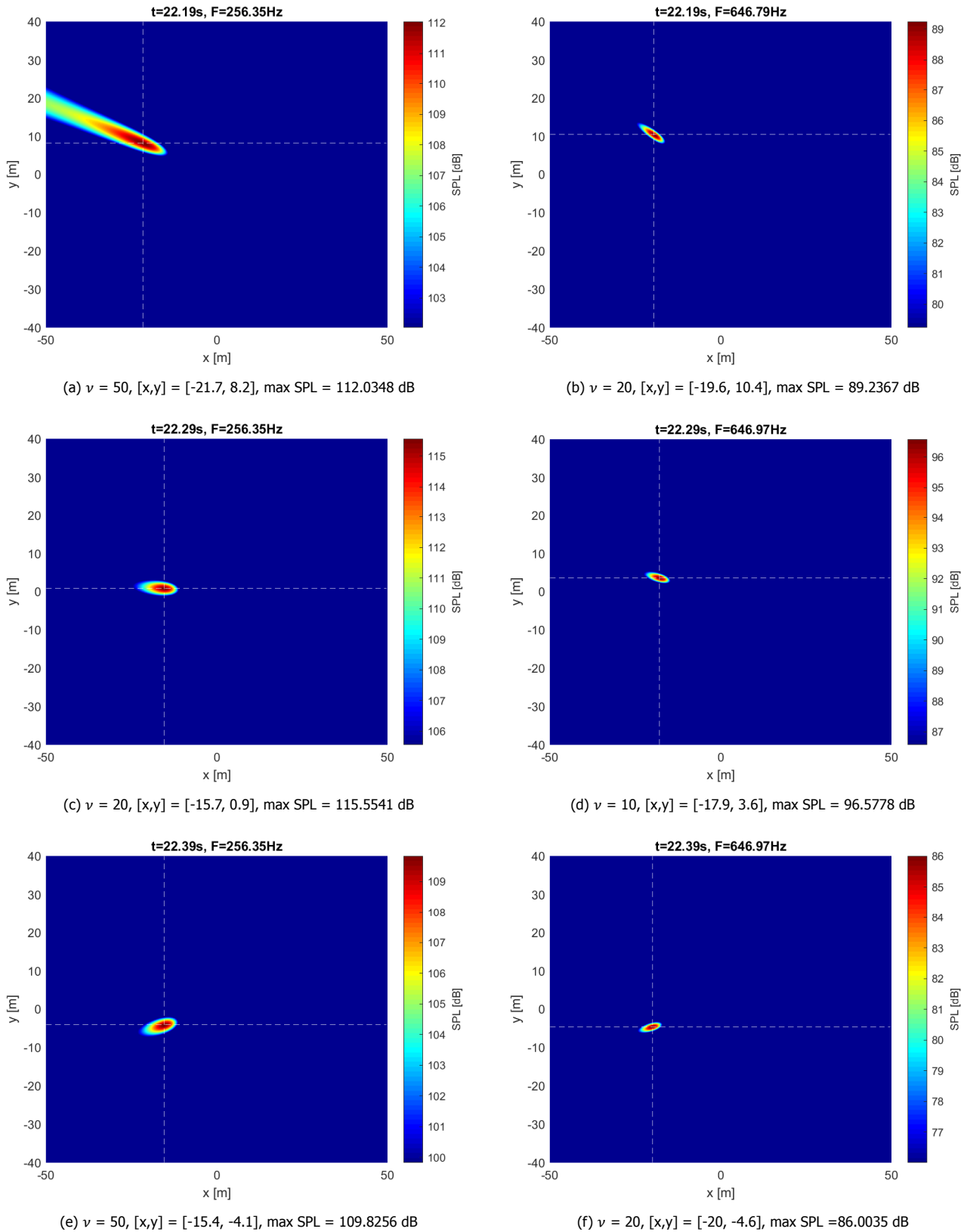


Figure 7.9: FB plots of the 4th tonal harmonic (left) and 5th peak (right) of the fly-over measurement at different timestamps

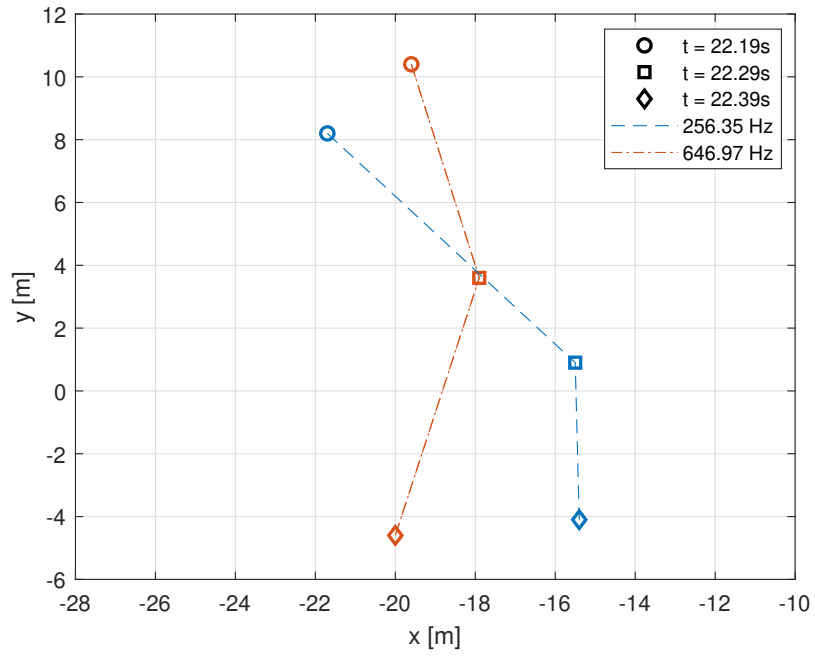


Figure 7.10: Location of dominant noise source for the 2nd BPF and 5th peak for different time stamps

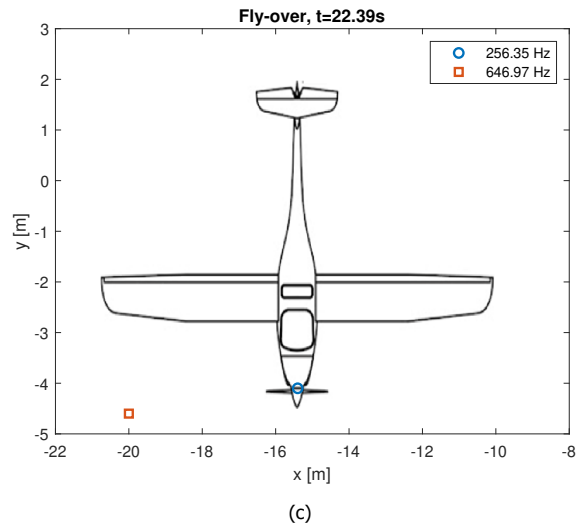
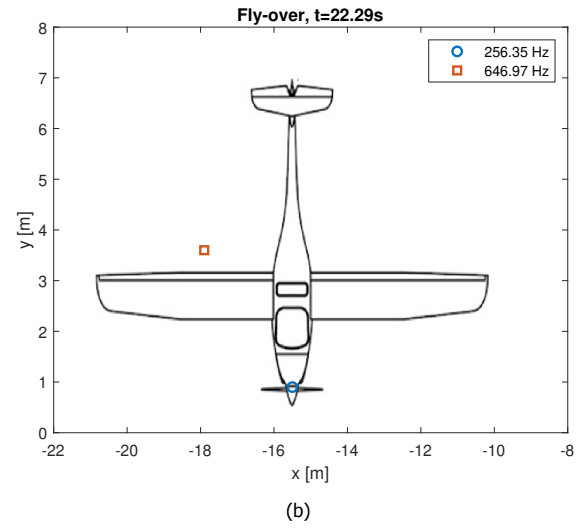
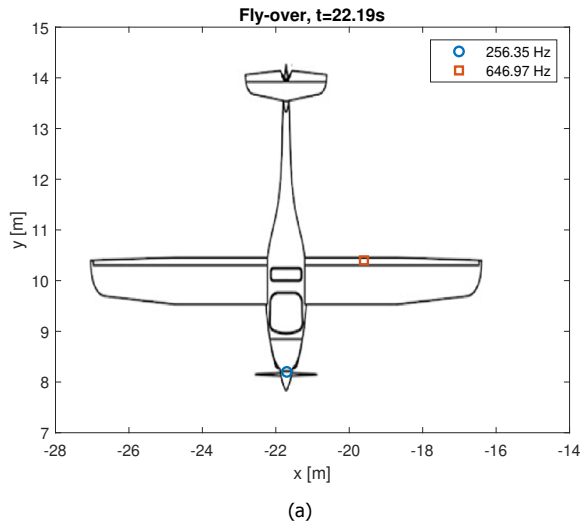


Figure 7.11: Indication of the location of dominant noise source on the Pipistrel

The location of the dominant noise source of the fly-over measurement is plotted on the Pipistrel and shown in [Figure 7.11](#). For the 5th peak, the location changes in all directions with respect to the 4th tonal harmonic. The location of the dominant noise source for the 4th tonal harmonic changes as well. If the aircraft would fly overhead and straight over the microphone array, the trend of the x and y-position would be a vertical line, this is not the case for this experiment as can be seen from [Figure 7.10](#).

It can be concluded that the dominant noise source seen in the beamformed plots at the 2nd and 4th tonal harmonic, 256.35 Hz and 488.28 Hz, is the propeller of the Pipistrel because the peaks of the output of the model and full-scale outdoor data coincide with each other. For the side lobes and 5th peak of the fly-over, no decisive conclusion can be drawn because the location of the dominant noise source shifts.

7.2.3. Directionality plot

As noise sources have directionality, the OSPL levels for both the full-scale outdoor data and HeliX-tool output are plotted against θ and are shown in [Figure 7.12](#). The total OSPL levels, as well as the independent noise source OSPL levels of the HeliX-tool are separately shown, while for the outdoor data, only the total OSPL levels are shown. The OSPL levels of the full-scale outdoor data are lower than the OSPL levels of the HeliX-tool, which matches the findings of [Figure 7.3](#).

The drag noise component has the lowest contribution to the total noise level, while the thickness noise component has the highest contribution. This is interesting as the thickness noise does not have a high contribution below $M=0.7$ according to Made and Kurtz in [9]. But in Akkermans et. al [44], it is found that thickness noise has a low contribution to the total noise up to M_h numbers of 0.6. The M_h for the fly-over experiment is 0.64, thus higher than 0.6, so based on Akkermans et. al [44], it is logical that the thickness noise has the highest contribution.

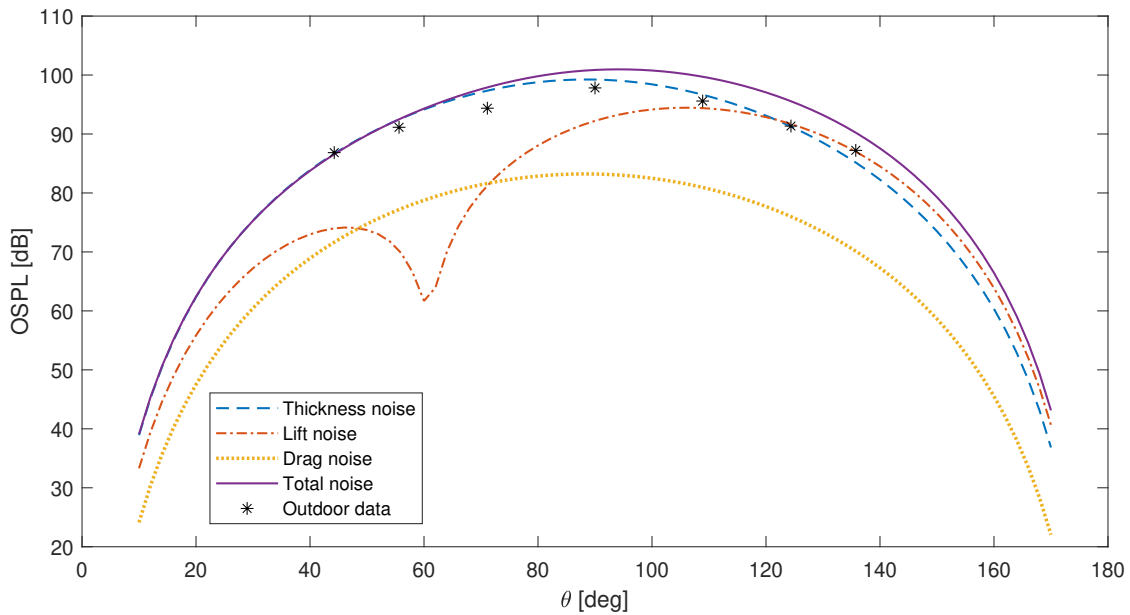


Figure 7.12: Directionality plot

The θ for the outdoor data OSPL levels are found by taking the OSPL levels at 0.1 s time interval from 22.29 s. θ is defined as the radiation angle between from propeller axis to observer point in degrees as was shown in [Figure 2.5](#) in [Section 2.7](#). It is assumed that the aircraft is overhead the microphone array at 22.34 s and thus at $\theta = 90^\circ$. The aircraft flies 4.17091 m in 0.1 s and with the altitude known, the θ can be calculated with simple trigonometry rules. The timestamps with corresponding θ 's, OSPL values and r are found in [Table 7.2](#).

Table 7.2: Outdoor data OSPL parameters

Time stamp [s]	θ [°]	OSPL [dB]	r [m]
21.99	44.25°	86.8398	17.46
22.09	55.62°	91.1393	14.77
22.19	71.11°	94.3733	12.88
22.29	90°	97.8133	12.19
22.39	108.89°	95.5878	12.88
22.49	124.38°	91.3502	14.77
22.59	135.75°	87.2260	17.46

The OSPL values from the HeliX-tool are also presented in a polar plot which is shown in Figure 7.13. The propeller is shown in the center of the plot and the flight direction of the aircraft is from 180° to 0°.

The OSPL level is highest at 90° and 270°. At 90°, the aircraft is overhead the microphone array which results in the highest sound level. At the back of the propeller, the lift OSPL values are higher than in front of the propeller. This is due to the slipstream at the back of the propeller. The airflow flows through the propeller and becomes distorted.

From Figure 7.13 it can be seen that the loading noise, which is the drag and lift noise combined, is shown as a quadrupole source while in Section 2.1, the loading noise could be represented as an array of dipoles. The thickness noise is shown in the polar plot as a dipole, while this could be represented as an array of monopoles. However, the polar plot is in agreement with literature found in Marte and Kurtz [6] and Mao et. al [45]. The change in behavior is probably due to the forward velocity of the propeller.

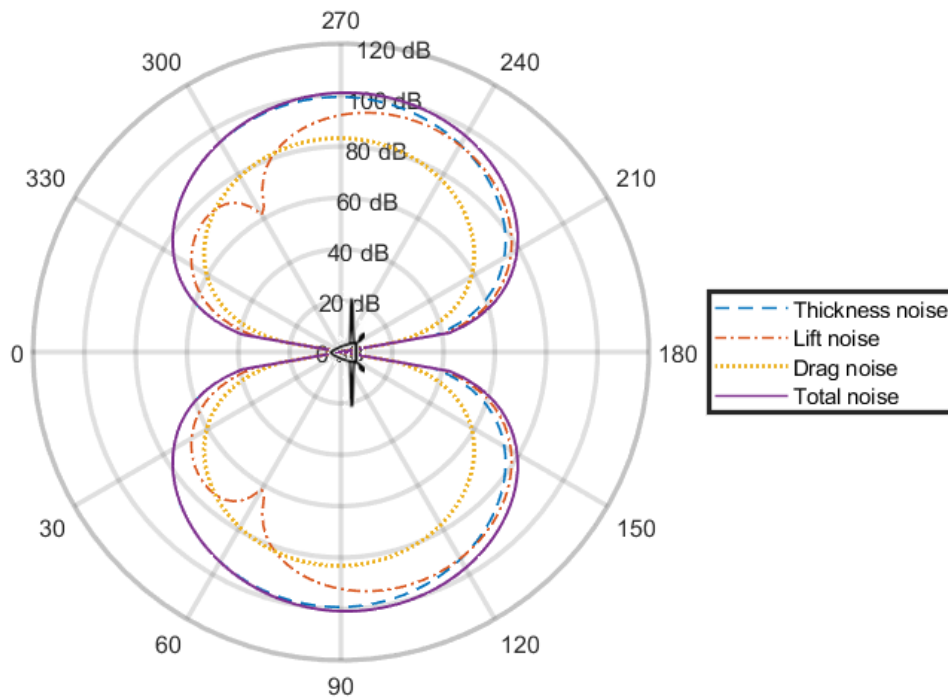


Figure 7.13: Polar plot of OSPL levels when aircraft is overhead the microphone array

8

Conclusion & recommendations

This chapter outlines the conclusion of this research in [Section 8.1](#) and with the recommendations based on the conclusion in [Section 8.2](#).

8.1. Conclusion

The objective of this master thesis was to assess the quality of the propeller noise model called HeliX-tool created by M. Haddaoui by verification and experimental validation. For the purpose of this project, that quality is defined as the accuracy of the model. The HeliX-tool is analyzed and a sensitivity analysis is performed. This sensitivity analysis helps in understanding which parameters should be determined with high accuracy to obtain confidence in the model output. The model was most sensitive to a change in V_x and thus this parameter needs to be determined with a high accuracy. To obtain the data for the experimental validation, four outdoor noise measurements were performed at airport Teuge. The measurements consisted of three take-offs and one fly-over and were performed with the Pipistrel Velix Electro. This is the first certified electric two-seat light-weight propeller aircraft in the Netherlands. With the electric engine, it was expected to have no other noise sources present than the propeller and is, therefore, a suitable choice for comparing the outdoor noise data with the HeliX-tool output.

Two validation metrics are assessed for the quality assessment, these are the SPL and OSPL values. The SPL values are plotted against the frequency and compared for all four measurements, while the OSPL is only compared for the fly-over measurement. The reason being, that for the fly-over the change in altitude is minimal during the measurement while this is not the case for the take-offs which makes it difficult to model for θ and the distance between observer and source is the smallest. The constant altitude enables the generation of the directionality plot where the OSPL values are plotted against the radiation angle, θ .

Looking at the frequency spectra, the SPL values of the full-scale outdoor data and model are within 4 dB to each other. The match in BPF and higher harmonics is in good agreement with each other up to the 4th harmonic. The 5th and 6th harmonics are deviating with approximately 3 Hz. The SPL values of the six harmonics for the four measurements are presented in a scatter plot to see how much the absolute values deviate from each other. From the scatter plot, one can see that in general the SPL values of the HeliX-tool are higher than the values from the outdoor data measurements. The SPL levels of 5th and 6th harmonic of the fly-over measurement are quite off and the frequency of the 5th peak of the outdoor data does not match the frequency of the 5th tonal harmonic. The 5th peak of the outdoor data is at 647 Hz and is beamformed. The 4th peak of the outdoor measurement of the fly-over, which coincides with the frequency of the 4th tonal harmonic, is also beamformed as check. In both beamformed plots, only one noise source is present. However, the location of the noise source is not the same at the 4th tonal harmonic and 5th peak which can indicate that there is another noise source present than the propeller causing the shifted 5th peak.

The directionality plot shows that the drag noise has the lowest, while the thickness noise has the highest contribution to the total noise. The total OSPL values from the outdoor data are lower than the OSPL values of the HeliX-tool, which matches the SPL values of the full-scale outdoor data which are lower than the SPL values of the HeliX-tool.

In general, based on the two validation metrics, it can be concluded that the HeliX-tool is of good quality. The outdoor noise data is obtained with an electric aircraft, meaning the propeller would be the dominant noise source and this data would be appropriate to validate the HeliX-tool with. Also, the helical tip Mach number for the measurements lie between 0.61 and 0.64, which are lower than 0.7 and thus XRotor with its Prandtl-Glauert compressibility correction can be used. The confidence in the HeliX-tool is increased and can be used as a tool in the design phase of new advanced propellers but is limited to Mach numbers below 0.7.

8.2. Recommendations

There are several recommendations for future research on the HeliX-tool. The first recommendation is to obtain the performance coefficients, C_t and C_p , of the aircraft that is used for the outdoor measurements. To perform a

high confidence validation, all the intermediate results need to be validated as thoroughly as the ultimate output of the model. Knowing these parameters will give an intermediate check and will help in understanding where the potential error occurs. If there is a substantial difference in the value of the performance coefficients, there is likely an error in the first part of the HeliX-tool that includes XFOIL and XRotor.

The second recommendation is to have the manufacturer's information on the propeller geometry and the NACA airfoil coordinates. Now, the geometry has been captured by 3D scanning and manually obtaining the coordinates, which is prone to errors. However, a 3D scanned propeller might give a more realistic geometry than information from a manufacturer as they will likely present the designed geometry and not the geometry after the propeller blade is produced. To know what case results in more accurate noise values, a propeller with known geometry and NACA airfoil coordinates should be 3D scanned and both geometries should be run in the model.

Performing more fly-over measurements is the third recommendation. To create the directionality plot, there is only one fly-over available. It would be desirable if there was at least one more. In general, more measurements result in more data which is always beneficial to assess the quality of the model.

The quality of the beamforming plot would also be increased with the addition of the optical camera. The image generated by the optical camera can be overlaid in the beamforming plot to see whether the noise source that is beamformed is positioned at the noise sources of the aircraft.

The last recommendation is finding another way to obtain the value of the altitude. In this research, the GoPro videos are used to see the flight instruments and read the altitude of the altimeter. This method is prone to errors and does not have high accuracy.

Bibliography

- [1] T. Lang, *Short-haul flights are the worst offenders for CO₂*, <https://www.robeco.com/nl/visie/2020/02/short-haul-flights-are-the-worst-offenders-for-co2.html> (2020).
- [2] P. Alves, M. Silvestre, and P. Gamboa, *Aircraft propellers—is there a future?* *Energies* **13**, 4157 (2020).
- [3] A. Filippone, *Aircraft noise prediction*, *Progress in Aerospace Sciences* **68**, 27 (2014).
- [4] M. Schulz and L. Laube, *Identification of noise sources in a turboprop engine bay*, in *16th AIAA/CEAS Aeroacoustics Conference*, Aeroacoustics Conferences (American Institute of Aeronautics and Astronautics, 2010).
- [5] M. Haddaoui, *Development of a propeller source noise model*, Master's thesis, Delft University of Technology, The Netherlands (2019).
- [6] J. E. Made and D. W. Kurtz, *A review of aerodynamic noise from propellers, rotors, and lift fans*, (1970).
- [7] R. Merino Martinez, M. Snellen, and D. Simons, *Determination of aircraft noise variability using an acoustic camera*. 23rd International Congress of Sound and Vibration: Athens, Greece (2016).
- [8] D. Russell, J. Titlow, and Y.-J. Bemmen, *Acoustic monopoles, dipoles, and quadrupoles: An experiment revisited*, *American Journal of Physics* **67**, 660 (1999).
- [9] D. B. Hanson, *Helicoidal surface theory for harmonic noise of propellers in the far field*, *AIAA Journal* **18**, 1213 (1980).
- [10] E. Envia, *Asymptotic theory of supersonic propeller noise*, *AIAA Journal* **32** (1992), 10.2514/3.11978.
- [11] H. Brouwer, *A lifting line model for propeller noise*, in *12th Aeroacoustic Conference* (1989).
- [12] H. Brouwer, *On the use of the method of matched asymptotic expansions in propeller aerodynamics and acoustics*, *Journal of Fluid Mechanics* **242**, 117 (1992).
- [13] D. B. Hanson, *Compressible lifting surface theory for propeller performance calculation*, *Journal of Aircraft* **22**, 19 (1985).
- [14] J. E. Ffowcs Williams and D. L. Hawkings, *Sound generation by turbulence and surfaces in arbitrary motion*, *Philosophical Transactions of the Royal Society of London. Series A, Mathematical and Physical Sciences* **264**, 321 (1969).
- [15] C. H. Hansen, *Fundamentals of acoustics*, Department of Mechanical Engineering, University of Adelaide (2018).
- [16] B. Magliozzi, D. Hanson, and R. Amiet, *Propeller and propfan noise*, *Aeroacoustics of flight vehicles: theory and practice* **1**, 1 (1991).
- [17] O. Bergmann, F. Möhren, C. Braun, and F. Janser, *AERODYNAMIC ANALYSIS OF SWEPT PROPELLER WITH BET AND RANS* (2021).
- [18] M. Drela, *XFOIL subsonic airfoil development system*, <https://web.mit.edu/drela/Public/web/xfoil/> (2013).
- [19] P. Klein, *Parametric Modeling and Optimization of Advanced Propellers for Next-Generation Aircraft*, Master's thesis, Delft University of Technology, The Netherlands (2017).
- [20] M. Drela and H. Youngren, *XROTOR User Guide*, http://web.mit.edu/drela/Public/web/xrotor/xrotor_doc.txt (2003).
- [21] Akiti, *Aerodynamics Example #1: Finding the Critical Mach Number of an Airfoil*, <http://www.akiti.ca/Mcrit.html> (-).
- [22] P. Aumond, A. Can, V. Mallet, B. Gauvreau, and G. Guillaume, *Global sensitivity analysis for road traffic noise modelling*, *Applied Acoustics* **176**, 107899 (2021).
- [23] B. Iooss and P. Lemaître, *A review on global sensitivity analysis methods*, in *Uncertainty Management in Simulation-Optimization of Complex Systems: Algorithms and Applications*, edited by G. Dellino and C. Meloni (Springer US, Boston, MA, 2015) pp. 101–122.
- [24] A. Saltelli, S. Tarantola, F. Campolongo, and M. Ratto, *Sensitivity analysis in practice: a guide to assessing scientific models*, Vol. 1 (Wiley Online Library, 2004).
- [25] F. Pappenberger, M. Ratto, and V. Vandenberghe, *Review of sensitivity analysis methods*, PA VANROLLEGHEM, éditeur: Modelling aspects of water framework directive implementation , 191 (2010).
- [26] P. M. Sforza, *Chapter 10 - propellers*, in *Theory of Aerospace Propulsion*, edited by P. M. Sforza (Butterworth-Heinemann, Boston, 2012) pp. 409–437.
- [27] J. H. Dittmar, *Cruise noise of the sr-2 model in a wind tunnel*, (1989).
- [28] PIPISTREL, *Velis Electro*, <https://www.pipistrel-aircraft.com/aircraft/electric-flight/velis-electro-easa-tc/> (2021).
- [29] E-Flight Academy B.V., *E-flight*, www.eflight.nl (2021).
- [30] S. Doljé, *Quantifying microphone array directivity*, Master's thesis, Delft University of Technology, The Netherlands (2017).
- [31] F. R. d. Amaral, J. C. Serrano Rico, and M. A. F. d. Medeiros, *Design of microphone phased arrays for acoustic beamforming*, *Journal of the Brazilian Society of Mechanical Sciences and Engineering* **40**, 354 (2018).
- [32] B. Von den Hoff, *Assessment of the use of global optimisation techniques for aircraft noise source identification*, Master's thesis, Delft University of Technology, The Netherlands (2020).
- [33] T. J. Mueller, *Aeroacoustic measurements*, in *Experimental Fluid Mechanics* (Springer-Verlag Berlin Heidelberg,

2002).

- [34] GeoCzech, Inc, *MyGeodata converter*, <https://mygeodata.cloud/converter/kml-to-csv> (2021).
- [35] FARO, *FARO Quantum max arms*, <https://www.faro.com/en/Products/Hardware/ScanArms> (2021).
- [36] Josiah Renfree, *Distance calculation using Haversine formula*, <https://nl.mathworks.com/matlabcentral/fileexchange/27785-distance-calculation-using-haversine-formula> (2014).
- [37] Prof. D.G. Simons and Prof. M. Snellen, *Reader Aircraft Noise and Emissions (part A)*, Faculty of Aerospace Engineering (2020).
- [38] A. Malgouezar, M. Snellen, P. Sijtsma, and D. Simons, *Improving beamforming by optimization of acoustic array microphone positions* (2016).
- [39] J. O. Smith, *Hann or Hanning or Raised Cosine*, https://ccrma.stanford.edu/~jos/sasp/Hann_Hanning_Raised_Cosine.html (2020).
- [40] S. Luesutthiviboon, *Design of an Optimized Acoustic Array for Aero-acoustic Research in an Open-jet Anechoic Wind Tunnel*, Master's thesis, Delft University of Technology, The Netherlands (2017).
- [41] P. Chiariotti, M. Martarelli, and P. Castellini, *Acoustic beamforming for noise source localization – reviews, methodology and applications*, *Mechanical Systems and Signal Processing* **120**, 422 (2019).
- [42] R. Merino-Martínez, P. Sijtsma, M. Snellen, T. Ahlefeldt, J. Antoni, C. J. Bahr, D. Blacodon, D. Ernst, A. Finez, S. Funke, T. F. Geyer, S. Haxter, G. Herold, X. Huang, W. M. Humphreys, Q. Leclère, A. Malgouezar, U. Michel, T. Padois, A. Pereira, C. Picard, E. Sarradj, H. Siller, D. G. Simons, and C. Spehr, *A review of acoustic imaging methods using phased microphone arrays*, *CEAS Aeronautical Journal* **10**, 197 (2019).
- [43] R. P. Dougherty, *Functional beamforming for aeroacoustic source distributions*, in *20th AIAA/CEAS Aeroacoustics Conference*, AIAA AVIATION Forum (American Institute of Aeronautics and Astronautics, 2014).
- [44] R. A. D. Akkermans, M. Pott-Pollenske, H. Buchholz, J. W. Delfs, and D. Almonet, *Installation effects of a propeller mounted on a high-lift wing with a coanda flap. part i: aeroacoustic experiments*, in *20th AIAA/CEAS Aeroacoustics Conference* (2014).
- [45] Y. Mao, C. Xu, and D. Qi, *Frequency-domain model of tonal blade thickness and loading noise*, *The Journal of the Acoustical Society of America* **135**, 93 (2014).
- [46] Agisoft, *Agisoft Metashape*, <https://www.agisoft.com/> (2021).

A

Read me file for HeliX-tool

The HeliX-tool consists of many files in which functions are given. These functions are imported to the "main" file which is where you run the tool. Although the HeliX-tool makes use of two external tools 'XFOIL' and XRotor' you do not need to install these on your computer. The .exe files are in the HeliX-tool folder.

Before you can run the HeliX-tool, you need to give the correct location of the files used in the model on your laptop. The location of these needs to be given in the following Matlab files:

- `read_xrotordata()`, lines 6, 49
- `rightformat()`, lines 5, 24, 43, 62, 81, 100, 119, 138, 157, 176, 195, 214, 233, 252, 271, 290, 309, 328
- `shift_correction()`, lines 17, 60, 103
- `thickness_normalization()`, lines 8, 27, 45, 71
- `xrotor()`, line 7

After the correct locations are given, you need to make sure that your propeller geometry files are in the correct folder and location. Also, prepare the files in the exact same format as given in the SR2-propeller files.

The input files are the following:

- `chord_Sr2` = Radial chord/diameter distribution, Δc
- `betadata_Sr2` = Radial thickness/chord distribution, $\Delta \delta$
- `thicknessdata_Sr2` = Radial difference in β distribution, $\Delta \beta$
- `rR024 ... rR100` = Airfoil coordinates per radial section

These files are imported in the following Matlab files:

- `run_xfoil()` : `betadata_Sr2` & `chord_Sr2`
- `rightformat()` : `rR024 ... rR100`
- `thickness_chord()` : `thicknessdata_Sr2`
- `wavenumber()` : `chord_Sr2`

Also change the n_i , and r_R variables to the correct range of your airfoil coordinates sections. These variables are found in the `main()` and `run_xfoil()` files.

After changing the range of these, also change the variable q in the file `run_xfoil()`. The q selects the corresponding Re and M for the radial location of the 18 radial blade sections.

In [Figure A.1](#), you can see the flow of the model and where all the input files are imported. The yellow blocks are the import files and the grey/purple blocks are the Matlab functions/files.

The other import files are created by the HeliX-tool or do not need to be altered, when using this model for your propeller.

Now you can run the "main" file. XFOIL will give plots of the Cp-coefficient for different angle of attacks. The range of angle of attacks are given in the Matlab file: `run_xfoil()`. These angles can be changed to a smaller range if for example the code is running for a long time to find convergence or not finding convergence after a certain value. Most of the time, you will get an error stating that XFOIL could not find convergence, then you should change the step in angles of attack or the range.

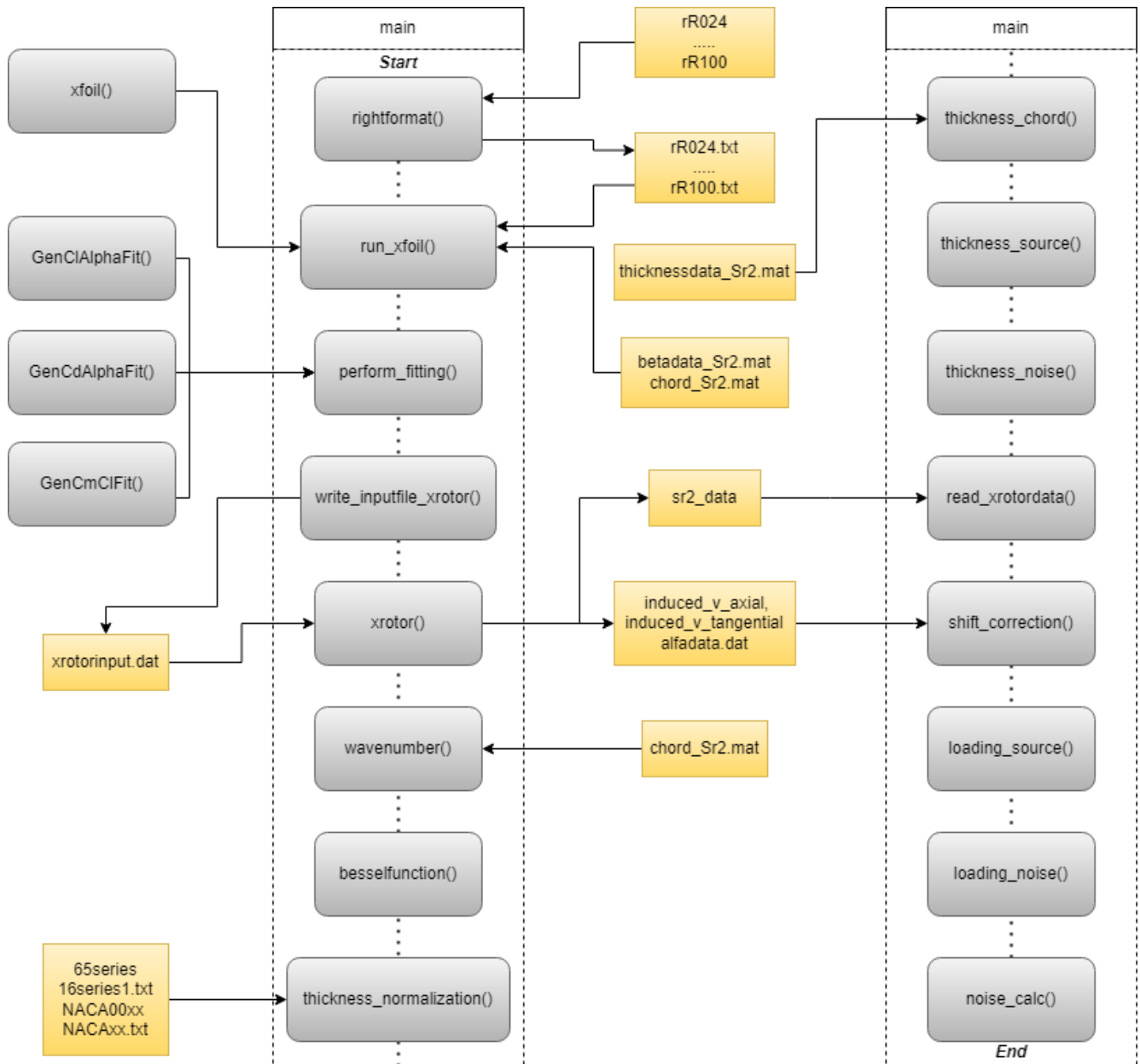


Figure A.1: HeliX-tool flowchart

XFOIL is the most time consuming part of the HeliX-tool.

There could be an error from the `read_xrotordata()` file as it is reading the `SR2_data` and some sections could be stalled. Then there is an "s" located between the Cl and Cd column in the `SR2_data` file, which need to be removed in order to proceed. Remove this "s", save the `SR2_data` file and run the "main" file from line 109 after `xrotor` is run.

Another error could arise reading the `SR2_data` file. Now, the data has moved a row down due to not finding convergence, but still having data. If this is the case, then you should change '16' into '17' on line 7 and '13' into '14' on line 49 & 50 in `read_xrotordata()`.

From line 145 to 157 in the "main" file, the frequency spectra is plotted at a certain radiation angle. This angle can be altered and is defined in line 125.

When the HeliX-tool is finished computing the noise, the code will end with a statement of how long it has run. In the workspace, you can find the outputs such as SPL, OSPL and OASPL.

B

Photogrammetry

Another method can be used to obtain a 3D model of the propeller. This is called photogrammetry. This is an accessible method as it only needs a camera of high resolution, at least 5 Megapixels and photogrammetry software for example Agisoft metashape [46]. There are however some scene or objects requirements:

- Avoid reflecting, shiny or transparent objects. If needed, shoot under a cloudy sky or wrap or cover the object with a non-shiny material.
- Avoid moving objects and unwanted foregrounds.
- Avoid flat objects or scenes.

For scaling, one can make use of the so-called 'markers' which can be generated in the software. These markers are figures that are of a certain size which can be printed and glued to the object. The software will recognize these markers and the correct scaling is found.

The procedure for photogrammetry is capturing the object by making pictures of a piece of the object and continuing until the entire geometry is captured by pictures. The correct way is shown in Figure B.1. After all the photos are taken, the software will combine all the pictures into one 3D geometry.

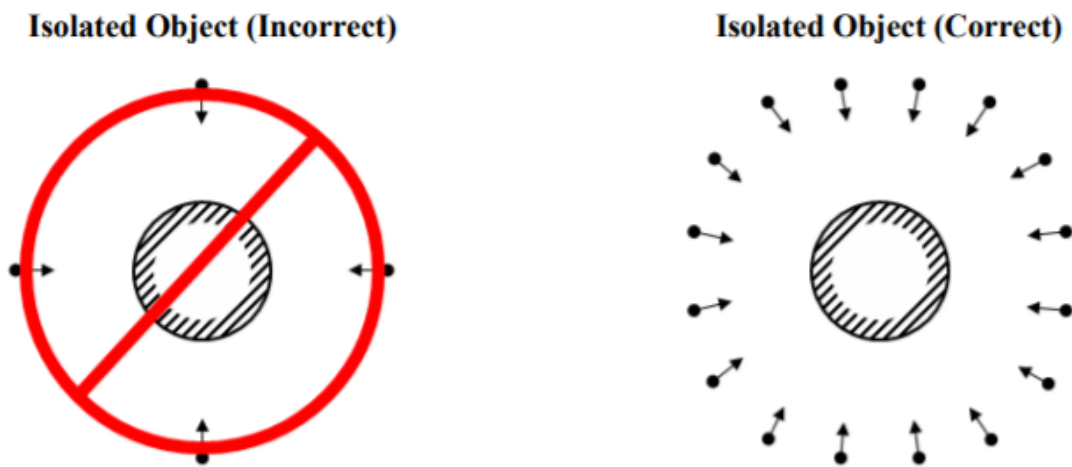


Figure B.1: Capturing the object with photogrammetry

After the geometry is obtained by the photogrammetry software, the model can be exported as .stl file to go into CAD programs for further processing.

C

Conventional beamforming plots

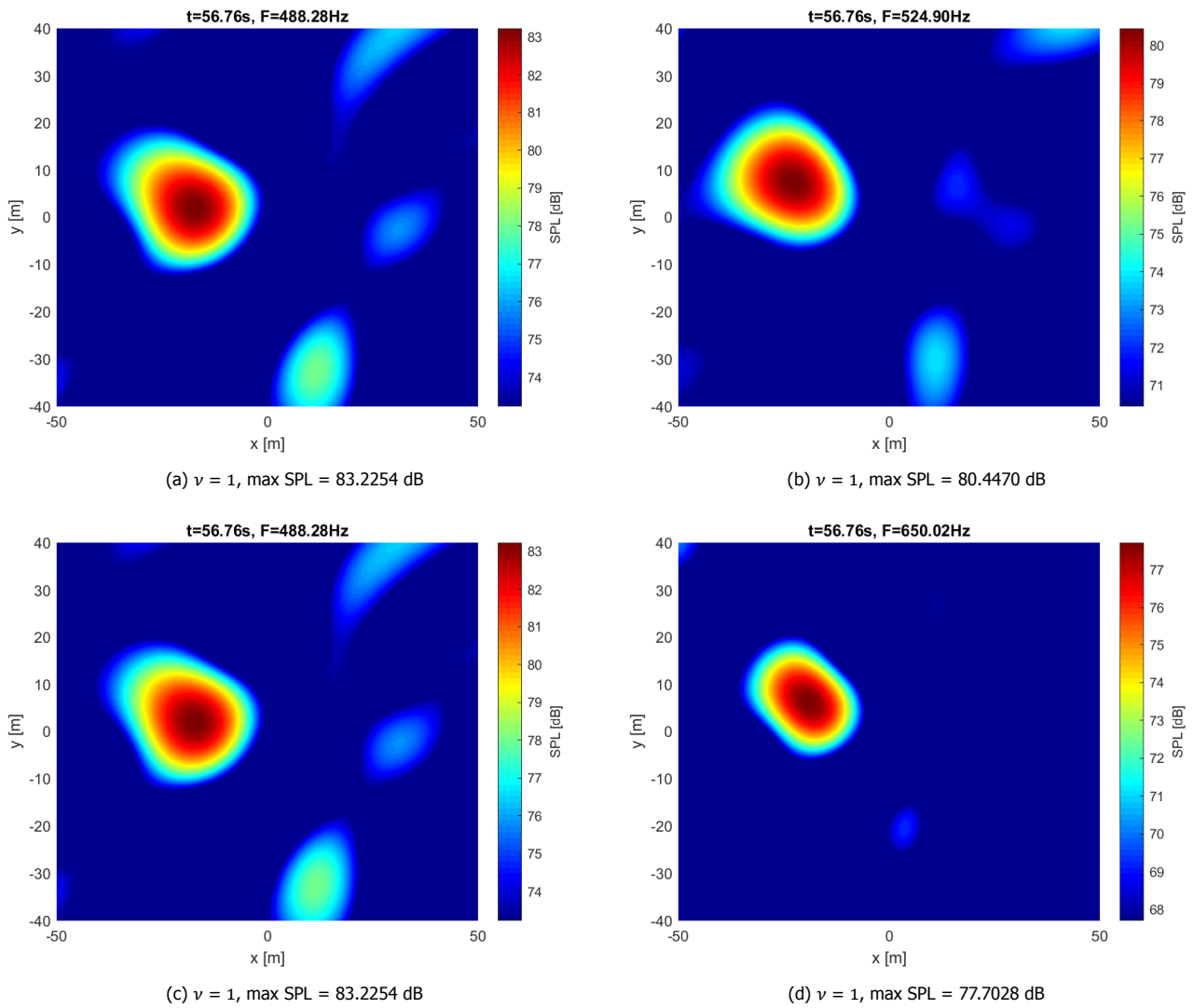
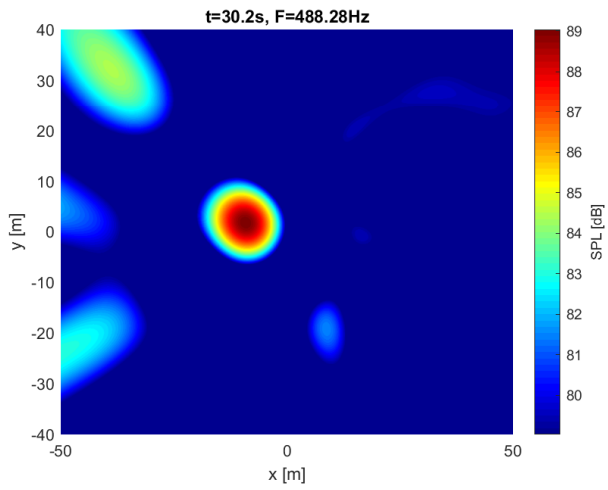
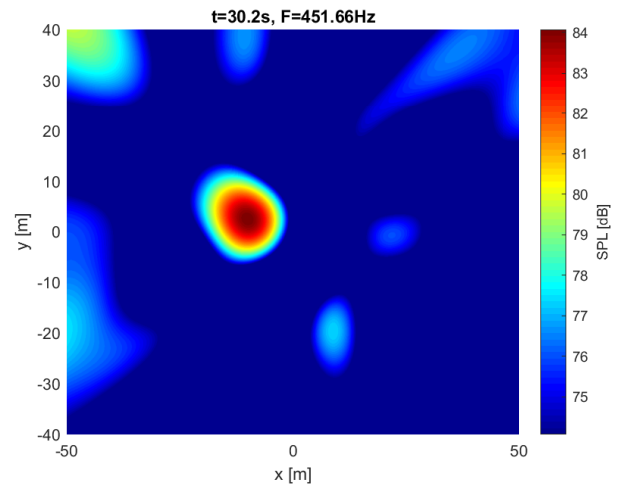


Figure C.1: Conventional beamformed plots of take-off 1

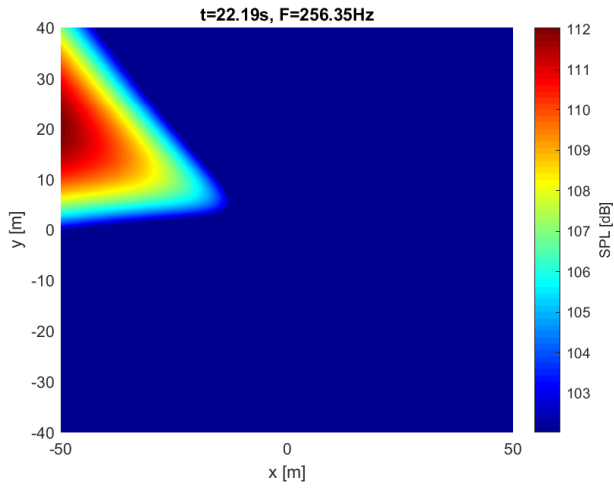


(a) $\nu = 1$, max SPL = 89.0364 dB

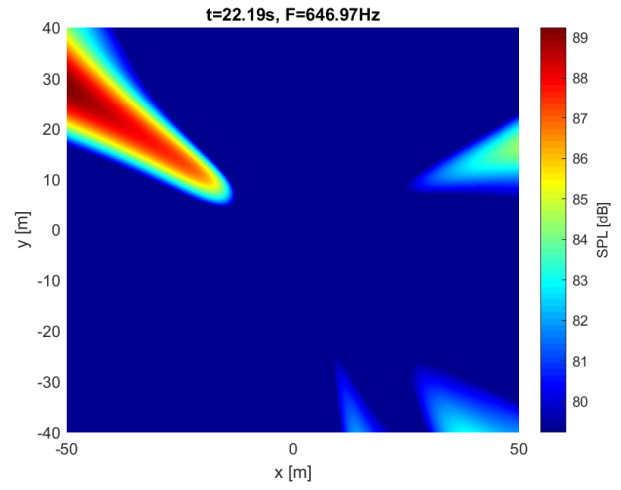


(b) $\nu = 1$, max SPL = 84.0667 dB

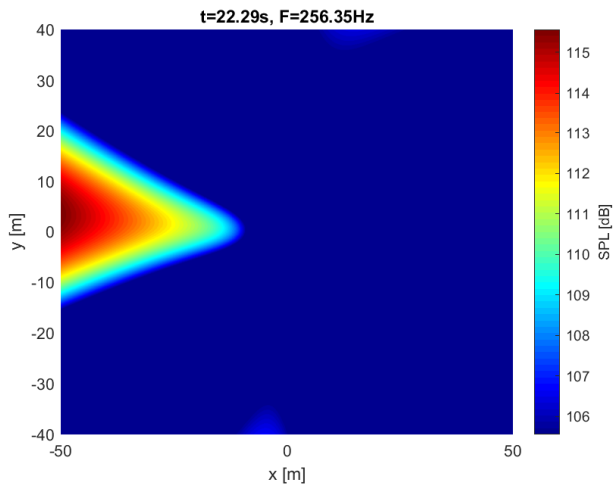
Figure C.2: Conventional beamformed plots of take-off 3



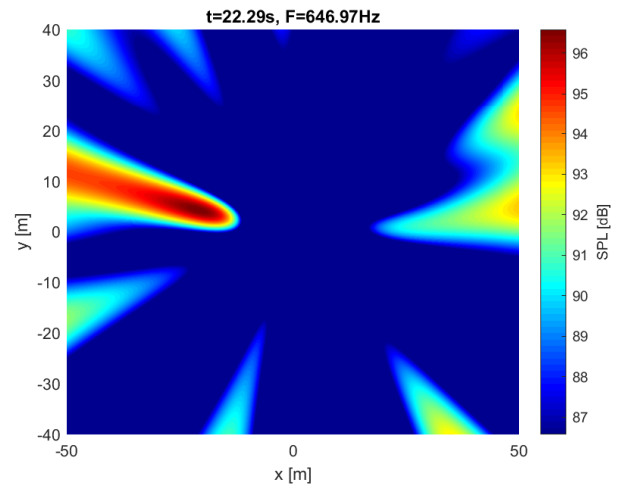
(a) $\nu = 1$



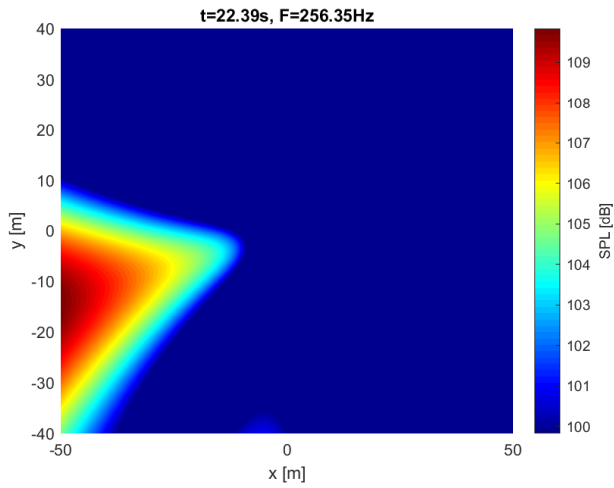
(b) $\nu = 1$



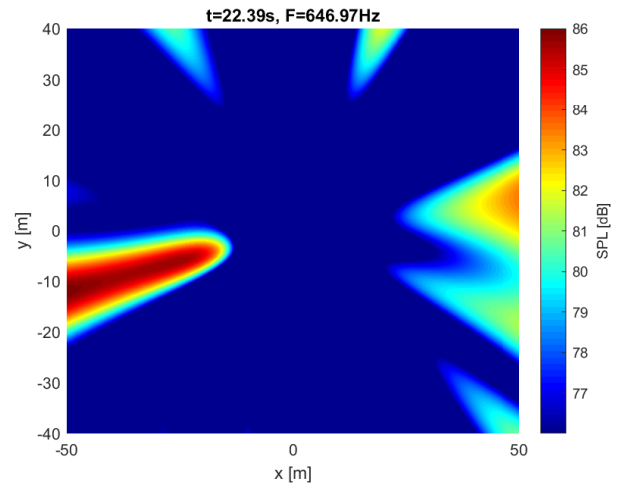
(c) $\nu = 1$



(d) $\nu = 1$



(e) $\nu = 1$



(f) $\nu = 1$

Figure C.3: CFDBF plots of the 2nd BPF (left) and 5th peak (right) of the fly-over measurement at different timestamps